Investigation of MBE-grown InAs/GaAs(001) and InAs/AlAs(001) quantum dot systems using synchrotron X-ray diffraction and complementary techniques

Dissertation
zur Erlangung des Doktorgrades
des Fachbereichs Physik
der Universität Hamburg

vorgelegt von
Andriy Zolotaryov

aus **Kharkov, Ukraine**

Hamburg
2007

Gutachter der Dissertation: Prof. Dr. R. L. Johnson
Prof. Dr. W. Hansen

Gutachter der Disputation: Prof. Dr. R. L. Johnson
Prof. Dr. W. Wurth

Datum der Disputation: 06.06.2007
Vorsitzender des Prüfungsausschusses: Dr. H. D. Rüter

Vorsitzender des Promotionsausschusses: Prof. Dr. G. Huber
Leiter des Departments Physik: Prof. Dr. R. Klanner
Dekan der MIN-Fakultät: Prof. Dr. A. Frühwald

Contents

I Introduction **4**

I.1 Size influenced energy quantization. 4
I.2 Quantum dot based optical devices 6
I.3 Quantum dot fabrication techniques 6
I.4 Regimes of epitaxial growth 8
I.5 Molecular beam epitaxy of quantum dots 10
I.6 Special features of the island growth in InAs/GaAs(001) and InAs/AlAs(001) systems 11
I.7 X-ray diffraction on quantum dots: advantages of synchrotron radiation 12

II Fundamentals of diffraction theory **15**

II.1 Scattering of X-ray photons 15
II.2 Scattering amplitude 16
II.3 Electron density. Fourier Integral. 18
II.4 Atomic amplitude 19
II.5 Diffraction from a periodic lattice 21
II.5.1 Crystal periodicity. Reciprocal lattice 21
II.5.2 Atomic planes. Braggs law. 23
II.5.3 Ewald construction. Reflection sphere. 24
II.6 Shape function 26
II.7 Coherence length. Position correlation between crystals. 27
II.8 Crystal with distortions 28
II.9 Phase problem. 30
II.10 Kinematic approximation 30
II.11 Grazing incidence diffraction. 32
II.11.1 Total reflection effect. Penetration depth. 32
II.11.2 Distorted-wave approximation. 34
II.11.3 Iso-strain approximation. 37
II.12 X-ray reflectivity of thin films 39

III Elastic deformation of SK-islands **40**
III.1 General elasticity theory 40
III.1.1 Mechanical model of pseudomorphic growth 42
III.1.2 Boundary conditions for the reciprocal space search. 43
III.2 Overview of methods for strain field computation in microscopic structures 44
III.3 Finite element analysis 46
III.3.1 Introdunction to FEM method 46
III.3.2 Modeling of elastic strain in SK-island 48
III.3.3 Finite element modeling of SK-island 49
III.3.4 Finite element solution for the SK-islands 50

IV Experimental equipment and techniques **53**
IV.1 Six-circle X-ray diffractometer 53
IV.1.1 Device overview 53
IV.1.2 Diffractometer BW2 54
IV.2 Special equipment 56
IV.2.1 Vacuum chamber for X-ray diffraction experiments 56
IV.2.2 He-chamber for X-ray diffraction experiments 56
IV.3 X-ray diffraction geometries 57
IV.3.1 Terminology 57
IV.3.2 Grazing incidence small angle X-ray scattering (GISAXS) . . . 60
IV.3.3 Grazing incidence diffraction (GID) 61
IV.3.4 Surface-sensitive asymmetrical X-ray diffraction (GI-HRXRD) 62
IV.3.5 X-ray reflectometry (XRR). 62
IV.3.6 Summary 63
IV.4 Surface imaging tools: Atomic force microscopy 63
IV.5 Numerical techniques. 65
IV.5.1 Calculation of intensity patterns 65
IV.5.2 Calculation of GISAXS intensities. 66
IV.5.3 Calculation of XRR intensity profiles. 66

V Theoretical calculations **67**
V.1 Island without displacement field. 67
V.2 Island with displacement field. 70
V.3 Limitations to analytical shape extraction with GID. 73
V.4 Morphology induced changes in island's strain field. 75
V.5 Effects of interdiffusion. 78
V.6 Finite size effects. 80
V.7 Conclusions 84

VI QD samples in synchrotron radiation **86**

VII Homogeneous islands 90
VII.1 InAs/GaAs(001) island systems 90
VII.1.1 AFM 91
VII.1.2 GISAXS 91
VII.1.3 GID 96
VII.1.4 Island composition analysis 100
VII.2 InAs/AlAs(001) island systems 104
VII.3 Conclusions 104

VIII Investigation of island formation 106
VIII.1 Investigation of island growth in InAs/GaAs(001) system 107
VIII.1.1 Structure analysis of islands grown at 530°C 107
VIII.1.2 Structure analysis of islands grown at 500°C 109
VIII.1.3 Structure analysis of islands grown at 480°C 109
VIII.1.4 Discussion 111
VIII.2 Investigation of island growth in InAs/AlAs(001) system 116
VIII.3 Structural investigation of InAs/AlAs(001) system 122
VIII.3.1 Method description 122
VIII.3.2 Experimental implementation 124
VIII.4 Conclusions 127

IX Capped quantum dot systems 129
IX.1 Theoretical calculations 129
IX.2 Experimental investigations 130
IX.3 Conclusions 134

X Summary and outlook 136
X.1 Summary 136
X.2 Outlook 137

Appendix 138

A List of frequently used abbreviations 138

B Linear deformation field algorithm 139

C Investigation of native oxide on InAs(001) 142

Abstract

Within the last decade significant progress in the fabrication of nanoscale island systems using molecular beam epitaxy (MBE) techniques has stimulated the increased industrial interest in these structures as building blocks for modern optical devices exploiting quantum confinement effects.

At the present time the most promising MBE-compatible island systems are based on III-V compound semiconductors. For technological reasons most activities now concentrated on the self-organized formation of InAs based quantum dots on the GaAs(001) and AlAs(001) surfaces exploiting the 3D Stranski-Krastanov (SK) growth. For these systems the produced quantum dot structures exhibit a pronounced size-dependent variations of the electronic properties.

The main obstacle for the bulk production of III-V quantum dot based devices is the unreliable technological yield. The reason for this is the complicated and not well understood self organization process that is used to generate the nanostructures.

In the systems of interest the topographical quality and electronic properties of SK-islands depend strongly on the deposition conditions. Furthermore, InAs/GaAs(001) and InAs/AlAs(001) island systems have quite different characteristics.

In this thesis the InAs/GaAs(001) and InAs/AlAs(001) systems will be analysed by means of synchrotron based X-ray diffraction tools and complementary imaging techniques (atomic force and scanning tunneling microscopy). The central topic of the thesis is the development and testing of X-ray diffraction based techniques for reliably monitoring island topography, and island structure analysis for island systems grown on standard wafers. Finite-element calculations of the strain fields in the island structures have been performed in parallel with the X-ray diffraction studies. The investigation of temperature dependent material supply mechanisms responsible for island formation will be provided for both non-capped island systems. Finally the intermixing in both capped systems will be discussed.

Chapter I

Introduction

I.1 Size influenced energy quantization.

In the atomic model, proposed by Nils Bohr, negatively charged electrons, moving on the defined distances around the positively charged atomic nuclei, possess the discrete sharply resolved energy levels E_n, Fig. 1(d). At temperature, close to "absolute zero" [1], the energy resolution limit for these levels is given by Heisenberg uncertainty principle:

$$\Delta t \cdot \delta E_n = h \tag{I.1}$$

where Δt is the emission decay time for electron on the n-th orbital, and h is a Plank's constant[2]. On the contrary to atoms, in the "infinitely" extended solids the electron positions are delocalised (Fig. 1(a)), leading to the temperature dependent continuous spectrum of energy states and band gaps [1, 2]. The "infinity" of the solid body is characterized by comparison of the electron energy in the solid to the energy of a free electron in vacuum, given by the de Broglie wavelength [3]:

$$\lambda_{deBrogli} \approx h/\sqrt{3m_{eff} \cdot kT} \tag{I.2}$$

where m_{eff} - is an effective electron mass [4], k - Boltzman's constant [5], T - absolute temperature in Kelvin. As a consequence of this definition, the closer the size of solid body lies to the *de Broglie* wavelength, the larger is the influence of quantization effects on its energy spectrum. In crystals with a mosaic structure, the size of each crystallite is much greater than $\lambda_{deBroglie}$ and no energy confinement effects are observed. Only when the size of the crystallite is comparable to interatomic distances,

[1] $T_0 = 0K = -273.15°C$

[2] Plank's constant represents the elementary quantum of energy. $h \approx 6.6261 \cdot 10^{-34}$ [J s]

[3] $E = h \cdot \nu$, $\nu = c/\lambda$, where c- speed of the light in vacuum. $c = 3 \cdot 10^8$ [m/s]

[4] effective mass is a characteristic value of a particle in the media with dispersion coefficient $\delta > 0$

[5] $k \approx 1.380658 \cdot 10^{-23}$ [J/K]

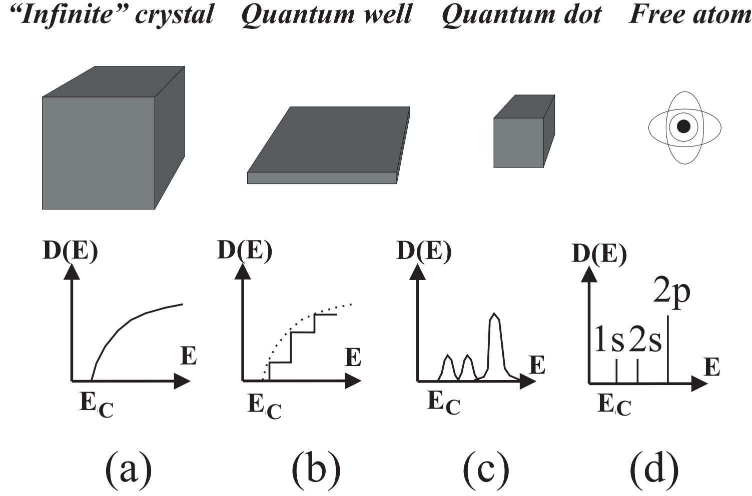

Figure 1: Size dependence of electron energy state density function D(E) representing the quantum confinement effect.

are significant quantum confinement effects observed [3]. Furthermore, since the effective mass of the electron in the crystalline solid can be much smaller than the free electron mass [6] , the quantization effects at low temperatures can be expected even at a sub-micrometer size scale [4].

The direct observation and application of quantization effects was the main motivation for researches within last four decades. At the begin of 1970's the first experimental results have been achieved on a thin layer system, exhibiting 1D thickness dependent energy quantization effect [6, 7, 8].The layered structures where this effect has been observed were called *quantum wells*, Fig. 1(b). At the end of 1980s the progress of nano-technological applications allowed researchers to concentrate their attention on structures where quantization in two (*quantum wires*) and three (*quantum dots*) dimensions can be detected.

In quantum dots, Fig. 1(c), the reduction of all crystal extensions leads to carrier localization in all three dimensions and breakdown of the band structure model with a continuous energy dispersion. Like on atomic scale, the energy spectrum of quantum dot crystal is discrete, and a profound size-dependent change of all macroscopic material properties as compared to the bulk occurs. Typical size of experimentally created quantum dot structures is on the order of 10-100 nm. The research in the field of quantum dots presents a new chapter in modern physics. Moreover, many commercial product related applications of quantum dots have been realized within the last decade, such as single electron transistors and quantum dot lasers.

[6] $m_e = 9.1 \cdot 10^{-31}$[Kg]

I.2 Quantum dot based optical devices

Being quasi-zero dimensional, quantum dots have a sharper density of states than higher-dimensional structures [5]. As a result, they have superior optical properties, and are being researched as a building blocks for diode lasers and quantum dot computers [10].

In quantum-dot based light-emitting diodes the principle of stimulated emission of coherent radiation is used with the radiation energy coupled to the band gap offset of the semiconductor heterostructure. Due to the technological compatibility and band gaps for suitable emission energies [11] the QD-heterostructures based on III-V compounds have found numerous applications. These III-V compounds have emerged themselves as the materials of choice for laser diodes that emit in the 0.7-1.6 μm wavelength range. This range includes the important fibre-optic communication bands at 0.85, 1.31 and 1.55 μm, the pumping bands for fibre amplifiers at 1.48 and 0.98 μm, and the wavelength currently used for optical disk players at 0.78 μm.

The main advantage of quantum dot lasers is the discrete wavelength of the laser response signal [12],[13]. In addition to excellent optical properties quantum dot lasers also offer a lower threshold current density and good temperature stability [14], [15].

Quantum dots are also considered as potential core-elements in devices for solid-state quantum computation. As one of the promising future applications in this field optical addressing (optical charging) concept should be mentioned [16]. This concept can be used as the basis for a very-high-density memory device in which information is written and read by controlling charge storage in quantum dots [17],[18].

I.3 Quantum dot fabrication techniques

In this subsection the main technologies enabling the preparation of quantum dot structures will be briefly described and compared. In the whole variety of QD production methods the two main groups can be distinguished (Fig. 2), namely, *chemical* and *physical* preparation techniques. The chemical methods are based on the *colloidal synthesis* of quantum dots from organic solutions, physical methods can in general be split into *lithography* and *self-organization* techniques [9]. Progress in the technology of colloidal synthesis permits the preparation of monodisperse spherical semiconductor crystals with sizes in the order of 2-4nm. This technology was developed and successfully applied for production of II-VI semiconductor crystals, such as CdSe [19]. Unfortunately, the application of such precipitated structures with an excellent quality and size dispersion is primarily inhibited by the difficulty of embedding them in a conducting matrix material. As a solution of this problem, the use of conventional technological materials, i.e. insulating silicates, is possible. But it enavitably decreases the possibility of electric injection and so the use of colloidal nanoparticles

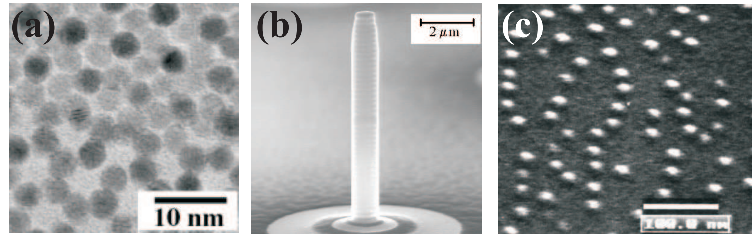

Figure 2: Examples of quantum dot structures fabricated by colloidal synthesis (a); ion beam lithography (b); self-organized epitaxial growth (c).

in opto-electronic devices.

One of the widely used modern QD fabrication processes is based on the artificial patterning of thin layer structures in three-dimensional regions. This technique uses different lithographic processes, such as optical lithography, X-ray lithography, electron and focused ion beam lithography. The main advantage of this techniques is relatively straightforward way QD fabrication and the possibility of almost arbitrary QD shape design. The patterning is realized in periodically following steps of masking and etching of the 2D layer systems with quantum well properties. In this way, a periodic array of 3D QD structures (microposts) can be fabricated [20],[21]. The key problem of this technique is the maximum achievable lateral resolution which varies from 100 nm for optical lithography down to 10-20 nm for X-ray and focused electron/ion beam techniques. The control of masking processes on the nm-scale requires a large number of technological steps and expensive equipment.

As an alternative method for QD fabrication, the effect of three dimensional self-organization during epitaxial growth of highly lattice-mismatched structures can be used. In this method, structure grown on the substrate with the relative lattice mismatch of more then 1% accommodates the minimum strain energy state by formation of 3D conglomerates. In order to achieve the best performance for QD devices the Stranski-Krastanov growth mode (see section I.4) is used to enable the coherent connection on the interface between the self-assembled 3D islands and the substrate. The main advantage of the self-organisation process is its simplicity and low production cost turning this technique into the most promising fabrication technology for the modern and future opto-electronic devices. Of course, the difficulties of this technique such as variable island chemical composition, island size fluctuations and distribution, represent challenging problems that still remain to be solved [22].

The investigation made in this thesis is primarily related to the development of self-organisation QD growth technique, and in particular to the monitoring of the structural properties of SK-grown InAs islands prepared in SK-growth mode.

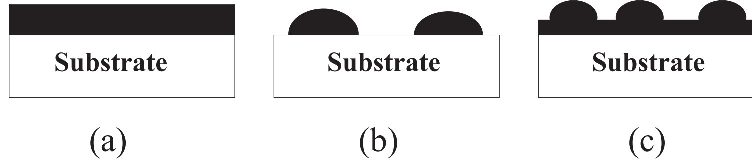

Figure 3: Schematic diagram of main epitaxial growth modes: Frank-van der Merwe (a); Volmer-Weber (b); Stranski-Krastanov (c).

I.4 Regimes of epitaxial growth

In this section the basic principles of epitaxial growth will be described (Fig. 3). In lattice-matched systems (self-epitaxy), the growth of deposited material is primarily determined by values of material γ_2 and substrate γ_1 surface energies and the energy of material/substrate interface γ_{12}. If condition $\gamma_2+\gamma_{12} < \gamma_1$ is fulfilled, the deposited material wets the substrate leading to layer-by-layer, or Frank-van der Merwe growth mode [23]. The changes in $\gamma_2 + \gamma_{12}$ can lead to a weak wetting effect and formation of decoupled 3D conglomerates of deposited material. In this situation the Volmer - Weber growth takes place [24]. In the case of lattice mismatched heterostructures ($>>$1% mismatch) with small interface energies, initial growth mode is layer-by-layer. Then with increasing layer thickness the misfit strain energy γ_{el} becomes dominant, leading either to the plastic relaxation of epilayer by means of misfit dislocations after some critical layer thickness h_c is reached, or to the γ_{el} reduction by means of isolated island formation. If the layer-by-layer growth proceeds in 3D island growth the Stranski-Krastanov (SK) mode dominates [25]. Islands formed in the SK growth mode can be both dislocated and elastically strained. The border between elastic relaxation and plastic deformation of the SK-island is mainly determined by the amount of island elastic strain energy. This energy value depends on the island shape and the island volume. In other words, the volume of islands determines their strain state. With increasing island volume the plastic deformation becomes an alternative mechanism of island stress relaxation. Depending on the energetic conditions of the SK-system the volume of deposited material can induce the change of growth modes from layer growth to coherent elastic or dislocated island growth. The formation of an island from a uniform film is accompanied by a relaxation of elastic energy of the epilayer, $\Delta E^V_{elastic} < 0$ and by a change of the film surface area, $\Delta A > 0$. This changes proceed by 3D island formation and disappearance of certain areas of a planar epilayer surface. The change of surface energy in this case is assumed to be positive, $\Delta E_{surf} > 0$. The morphology of resulting system is determined by the relation between the value of ΔE_{surf} and the energy of the dislocated island/substrate interface E_{disl}. Based on this principle, the SK-growth mode can be represented by a diagram (Fig. 4) showing the dependence of the parameter $\Gamma = E_{disl}/\Delta E_{surf}$ on the

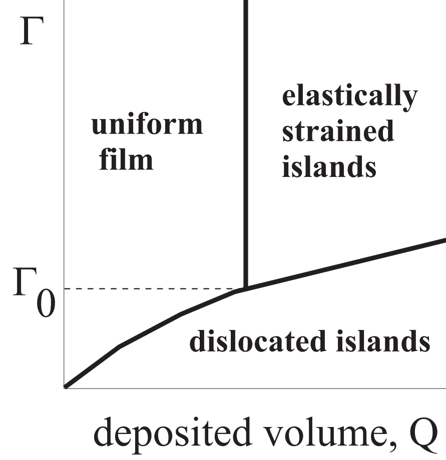

Figure 4: The diagram showing the preferred film morphology as a function of the amount of deposited material Q, and the quantity $\Gamma = E_{disl}/\Delta E_{surf}$, where ΔE_{surf} is the change of the surface energy due to island formation and E_{disl} is the energy of the dislocated island(film)/substrate interface.

deposited material volume Q [26].

If ΔE_{surf} is large, or the energy of the dislocated interface is relatively small, the corresponding value Γ is smaller than critical value Γ_0 limiting the formation of elastically strained islands. In this case the increase of the deposited material volume will proceed in dislocated island growth (dislocated film for low lattice mismatch). If ΔE_{surf} is smaller than E_{disl} the corresponding Γ value is larger then Γ_0. With the increase of the amount of the deposited material, a transformation from layer to elastically strained (coherent) islands occurs. The surface energy change due to the formation of coherent islands can be written as:

$$E_{island} = E_{edges} + \Delta E_{surf} - E_{relax} \tag{I.3}$$

where E_{edges} is a short-range energy of island edges, ΔE_{surf} is the gain of surface energy due to island formation, and E_{relax} - is the energy of elastic relaxation of the island volume strain. The different energy terms in Eq. I.3 depend on the linear island dimension L in the following way:

$$E_{edges} = AL, \quad \Delta E_{surf} = BL^2, \quad E_{relax} = CL^3 \tag{I.4}$$

with A,B and C - proportionality coefficients. If the surface energy gain dominates over E_{edges}, the formation of coherently strained islands is only possible for islands larger than the *critical island size* $L_{crit} = (2B)/(3C)$. Smaller islands if formed due to kinetic process will not grow and lose atoms to larger islands via diffusion. Once islands larger than L_{crit} are formed, they are assumed to reduce their overall surface

undergoing the so-called *Ostwald ripening* process [27]. The ripening process implies the further growth of large islands at the expense of the evaporation of small coherent islands. Islands undergoing ripening are assumed to possess dislocations [28].

I.5 Molecular beam epitaxy of quantum dots

The SK-growth of quantum dot semiconductor heterostructures is usually realized using *molecular beam epitaxy* (MBE) under ultra-high-vacuum (UHV) conditions.

The *solid-source* MBE technique is the main method for preparation of quantum dots. Here ultra-pure elements - in the case of interest indium (In) / gallium (Ga)/ aluminium (Al) and arsenic (As) - are heated in separate temperature-controlled quasi-knudsen effusion cells until the correct vapor pressure for the required growth conditions is achieved. The evaporated atoms or molecules condense on the single-crystal substrate, usually an n-doped GaAs(001) wafer, where they react with each other building the desired compounds, i.e. InAs, AlAs, GaAs, which then act as building blocks for the film/island growth.

In MBE method the term "beam epitaxy" means that evaporated atoms do not interact with each other, or any other residual gases until they reach the substrate. This is possible due to the large mean free path lengths of the beams in the highly evacuated vacuum chamber. The deposition rates are usually in time scale of 0.01-0.1 ML/sec (sub-monolayers). For this reason computer controlled shutters regulating the outgoing material flux are used. RHEED (Reflection High Energy Electron Diffraction) is used for *in-situ* monitoring of the overlayer material.

The SK-island samples described in this thesis were prepared in the following way. After thermal oxide desorption, a $\approx$ 200nm-thick GaAs buffer was grown on the wafer at a temperature of $600°C$. The deposition of Ga (further In or Al) proceeded under a partial pressure of As_4 gas of the order of $10^{-5} - 10^{-6}$ mbar.

The formation of the characteristic 2x4 GaAs(001) reconstruction was verified by the formation of diffraction streaks in the RHEED pattern indicating the cleanliness of the substrate surface. After this, the substrate temperature was reduced to the region between 470 and $530°C$, which are the limiting temperatures for the formation of homogeneous InAs island structures [29]. This results in a change of the GaAs surface reconstruction to a c(4x4) RHEED pattern, shown in Fig. 5(a). If the InAs growth on AlAs(001) substrate was investigated, an AlAs buffer layer of thickness $\approx$ 5nm was predeposited pseudomorphycally before the InAs deposition started. After the Indium source shutter is opened, the GaAs reconstruction features immediately disappear, and the RHEED pattern indicated a degraded two-dimensional surface morphology (Fig. 5(b)). This situation was maintained until the transition from 2D to 3D InAs growth took place. At this point, the 2D diffraction spots disappear (Fig. 5(c)) before new 3D-type diffraction spots emerge. After that the RHEED pattern exhibits the 3D diffraction spots decorated with additional weak intensity tails (Fig. 5(d)), called

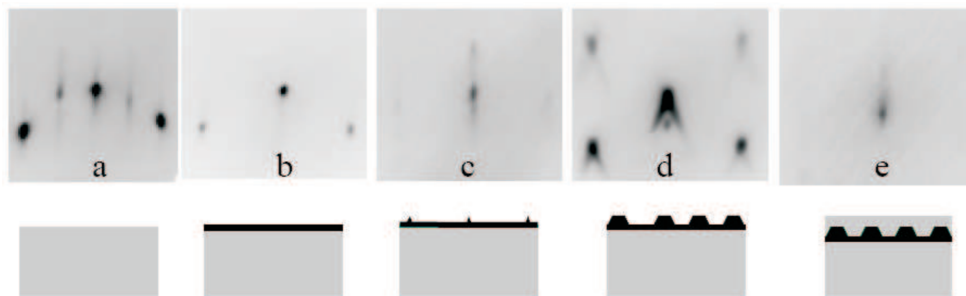

Figure 5: *In-situ* RHEED patterns observed during MBE growth of InAs on GaAs (001). (a) c(4x4) reconstructed GaAs substrate at 500°C; (b) start of InAs growth; (c) transition from 2D to 3D growth; (d) end of 3D growth; (e) after deposition of the GaAs capping layer. Taken from [30].

chevrons being the main indication for 2D-to-3D transition of the growth mode from layer to island growth. After the 3D transition was observed for uncapped islands (rough capping layer pattern for buried islands) the wafer was cooled down to room temperature.

In the case of buried dots, the 3D InAs layer was covered after approximately 30s time delay with a 30-nm GaAs(AlAs) cap at the same substrate temperature as for InAs layer deposition. The corresponding RHEED pattern is shown in Fig. 5(e).

I.6 Special features of the island growth in InAs/GaAs(001) and InAs/AlAs(001) systems

The process of island growth during InAs deposition on GaAs(001) and AlAs(001) substrates can be divided into two main stages. In the first stage (see Fig. 6(a)), starting from the moment of wetting layer completion, the formation of homogeneous presumably defect-free nanoscale SK-islands with a narrow size distribution takes place [31].

For InAs/ GaAs(001) and InAs/ AlAs(001), the process of island formation within this stage exhibits significant differences. In the case of InAs growth on GaAs(001) under particular growth conditions the formation of islands with a nearly constant size takes place. The addition of incoming InAs material seems to influence only the surface density of the islands, until it reaches some "critical" density value, at which point the first stage of island growth is completed [32].

In the case of InAs/AlAs(001) system, during the entire process the island surface density remains rather constant [33]. The addition of InAs mainly influences the size of the islands. The first stage is completed when particular "critical" island

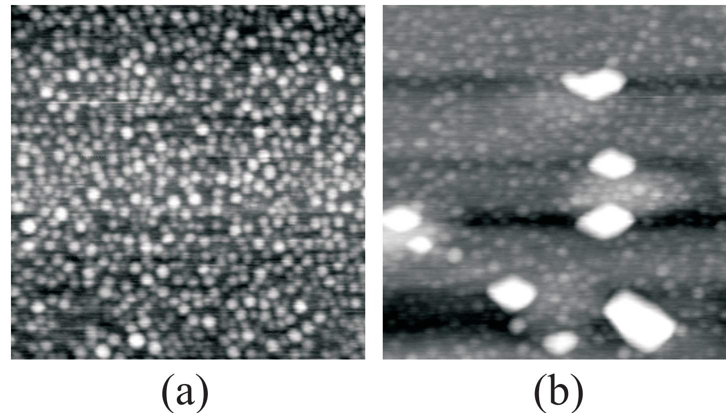

Figure 6: AFM images ($1\mu m^2$) of surface topography after deposition of (a) 2.4ML, and (b) 3ML on the AlAs(001) substrate surface at 500°C.

dimensions are exceeded.

In the second stage the change of surface topography proceeds similarly for both systems (see Fig. 6(b)). At the beginning of this stage the formation of homogeneous 3D islands stops. The incoming InAs is not incorporated any more in the already developed homogeneous islands and further growth proceeds by means of formation of larger island conglomerates [34],[28]. The initial surface density of islands formed before the beginning of second growth stage remains unchanged during the further material deposition.

According to the main features characterizing the resulting surface topography, the first and second stages of InAs growth in this work will be denoted as stage of *homogeneous growth* and the *coalescence stage*.

Switching from one growth mode to another is a multi-parameter process depending on different deposition conditions such as material flux, growth temperature, partial As pressure, etc. [22], [35] and was determined using experimental trial-and-error procedures. In this work the particular attention will be paid to both island growth stages in InAs/GaAs(001) and InAs/AlAs(001) systems.

I.7 X-ray diffraction on quantum dots: advantages of synchrotron radiation

Studies in the field of X-ray crystallography were initiated at the beginning of 20th century. Low-power, X-ray laboratory sources, *X-ray tubes*, were used. In an X-ray tube radiation is created by an electron beam accelerated in vacuum toward a metal target. The interaction of the high energy electrons with the target material leads to

two types of radiation. One component is the *Bremsstrahlung*, the spectrum with a continuous energy distribution with onset wavelength of:

$$\lambda_{min} = 12.4/U[\mathring{A}] \tag{I.5}$$

where U is the acceleration voltage in keV. Second part is the *characteristic* radiation from excited inner K-shell electrons of the target material. The relative intensity of the characteristic radiation is four orders of magnitude higher than the Bremsstrahlung. Using the X-ray characteristic radiation and standard slit systems for beam collimation, the lab sources are good tools for the investigation of macroscopic polycrystalline and powder samples. Of course, the reduction of size of investigated objects to thin and ultra-thin films and nanocrystals accompanied with a progress in lithographic technologies have set new challenges for X-ray structural analysis. For the investigation of these new objects higher measurement resolution is required. The usage of smaller slit apertures could provide the necessary beam divergence but only at the expense of incoming photon flux, making the standard lab X-ray sources unsuitable for this kind of research.

Synchrotron X-ray radiation has shown itself as a more prospective for the modern solid body structure analysis. Synchrotron radiation is emitted from the high-energy electrons (positrons) moving within a storage ring whenever their are accelerated. In the second-generation synchrotron sources the radiation is produced with the help of *bending magnets*. In third-generation synchrotron sources, the so-called *insertion devices* (*wigglers* and *undulators*) are installed to improve the source properties. The emission spectrum of synchrotron is well defined. Its calculation is based on a knowledge of the bending radius R and the kinetic energy of the electrons (positrons) E_{el}. The spectrum is characterized by the critical energy E_c, given by:

$$E_c = 3hc/(4\pi R) \cdot (E_{el}/m_0c^2) \tag{I.6}$$

where m_0c^2 is the rest mass energy of a relativistic particle. The emission spectrum increases continuously up to the critical energy E_c and then decreases rapidly beyond.

Different X-ray sources are usually compared by specifying the brilliance, characterizing the quality of the emitted radiation defined by:

$$brilliance = \frac{dN/dt}{mrad^2 \cdot mm^2 \cdot 0.1\%\, energy\ interval} \tag{I.7}$$

The brilliance describes the number of photons N emitted in one second from a source area of 1mm^2 into a radiation cone defined by the special opening angle of 1mrad^2 and normalized on a spectral bandwidth of 0.1% [36].

In terms of brilliance even the very-first synchrotron radiation sources were already 1000 times more powerful than X-ray tube sources. Together with the fact, that the synchrotron radiation energy can be easily chosen in the almost whole X-ray spectrum

it brought a host of advantages for material structure analysis. It is possible to focus the synchrotron X-ray beam in such a way that all beam intensity could be brought to bear on a very small crystal.

Concerning the diffraction experiments presented in this work, the major advantage of synchrotron radiation is its high brilliance, since for diffraction on quantum dot samples it is necessary to provide a narrow collimated incident beam while maintaining a sufficient intensity and angular resolution to resolve closely spaced diffraction spots on diffuse scattering pattern. The higher intensity and good collimation of the probing synchrotron X-ray beam are essential for performing diffraction experiment on quantum dot structures.

Chapter II

Fundamentals of diffraction theory

Modern X-ray crystallography is a well established field [48],[49],[50]. In general, the theory describing the scattering of X-rays by an arbitrary object is quite complicated. In this chapter, on the contrary, the only several aspects will be summarized being of main importance in the frame of this work.

Below the theory describing the X-ray scattering on a perfectly periodic crystal and on the crystal with small (elastic) distortions together with the special features of the grazing incidence geometry will be shortly overviewed.

II.1 Scattering of X-ray photons

Since many decades the phenomena of X-ray scattering on solids has become a separated field of structure analysis. From the mathematical point of view the diffraction experiment with high-energy electromagnetic waves on a system of atoms is the problem of finding the wave front and resulting intensity distribution formed in the process of scattering. For the solution of physical problems the reverse calculation with determination of the structure (position of elemental scatterers) of an object from the experimentally observed diffraction field is necessary.

In the model scattering process the coherent X-ray radiation with energy $E = h \cdot \nu$, where h is Planck's constant[1] and ν is the radiation frequency, go through the assembly of point scatterers (atoms). The point scatterers interact with the incident waves, scattering them. The direction of wave propagation is defined by the wave vector $\mathbf{k}$, whose modulus is equal to:

$$|\mathbf{k}| = \frac{2 \cdot \pi}{\lambda} \tag{II.1}$$

where λ is the wavelength connected with the radiation frequency by:

$$\lambda = \frac{c}{\nu}, \tag{II.2}$$

[1] $h = 6.626068 \cdot 10^{-34} \frac{m^2 \cdot kg}{sec}$

where c is the speed of light in vacuum [2]. Frequently, the incoming monochromatic wave is assumed to be a plane wave:

$$E = E_0 \cdot \exp(i(\mathbf{k} \cdot \mathbf{r}) + C)) \tag{II.3}$$

where E_0 is the wave amplitude, $\mathbf{r}$ is the radius vector of the point of space, and C is the initial phase. The expression (II.3) does not include time as a parameter because as a result one is interested in the diffraction pattern at any arbitrary moment of time. This assumption is sufficient for establishing the relative phase difference arising in interference of scattering waves, since this difference depends exclusively on the spatial arrangement of scatterers and is time independent. The scattering of the radiation by the object can be *elastic* or *inelastic.* In the case of elastic scattering the interaction between atom and incoming wave proceeds *without* any loss of energy (no wavelength changes). On the contrary, in the inelastic case the energy of the scattered wave is *different* from its initial value. In general, the scattering process is assumed to be elastic and its resulting diffraction pattern is used to determine the spatial arrangement of atoms.

II.2 Scattering amplitude

In general approach, secondary waves coming from all points of the object are considered. Consider the object consisting of two point scatterers *O* and *O'* (Fig. 1). The origin in the local coordinate system is chosen to be on one of the points. The relative position of scattering points is given by vector $\mathbf{r}$. The incident plane wave excite this centers and each of them becomes the source of a secondary spherical wave. The initial wave arrives at both centers with different phases leading to a phase difference of the scattered waves. Depending on relative phase difference both diffracted waves will interfere constructively or destructively. Of course, these changes of resulting amplitude will only be significant if the wavelength of the incoming radiation is comparable to the distance between scattering points defined by $\mathbf{r}$. The typical distance between scatterers (atoms) in solids is in the order of $3\mathring{A}$, so to create interference effects *only* radiation in the hard X-ray spectrum ($\lambda_{X-ray} \approx 1\mathring{A}$) is suitable.

In Fig. 1 the path difference between waves scatted in the same direction by the points at positions 0 and $\mathbf{r}$ is equal to:

$$\mathbf{k} \cdot \mathbf{r} - \mathbf{k_0} \cdot \mathbf{r} = (\mathbf{k} - \mathbf{k_0}) \cdot \mathbf{r} \tag{II.4}$$

So, in the case of a primary wave with unit amplitude ($E_0 = 1$), the scattering at point $\mathbf{r}$ will produce a wave:

$$f \cdot \exp[i(\mathbf{k} - \mathbf{k_0}) \cdot \mathbf{r}] = f \cdot \exp[2\pi i(\mathbf{S} \cdot \mathbf{r})] \tag{II.5}$$

[2] c=299792458 $\frac{m}{sec}$

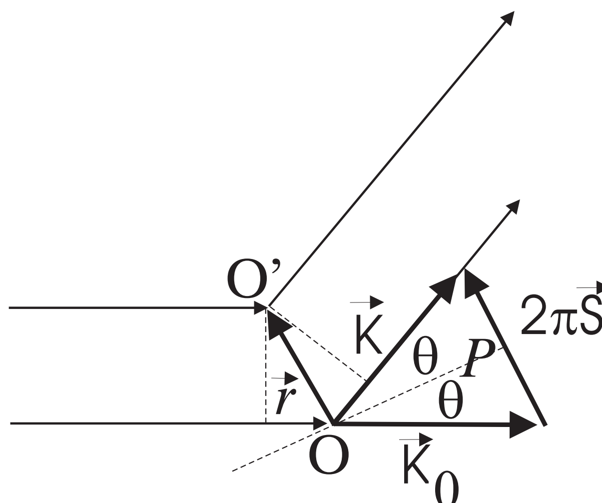

Figure 1: Scattering schema with two point centers.

where f is the scattering factor, and **S** is the vector perpendicular to plane P (see Fig. 1) with respect to which the scattering angle 2θ can be measured.

$$\mathbf{S} = \frac{\mathbf{k} - \mathbf{k_0}}{2\pi}; |\mathbf{S}| = \frac{2\sin(\theta)}{\lambda} \quad \text{(II.6)}$$

If the object placed in the path of the initial wave consists of n scattering centers with scattering power f_i, located at points $\mathbf{r_j}$, the resulting amplitude of the scattering wave will be:

$$\sum_{j=1}^{n} f_i \cdot \exp[2\pi i(\mathbf{S} \cdot \mathbf{r_j})] = F(\mathbf{S}) \quad \text{(II.7)}$$

The quantity F(**S**) is called the *scattering amplitude* of a given object. For a "point" scattering center, the quantity f_i is constant and independent on **S**. In the general concept of the scattering power f of a given center any type of physical scattering unit can be used, i.e. atom, molecule, group of molecules, etc.

If the scattering process on an atom is considered, the elastic wave-atom interaction can be split into two processes: the scattering by *atomic nuclei* and *electrons*. Both nuclei and electrons oscillating in the electric field of the primary wave become the sources of a secondary scattered waves of the same frequency as the incident wave. The scattering power is inverse proportional to the mass of the scatterer. Taking into account the nuclei/electron mass difference, $m_{nuclei}/m_{electron} \approx 1840$, the scattering from the nuclei can be neglected and so, *only* the scattering power of the electrons in

the atom have to be taken into account:

$$F_e = \frac{1}{R} \cdot \frac{e^2}{(mc)^2} \cdot \sin(\phi) \tag{II.8}$$

where R is the distance from the scattering center to the point of observation, e and m are the charge and the mass of the electron, c is the velocity of light, and ϕ - is the so-called polarization angle, describing the polarization of the incident wave. To express the scattering amplitude in absolute units, the scattering amplitude of the object should be multiplied by the the factor F_e:

$$F_{abs}(\mathbf{S}) = F(\mathbf{S}) \cdot F_e \tag{II.9}$$

II.3 Electron density. Fourier Integral.

Instead of a discrete set of points n at positions $\mathbf{r_j}$ one can consider a continuous distribution of scattering power of the object. Since, as shown previously, the X-rays are mainly scattered by electrons, the "continuously scattering matter" is in this case the time-averaged electron density $\rho(\mathbf{r})$ of the object. This function can be presented as an average number of electrons $n_e(\mathbf{r})$ in a volume element $\delta V_{\mathbf{r}}$ at the point $\mathbf{r}$ and divided by the volume element:

$$\rho(\mathbf{r}) = n_e(\mathbf{r})/\delta V_{\mathbf{r}} \tag{II.10}$$

From the quantum-mechanical point of view this time-averaged electron density is equal to the wave-function of an object squared

$$\rho(\mathbf{r}) = |\psi(\mathbf{r})|^2 \tag{II.11}$$

In this approach, the sum over discrete scattering centers in (II.7) must be replaced by an integral over the continuous function $\rho(\mathbf{r})$:

$$\begin{aligned} F(\mathbf{S}) &= \int \rho(\mathbf{r}) \cdot \exp([2\pi i(\mathbf{S} \cdot \mathbf{r})])\, dV_{\mathbf{r}} = \\ &= \iiint_{x,y,z=-\infty}^{+\infty} \rho(x,y,z) \cdot \exp([2\pi i(xX + yY + zZ)])\, dx\, dy\, dz = \\ &= \mathscr{F}[\rho] \end{aligned} \tag{II.12}$$

where $dV_{\mathbf{r}}$ is an element of the scattering volume, X, Y, Z are three coordinates of vector $\mathbf{S}$, and $\mathscr{F}$ is the *Fourier integral operator*. The equation (II.12) assigns the scattering amplitude as a function of $\mathbf{S}$ and defines scattering in any direction in *reciprocal space*:

$$\mathbf{k} = \mathbf{k_0} + 2\pi \cdot \mathbf{S}(X,Y,Z) \tag{II.13}$$

In this case F(**S**) is the reciprocal "image" of a function $\rho(\mathbf{r})$, describing the object structure in the direct space and in one-to-one correspondence with it. The integral (II.12) is suitable to describe diffraction phenomena for objects with inhomogeneities comparable to the wavelength of incoming radiation.

II.4 Scattering by a single atom. Atomic amplitude.

The atomic amplitude defines the scattering by the single atom, where $\rho_a(\mathbf{r})$ is the electron distribution function of an object given by electron density of the atom in Eq.(II.12). The atomic form factor can be written as:

$$f(\mathbf{S}) = \int \rho_a(\mathbf{r}) \cdot \exp[2\pi i(\mathbf{S} \cdot \mathbf{r})]\, dV_{\mathbf{r}} \quad \text{(II.14)}$$

To a sufficiently good approximation, the inner electron shells of atoms are spherically symmetric, so $\rho_a(\mathbf{r}) = \rho_a(r)$ and the integral (II.12) can be written in spherical coordinates:

$$f(s) = \int_0^\infty 4\pi\, r^2\, \rho_a(r)\, \frac{\sin(s \cdot r)}{s \cdot r}\, dr \quad \text{(II.15)}$$

where $s = 2\pi\, \mathbf{S} = 4\pi \frac{sin(\theta)}{\lambda}$. For the vast majority of cases the spherical approximation is sufficient, and so if $s \to 0$ then $\frac{sin(s \cdot r)}{s \cdot r} \to 1$ and:

$$f(0) = \int \rho_a(\mathbf{r})\, dV_{\mathbf{r}} = \mathbf{Z} \quad \text{(II.16)}$$

This means, that for zero scattering angle the atomic amplitude is simply the atomic number. As the scattering angle increases, the function $f(\frac{sin(\theta)}{\lambda})$ decreases. Such functions are called *f-functions* and can be calculated from the electron distributions of the atom. The direct determination of the electron density distribution is a relatively complicated process. For numerical calculation, the relatively reliable approximation of *Cromer and Mann* [37] can be used, where the angular dependence of the atomic scattering factor is represented by a 9-parameter equation:

$$f(\frac{\sin(\theta)}{\lambda}) \approx \sum_{i=1}^{4} a_i \cdot \exp[-b_i \cdot (\frac{\sin(\theta)}{\lambda})^2] + c \quad \text{(II.17)}$$

with a_{1-4}, b_{1-4} and c as coefficients, tabulated for each specific atom in the *International Tables for Crystallography* [38]. All 9 coefficients for atoms considered in this work are given in tab. II.1. If the energy of the incident radiation is close to

atom	a_1	a_2	a_3	a_4	b_1	b_2	b_3	b_4	c
^{49}In	19.1624	18.5596	4.2948	2.0396	0.5476	6.3776	25.8499	92.8029	4.9391
^{13}Al	6.4202	3.0387	1.9002	0.7426	1.5936	31.5472	1.9646	85.0886	1.1151
^{31}Ga	15.2354	6.7006	4.3591	2.9623	3.0669	0.2412	10.7805	61.4135	1.7189
^{23}As	16.6723	6.0701	3.4313	4.2779	2.6345	0.2647	12.9479	47.7972	2.531

Table II.1: Cromer and Mann coefficients (II.17), used for the numerical calculations presented in following chapters.

atom	f' (10keV)	f"(10keV)
^{49}In	8.71859E-02	3.78407
^{13}Al	1.71425E-01	1.77072E-01
^{31}Ga	-2.28343	-5.78347E-01
^{23}As	-1.39878	7.52429E-01

Table II.2: Correction coefficients of resonance interaction and absorption for 10 keV.

the absorption edge of the respective atom then the effects of resonance interaction [39], *f'* , and imaginary absorption part [40], *f"*, have to be included in the atomic scattering factor calculations:

$$f_a = f(\frac{\sin(\theta)}{\lambda}) + f' + i \cdot f'' \tag{II.18}$$

Both *f'* and *f"* coefficients are also tabulated for each particular photon energy. For 10keV radiation energy used in present experiments the coefficients are given in Table II.2 .

To calculate the scattering power of a molecule, the sum has to be made over the waves scattered by atoms in the molecule in Eq.(II.7):

$$f_{mol} = \sum_{j=1}^{n} f_a \cdot \exp[2\pi i\,(\mathbf{S} \cdot \mathbf{R_j})], \tag{II.19}$$

where $\mathbf{R_j}$ describes the positions of the individual atoms. For numerical calculation of scattering power of the alloy of composition $A_xB_{1-x}C$ build from molecules AC and BC the *Vineyard approximation* [41], [3] can be used.

$$f_{A_xB_{1-x}C} = (f_{AB} - f_{AC}) \cdot x + f_{AC} = f_{AB} \cdot x + f_{AC} \cdot (1-x) \tag{II.20}$$

[3] assuming a linear change of the scattering factor of the alloy with concentration x

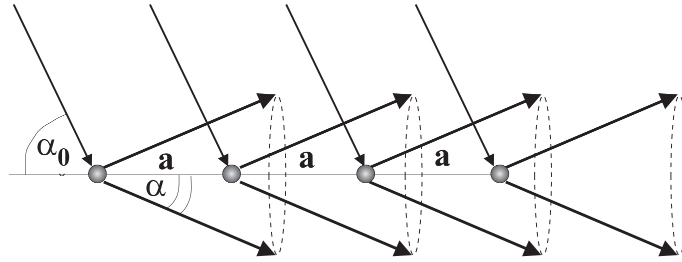

Figure 2: Diffraction from a one-dimensional periodic row of points

II.5 Diffraction from a periodic lattice

II.5.1 Crystal periodicity. Reciprocal lattice

By definition definition a crystal is a homogenous solid formed by a repeating three-dimensional pattern of atoms, ions, or molecules. The periodicity of the crystal in real space is characterized by the translation (lattice) vector:

$$\mathbf{t} = \mathbf{a_1} \cdot m + \mathbf{a_2} \cdot n + \mathbf{a_3} \cdot p \tag{II.21}$$

where the crystal in each point can be reproduced by the translation of its unit cell - the smallest crystal unit built by basis vectors $\mathbf{a_1}$, $\mathbf{a_2}$, $\mathbf{a_3}$ whose size is determined by the absolute values of these vectors - in three dimensions multiplying the unit cell vectors with integer numbers m, n and p. For a one-dimensional periodic crystal with lattice period a (Fig. 2) for a monochromatic X-ray wave incident at angle α_0 on each of the lattice atoms it will give a maximum scattered amplitude when:

$$a\,(\cos(\alpha) - \cos(\alpha_0)) = h \cdot \lambda \tag{II.22}$$

where α is the angle of scattering and h is an integer. The scattering is assumed to be cylindrically symmetrical, so that scattered beams form cones about the axis of the 1D atomic lattice.

The condition described by Eq.(II.22) is the *Laue criteria* for diffraction. If a 3D periodic lattice is considered the Laue condition should be simultaneously fulfilled in all three directions, $\mathbf{a_1}$, $\mathbf{a_2}$, $\mathbf{a_3}$. This means that only those reflections are possible which correspond to the lines of intersection of all three cones. In this case the Laue condition is:

$$\begin{aligned}
\mathbf{a_1}\,(\mathbf{k} - \mathbf{k_0}) &= 2\pi\, h, \text{ or } \mathbf{a_1} \cdot \mathbf{S_1} = h \\
\mathbf{a_2}\,(\mathbf{k} - \mathbf{k_0}) &= 2\pi\, k, \text{ or } \mathbf{a_2} \cdot \mathbf{S_2} = k \\
\mathbf{a_3}\,(\mathbf{k} - \mathbf{k_0}) &= 2\pi\, l, \text{ or } \mathbf{a_3} \cdot \mathbf{S_3} = l
\end{aligned} \tag{II.23}$$

Rewriting Eq.(II.23) as:

$$\mathbf{S} = \mathbf{S_1} + \mathbf{S_2} + \mathbf{S_3} = h\,\mathbf{a_1^*} + k\,\mathbf{a_2^*} + l\,\mathbf{a_3^*} = H_{hkl} \tag{II.24}$$

defines the *reciprocal lattice* vector $\mathbf{H_{hkl}}$. The unit vectors $\mathbf{a^*_{1-3}}$ of the reciprocal lattice are related to the unit vectors $\mathbf{a_{1-3}}$ in real space by:

$$\begin{aligned}
\mathbf{a_1^*}\cdot\mathbf{a_1} &= 2\pi,\ \mathbf{a_2^*}\cdot\mathbf{a_1} = 0,\ \mathbf{a_3^*}\cdot\mathbf{a_1} = 0\\
\mathbf{a_1^*}\cdot\mathbf{a_2} &= 0,\ \mathbf{a_2^*}\cdot\mathbf{a_2} = 2\pi,\ \mathbf{a_3^*}\cdot\mathbf{a_2} = 0\\
\mathbf{a_1^*}\cdot\mathbf{a_3} &= 0,\ \mathbf{a_2^*}\cdot\mathbf{a_3} = 0,\ \mathbf{a_3^*}\cdot\mathbf{a_3} = 2\pi
\end{aligned} \tag{II.25}$$

Replacing the diffraction vector $\mathbf{S}$ by $\mathbf{H_{hkl}}$ one can write the diffraction law as:

$$\mathbf{k} = \mathbf{k_0} + 2\pi\,\mathbf{H_{hkl}} \tag{II.26}$$

An infinite point lattice in real space is described by:

$$T(\mathbf{r}) = \sum_{m,n,p=-\infty}^{+\infty} \delta(\mathbf{r} - \mathbf{t}(m,n,p)), \tag{II.27}$$

where δ is *delta-function.* For infinite crystal, in which each unit cell has an electron density of $\rho_{cell}(\mathbf{r})$, can be written as a convolution:

$$\rho_\infty(\mathbf{r}) = \rho_{cell}(\mathbf{r})\cdot T(\mathbf{r}) \tag{II.28}$$

If the function $\rho_\infty(\mathbf{r})$ is arbitrary, then F($\mathbf{S}$) in Eq.(II.12) may exist at all values of $\mathbf{S}$. If the function $\rho_\infty(\mathbf{r})$ is periodic, then integral (II.12) can be taken over one period and is nonzero only at discrete values of $\mathbf{S} = \mathbf{H_{hkl}}$:

$$\begin{aligned}
F(\mathbf{S}) &= F_{hkl} = \int \rho(\mathbf{r})\cdot\exp[2\pi i\,(\mathbf{H_{hkl}}\cdot\mathbf{r})]\,dV_{\mathbf{r}} =\\
&= \int_0^{a_1}\int_0^{a_2}\int_0^{a3} \rho(x,y,z)\,\exp[2\pi i\,(\frac{h}{a_1}x + \frac{k}{a_2}y + \frac{l}{a_3}z)]\,dx\,dy\,dz
\end{aligned} \tag{II.29}$$

where a_1, a_2, a_3 are the absolute values of the lattice unit vectors $\mathbf{a_{1-3}}$ and define the lattice period in three main directions, and h, k, l are integers. For an infinite crystal with allowed values of scattering amplitude, F_{hkl}, the total scattering amplitude can be written as:

$$F_\infty(\mathbf{S}) = \sum_{hkl} \frac{F_{hkl}}{\gamma}\,\delta(\mathbf{S} - \mathbf{H_{hkl}}) \tag{II.30}$$

where γ is volume of the crystal unit cell. The last equation defines the periodic set of nodes in the reciprocal lattice, each described by a delta function and placed at

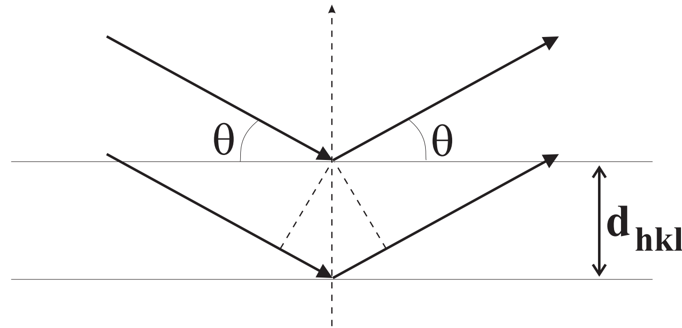

Figure 3: Bragg diffraction conditions.

the end of vector $\mathbf{H_{hkl}}$. The weight of each node is defined by the complex structure amplitude F_{hkl}. A particular atomic arrangement (relative atomic positions) within the crystal unit cell can significantly influence the values of F_{hkl} for particular sets of h, k, l. This effect is called the *geometrical structure factor* of the crystal unit cell and arises from electron density variations within the crystal unit cell (Eq.II.7). The destructive interference between waves scattered from the atoms in the unit cell lead to reduced intensity at particular values of H_{hkl} in reciprocal space. For instance, in the case of a base-centered cubic (*bcc*) cell the destructive interference leads to intensity reduction at reciprocal points for which the sum $h + k + l$ is an odd integer. In the case of a face-centred cubic (*fcc*) cell the same effect is produced for the h, k, l indices being partially even or odd.

Materials like GaAs have a *zinc-blende* (ZB) structure, which is similar to the *diamond* structure but it has different atoms in the unit cell. Relative to *fcc* cell, in diamond cell only reflections with order $n/4$ are allowed. In ZB cell the reflections, which are forbidden for diamond cell, do not disappear completely. It makes the ZB-pattern a special case in between the case of fcc and diamond lattices.

II.5.2 Atomic planes. Braggs law.

If the crystal is perfectly periodic in all main directions it is called perfect or a *single* crystal. In this case one can describe the periodic arrangement of atoms by the *lattice planes*. In this case the conditions at which each particular lattice plane will diffract incoming X-ray beam can be derived using the usual *law of reflection*.

Consider a set of parallel lattice planes equally spaced distance d apart (Fig. 3). Suppose the incident waves to be reflected specularly and each plane reflects only a small fraction of the incoming radiation like a semi-transparent mirror. The total path difference between the X-rays reflected from adjacent planes is then $2\,d\,\sin(\theta)$, where θ is measured relative to the surface plane. Constructive interference of the reflected radiation occurs whenever the path difference is integer number n of wavelengths λ.

So that:

$$2\,d\,\sin(\theta) = n\,\lambda \tag{II.31}$$

This is the *Bragg* equation [42]. The Bragg equation as well as the Laue conditions indicates that diffracted beams can be obtained for given d_{hkl} in monochromatic radiation ($\lambda = const$) only by changing the crystal orientation relative to the incoming beam (angle θ). Since the reciprocal lattice was introduced as a set of points at the end of the vectors $\mathbf{H_{hkl}}$, these reciprocal points representing the reciprocal lattice planes are also indexed in three dimensional space with letters h, k and l. The absolute length of the normal vector H_{hkl} is then the inverse of interplanar distance d_{hkl}:

$$|\mathbf{H_{hkl}}| = 2\pi/d_{hkl} \tag{II.32}$$

So, in the case of diffraction from a perfect crystal, the point-maxima positions in reciprocal space, $\mathbf{S} = \mathbf{H_{hkl}}$, can be interpreted as a diffraction from particular crystal lattice planes (*hkl*) with spacing d_{hkl}. In this case Bragg law can be written as:

$$2k\sin(\theta) = |\mathbf{H_{hkl}}| \tag{II.33}$$

II.5.3 Ewald construction. Reflection sphere.

In order to construct graphically the diffraction conditions for particular points in reciprocal space the *Ewald construction* can be used (Fig. 4). For monochromatic radiation with $\mathbf{k_0}$ and $\mathbf{k}$ along the directions of the incident and scattered waves, the set of the ends of vectors $\mathbf{S}$ lies on the Ewald sphere with radius $|\mathbf{k}| = 1/\lambda$.

The construction with $\mathbf{k} = \mathbf{k_0}$ corresponds to the value of $\mathbf{S} = \mathbf{H_{000}} = 0$, describing the zero order node in reciprocal space. The diffraction conditions are primarily determined by the reciprocal lattice, built by unit vectors $\mathbf{a_1^*}$, $\mathbf{a_2^*}$ and $\mathbf{a_3^*}$ by orientation with respect to $\mathbf{k_0}$, and by the absolute value of vector $\mathbf{k}$. The conditions for the formation of a diffraction maximum at position with indices *hkl* consist in intersection by the reflection sphere with the node (*hkl*) of the reciprocal lattice, corresponding to condition $\mathbf{S} = \mathbf{H_{hkl}}$.

To summarize, with a monochromatic beam and a single crystal, then to investigate a particular allowed reflection *hkl* it is necessary to appropriately orient the crystal in respect to the incoming X-ray beam. Based on the Ewald construction, various diffraction geometries can be used to analyse the scattered intensity in the reciprocal lattice.

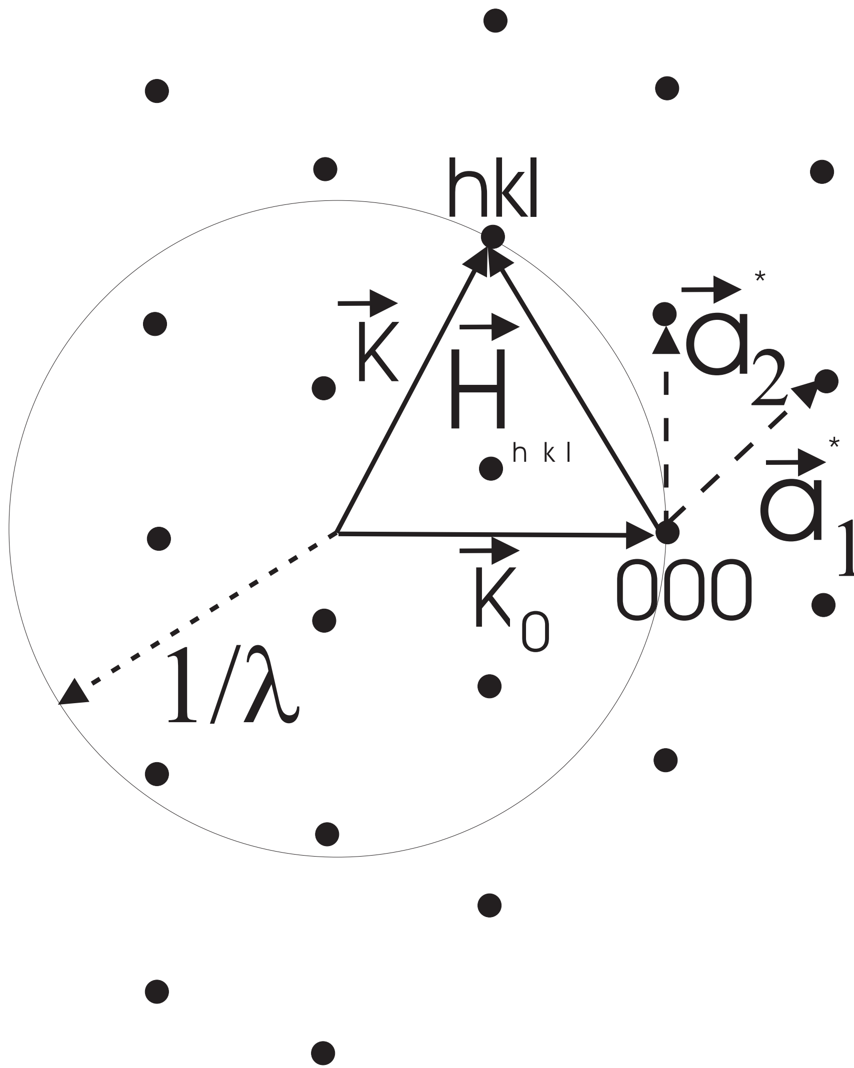

Figure 4: Ewald sphere in the reciprocal lattice of the crystal projected in the plane of the unit vectors $\mathbf{a_1^*}$ and $\mathbf{a_2^*}$.

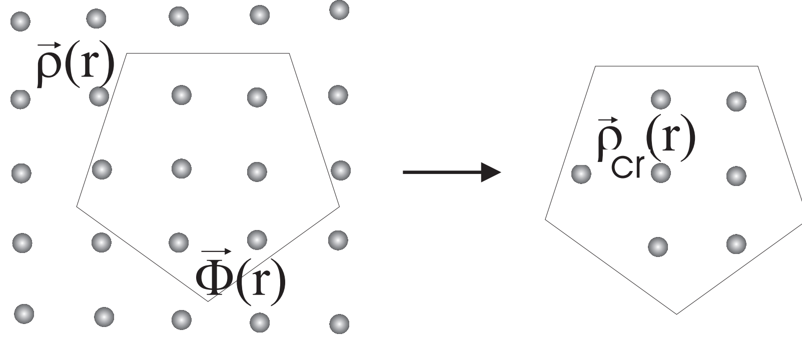

Figure 5: Schematic representation of the shape function.

II.6 Size of reciprocal lattice points. Shape function.

Equation (II.29) represents a concept where the infinite periodic function $\rho(\mathbf{r})$ is integrated over its periods at "point" nodes of the reciprocal lattice described by discrete indices h, k, l. A real crystal has finite dimensions and a defined shape and volume V. Depending on the crystal size *truncation* effects occur, where the nodes in reciprocal lattice are not points, described by delta function $\delta(\mathbf{S} - \mathbf{H_{hkl}})$, but have a finite size and defined shape. To take the finite size of the crystal into account a *shape function* (Fig. 5) is introduced:

$$\Phi(\mathbf{r}) = \begin{cases} 1 & \text{, inside the crystal} \\ 0 & \text{, outside the crystal} \end{cases} \tag{II.34}$$

In this case the electron density function $\rho(\mathbf{r})_{cr}$ is the product of the electron density function of the infinite crystal and its shape function:

$$\rho(\mathbf{r})_{cr} = \rho_\infty(\mathbf{r}) \cdot \Phi(\mathbf{r}) \tag{II.35}$$

The scattering amplitude of the infinite crystal is given by (II.30). The Fourier transform (amplitude) of the crystal shape is defined by:

$$D(\mathbf{S}) = \int_V \Phi(\mathbf{r}) \, \exp[2\pi i\,(\mathbf{S}\cdot\mathbf{r})]\, dV_{\mathbf{r}} = \int_\Phi \exp[2\pi i\,(\mathbf{S}\cdot\mathbf{r})]\, dV_{\mathbf{r}} \tag{II.36}$$

According to (II.35) the scattering amplitude of the finite crystal is given by:

$$F(\mathbf{S}) = [\sum_{hkl} \frac{F_{hkl}}{\gamma}\, \delta(\mathbf{S} - \mathbf{H_{hkl}})] \cdot D(\mathbf{S}) \tag{II.37}$$

Replacing $\delta(\mathbf{S}-\mathbf{H_{hkl}})\cdot D(\mathbf{S})$ by $D(\mathbf{S}-\mathbf{H_{hkl}})$ one describes the shape of each "point" of reciprocal space determined by H_{hkl}. The resulting scattering amplitude of a finite crystal now can be written as:

$$F_{cr}(\mathbf{S}) = \frac{1}{\gamma}\sum_{hkl} F_{hkl}\cdot D(\mathbf{S}-\mathbf{H_{hkl}}) \tag{II.38}$$

To demonstrate the effect of the crystal shape function on the size of a reciprocal lattice point a rectangular crystal with finite dimensions A_1, A_2 and A_3 can be considered. The shape part is then defined by:

$$\begin{aligned} D(\mathbf{S}) &= \int_{-A_1/2}^{A_1/2}\int_{-A_2/2}^{A_2/2}\int_{-A_3/2}^{A_3/2} \exp[2\pi i\,(xX+yY+zZ)]\,dx\,dy\,dz = \\ &= \frac{\sin(\pi A_1 X)}{\pi X}\cdot\frac{\sin(\pi A_2 Y)}{\pi Y}\cdot\frac{\sin(\pi A_3 Z)}{\pi Z} \end{aligned} \tag{II.39}$$

In this case the actual shape of the reciprocal node will be modulated by function $\frac{\sin(At)}{t}$, where A is the crystal size in particular direction of real space, in each of three main directions of reciprocal space. If the total scattering amplitude over such node is calculated it will be proportional to the crystal volume.

$$\int D(\mathbf{S})dv_{\mathbf{S}} = A_1\cdot A_2\cdot A_3 = V \tag{II.40}$$

II.7 Coherence length. Position correlation between crystals.

If the coherence length of the incoming X-ray beam covers more then one single crystallite the effects of position correlation of these crystallites have to be taken into account when scattering amplitude is calculated. The spatial or lateral coherence length L_{s0} is determined by geometrical considerations:

$$L_{s0} = \frac{\lambda R}{2r_s} \tag{II.41}$$

where R is the source-sample distance and r_s is the source size. L_{s0} represents the maximum spacing between two points of an extended source emitting photons which can interfere at any given sample point. For scattering processes, the projection of the coherence length onto the sample surface is important, so that:

$$L_s = \frac{L_{s0}}{\sin(\alpha_i)} \tag{II.42}$$

where α_i is the angle of incidence.

In the case of grazing incidence L_s becomes very large. For instance, for set-up at grazing incidence angle of 0.2 °, L_s is in the order of 10^3 nm. For crystal (island) size in the order of 10^2 nm investigated in this work the effect of island short-range correlation should be considered. The effect of crystal position correlation on the scattering amplitude is accounted by the additional correlation factor R:

$$P(\mathbf{r}) = \sum_m P_m(\mathbf{r} - \mathbf{R_m}) \tag{II.43}$$

If an array of spatially separated equivalent crystals is considered, the correlation factor can be rewritten in the form:

$$P(\mathbf{r}) = P_c(\mathbf{r}) \sum_m \delta(\mathbf{r} - \mathbf{R_m}) \tag{II.44}$$

where $P_c(\mathbf{r})$ is the *position function*, representing the position of the center point of each crystal, and δ a delta function, describing the discrete behavior of correlation factor $P(\mathbf{r})$. Describing the correlation part of scattering amplitude in terms of Fourier integral (II.12) one obtains:

$$F(\mathbf{S}) = \int P_c(\mathbf{S}) \sum_m \delta(\mathbf{r} - \mathbf{R_m}) \cdot \exp(i\mathbf{S} \cdot \mathbf{r}) d^3r \tag{II.45}$$

Since $\mathbf{r}$ only takes discrete values $\mathbf{r} = R_m$ this integral can be split into a sum:

$$F(\mathbf{S}) \approx \sum_m \exp[i(\mathbf{S}^{\parallel} \cdot \mathbf{R}^{\parallel}_{\mathbf{m}} + \mathbf{S}^{\perp} \cdot \mathbf{R}^{\perp}_{\mathbf{m}})] \tag{II.46}$$

where the component $\mathbf{S}^{\parallel} \cdot \mathbf{R}^{\parallel}_{\mathbf{m}}$ accounts for lateral ordering of crystals within the layer and the $\mathbf{S}^{\perp} \cdot \mathbf{R}^{\perp}_{\mathbf{m}}$ component accounts for the correlation along surface normal. If the function describing the relative crystal positions R_m known, the scattering amplitude of a single crystal in the array of equal crystals is then modulated by a factor:

$$F(\mathbf{S}) \approx \sum_m \exp[i\, \mathbf{S} \cdot \mathbf{R_m}] \tag{II.47}$$

II.8 Crystal with distortions

As derived above, the scattering amplitude of a single atomic scatterer is given by Eq. (II.14). In the kinematic approximation (see below), the scattering amplitude of a sample consisting of a discrete number n of scattering points can be written as a sum of the scattering amplitude of each of the points.

$$F(\mathbf{S}) = \sum_n f_a(\mathbf{S}) \exp[2\pi i\, (\mathbf{S} \cdot \mathbf{r_n})] \tag{II.48}$$

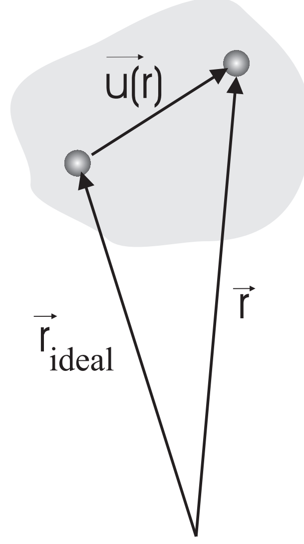

Figure 6: Atom in displacement field (shown in grey). Determination of displacement vector.

where f_a is the atomic scattering factor and $\mathbf{r_n}$ is the vector describing the position of the n-th atom. Considering the finite volume of the scattering body its scattering amplitude should be multiplied by the shape factor D, (see Eq. II.36). For an undistorted ideal crystal the diffraction vector $\mathbf{S}$ can possess only values with $\mathbf{S} = \mathbf{H_{hkl}}$. So, equation (II.36) can be written in the form:

$$D(\mathbf{H_{hkl}}) = \int_V F(\mathbf{r}) \exp[2\pi i \, (\mathbf{H_{hkl}} \cdot \mathbf{r})] \, dV_{\mathbf{r}} \tag{II.49}$$

If particular atoms of the crystal undergo displacements from their initial positions it influences the phase difference between the scattered waves and changes the value of the total scattering amplitude. To describe such atomic displacements the displacement vector $\mathbf{u}(\mathbf{r})$ is introduced (Fig. 6).

The number of vectors $\mathbf{u}(\mathbf{r})$ defines the so-called *displacement field* in which the ideal crystal undergoes deformation. In general, atomic displacements are assumed to be smaller then the absolute value of $\mathbf{r}$. In this case, the electron density of the ideal crystal lattice is assumed to follow the changes of atomic positions (*Takagi approximation* [43]). Under this condition the final position of each atom is described by:

$$\mathbf{r} = \mathbf{r_{ideal}} - \mathbf{u}(\mathbf{r}) \tag{II.50}$$

Now, the equation for the total scattering amplitude of the object should be written

as:

$$\begin{aligned}F_{abs} &\approx F(\mathbf{S})\cdot D(\mathbf{H_{hkl}}) = \\ &= \sum_n f_a(\mathbf{S})\int_V F(\mathbf{r})\exp[2\pi i\,(\mathbf{H_{hkl}}\cdot\mathbf{r})]\cdot \\ &\quad\cdot\exp[2\pi i\,(\mathbf{S}\cdot(\mathbf{r_n}-\mathbf{u}(\mathbf{r_n}))]\,dV_{\mathbf{r}}\end{aligned} \tag{II.51}$$

or:

$$F_{abs}\approx\sum_n f_a(\mathbf{S})\int_V F(\mathbf{r})\ \exp[-2\pi i\,(\mathbf{q}\cdot\mathbf{r_n})]\ \exp[-2\pi i\,(\mathbf{S}\cdot\mathbf{u}(\mathbf{r_n}))]\,dV_{\mathbf{r}} \tag{II.52}$$

where vector $\mathbf{q}=\mathbf{H_{hkl}}-\mathbf{S}$ represents the deviation of the F_{abs} position of the deformed crystal relative to its position in the case of scattering by an "ideal" crystal. If the position of atomic scatterers are limited by the crystal dimensions Eq.(II.52) should be rewritten as:

$$F_{abs}\approx\sum_n f_a(\mathbf{S})\int_F \exp[-2\pi i\,(\mathbf{q}\cdot\mathbf{r_n})]\ \exp[-2\pi i\,(\mathbf{S}\cdot\mathbf{u}(\mathbf{r_n}))]\,dV_{\mathbf{r}} \tag{II.53}$$

To use the last equation for numerical calculations one should mathematically introduce the shape function of the crystal and to determine the matrix elements of displacement field.

II.9 Phase problem.

In the intensity signal collected during X-ray diffraction experiment the phase information - information about the atomic positions - is lost. In the case of crystals with distortions the main method for extracting information about the positions of the atoms is based on the comparison of the experimentally derived intensity distribution with that calculated numerically for a model. The main disadvantage of this technique is the large amount of time needed for the numerical calculations.

As a highlight, recently the new method exploiting the gradient search iterative algorithms has been announced for the direct retrieval of the phase information from the intensity signal [44]. This method is at the moment on its development stage and possibly will replace the conventional technique in the near future [45].

II.10 Kinematic approximation and critical thickness

When calculating the total amplitude of the scattered wave it has been assumed that the total wave is the sum of the elementary waves. This approach is called *kinematic* approximation and ignores the following circumstances:

(I) When an incident wave is propagating in a crystal, its amplitude must diminish gradually, because energy is lost due to the excitation of secondary scattered waves. The initial wave is weakened by the effect of absorption.

(II) Secondary diffracted waves interfere both with the initial wave and among themselves and also experience scattering and absorption.

Those effects are taken into account in the more general *dynamical* theory [46],[47]. Since dynamic effects develop gradually as the initial wave penetrates into the crystal, the kinematic approach yields fairly accurate results for sufficiently small penetration thickness. For small thicknesses the primary wave is hardly weakened, the secondary waves has not yet gained much intensity, and absorption effects can be neglected. In other words, the kinematic approximation can be used when the absolute intensity of the scattered beam is weak compared with that of the incident beam.

Assume the single crystal is in the particular position relative to the incoming beam so that the intensity at particular reciprocal point (h,k,l) can be measured. In this case, the amplitude of the scattered beam F_{cr} is given by Eq. II.38. The scattering power of a single electron unit F_e is given by (II.8). Assuming the scattering crystal to have a cubic shape with sides of length A and the total scattering intensity to be measured by the flat rectangular detector with detection area of $\Delta X \Delta Y$ (determines the integration area in the reciprocal space of the point detector moving in the laboratory system with coordinates x and y). For rectangular crystal its projection on the detector is approximately $\Delta X \cdot \Delta Y \approx A^2$. In the case, where the center of the reciprocal lattice point hkl intersects the Ewald sphere, the shape factor D in (II.38) is also proportional to A^2. In this case the intensity of the diffracted beam relative to the incoming beam can be written as [48]:

$$\frac{I_{hkl}}{I_0 A^2} = F_e^2 (\frac{F_{hkl}}{\gamma})^2 \, \lambda^2 \, A^2 \tag{II.54}$$

where prefactor A^2 for the initial intensity describes the fact, that crystal shades the incoming beam by its area A^2 (all other factors have been explained previousely). This expression shows that the integrated scattered intensity is proportional to the square of the linear crystal dimension (or crystal thickness) A. Obviously, this can be true only until this thickness will not exceed some value after which the scattering intensity will become equal to the incoming beam intensity, so that:

$$F_e \frac{F_{hkl}}{\gamma} \lambda \, A^K \leq 1 \tag{II.55}$$

where A^K is the *critical thickness* determining the range of validity of the kinematical approximation. Assuming all atoms to scatter in phase, so that $F_e F_{hkl} = \sum F_e$ ($F_e \approx 10^{-11}$ cm) and taking the volume of each atom to be $\approx 10^{-23} cm^3$, then for X-ray radiation with $\lambda \approx 10^{-8}$ cm A^K will be in the order of $A^K \approx 1$ μm.

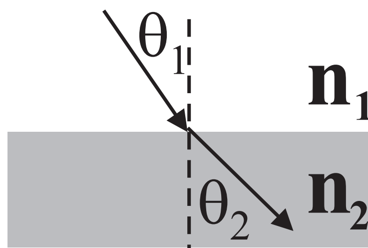

Figure 7: Schematic representation of refraction of the light on the border between two media with different refractive indices (n_1 and n_2)

The structures studied in this thesis, have linear dimensions far below 10^{-5} cm. In this case, the kinematic approximation is adequate for numerical calculations of the scattered intensities.

II.11 Grazing incidence diffraction.

II.11.1 Total reflection effect. Penetration depth.

Snell's law (Fig. 7) gives the relationship between angles of incidence and refraction for a wave impinging on an interface between two media with different indices of refraction. The law follows from the boundary condition that a wave be continuous across a boundary, which requires that the phase of the wave be constant on any given plane, resulting in:

$$n_1 \sin(\theta_1) = n_2 \sin(\theta_2) \tag{II.56}$$

where θ_1 and θ_2 are the angles from the normal of the incident and refracted waves, and n_1 and n_2 are refractive indices of the media.

Analysing Snell's law one can find certain circumstances under which the ray will not be refracted, instead it is reflected. This is the case when $n_1/n_2 > 1$. In this case the angle of incidence exceeds the *critical angle*:

$$\sin(\theta_{cr}) = \frac{n_2}{n_1} \tag{II.57}$$

The last equation determines the *grazing incidence* regime. The average *index of refraction* (n) is the fundamental quantity which controls the "optical effects" in the grazing incidence regime. In the case of an X-ray beam coming from vacuum(air) ($n_1 = 1$) into a solid the index of refraction can be written as:

$$n = 1 - \delta + i\beta \tag{II.58}$$

Material	δ(10keV)	α_{cr}, $^\circ$
AlAs	6.92 E-06	0.213
GaAs	1 E-05	0.256
InAs	1.08 E-05	0.266

Table II.3: Dispersion coefficients and critical angle values of some III-V compound semiconductors.

where δ and β represent respectively *dispersion* and *absorption* of the medium. For X-ray energies far away from absorption edges of the medium, β is at least one order of magnitude smaller than δ - the absorption effects can be neglected:

$$\delta \approx r_0 \frac{\lambda^2}{2\pi} \rho_e \tag{II.59}$$

where r_0 is the Bohr atomic radius and ρ_e is the electron density. To satisfy the grazing incidence conditions of the Snells law (introduction of angle α = 90 - θ_1):

$$1 - \delta = \cos(\alpha_{cr}) \tag{II.60}$$

Taking into account that in the case of X-rays grazing incidence the incoming beam angles α_i have values far below one degree one can approximate:

$$\cos(\alpha_{cr}) \approx 1 - \frac{\alpha_{cr}^2}{2} \tag{II.61}$$

and so:

$$\alpha_{cr} \approx \sqrt{2\delta} = \lambda \sqrt{\rho_e r_0 / \pi} \tag{II.62}$$

The values of δ and critical angle, α_{cr}, at incoming radiation energy of 10 keV for the materials discussed in this work are shown in Table II.3.

While on the border between both media in the regime of total external reflection the primary beam is specularly reflected, inside the less dense medium (with dispersion/absorption) an *evanescent wave* propagates [51], and E-field decays exponentially within the penetration depth [4]. In the absence of absorption the penetration depth is:

$$\Lambda \approx \lambda / [2\pi(2\delta - \sin(\alpha_i)^2)^{1/2}] \tag{II.63}$$

For incident angles of the order of 0.2° the penetration depth is in the nanometers rage. For the GaAs and AlAs substrate materials the dependence of the penetration depth on the incident angle is shown in Fig. 8.

It can be seen, that by varying the incoming angle within the range of total reflection one can significantly influence the penetration depth of the X-rays.

[4] The depth at which the intensity of the incident wave is reduced by a factor $\frac{1}{e}$

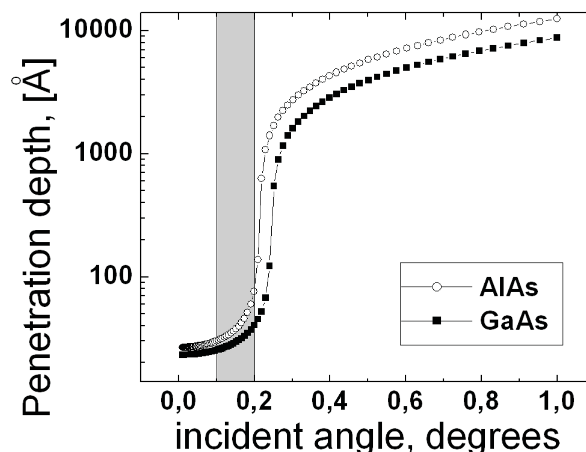

Figure 8: Angular dependence of penetration depth for GaAs and AlAs crystals at incoming X-ray radiation energy of 10 keV. Area marked grey represents the region exploited in this work.

II.11.2 Reflection/refraction effects. Distorted wave approximation.

In the general case of grazing incidence diffraction on a flat crystal surface the intensities of the refracted and reflected X-ray waves and the phase relation between them and the incident wave field should be corrected by the Fresnel coefficients of *transmission* (T) and *reflection* (R), written in the form:

$$R(\alpha) = \frac{E_1}{E_0} = \sin(\alpha) - \frac{\sqrt{n_0^2 - \cos(\alpha)^2}}{\sin(\alpha) + \sqrt{n_0^2 - \cos(\alpha)^2}} \tag{II.64}$$

and

$$T(\alpha) = \frac{E_t}{E_0} = \frac{2\sin(\alpha)}{\sin(\alpha) + \sqrt{n_0^2 - \cos(\alpha)^2}} \tag{II.65}$$

The reflectivity coefficient R^2 determines the specularly reflected intensity, whereas the transmittivity, T^2, governs the intensity of the evanescent wave field.

Now the case of a crystal with finite dimensions positioned on/under the surface of an other laterally flat and infinitely large crystal (substrate) made of different material should be considered. The incident X-ray wave incoming at angle below the substrate critical angle interacts with the small crystal positioned on the substrate (case 1) or below the substrate surface (case 2) at some depth t.

In the first case, because of the small incident angles (smaller then α_c), there is a fraction of the incoming X-rays that is specularly reflected from the substrate

surface before entering the probed crystal. In this situation the vector of the incoming wave is modified. It leads to the appearance of additional amplitude in the overall scattering/diffraction process. The same effects take place for the outcoming waves. In the second case, refraction effects lead to changes of the incoming and outgoing wave vector directions inside the substrate material.

Under these circumstances the kinematical approximation does not describe the scattering process sufficiently well and the so-called *distorted wave Born approximation* (DWBA) should be used [52]. The incoming plain wave produces a wave field inside and outside of the crystal under investigation. The crystal itself is treated as a wave "perturbation" described by the perturbation potential [53]. After interaction with this potential the modified scattered wave leaves the sample. The solution of the problem consist of two independent components: the dynamical component describing the scattering by the undisturbed medium (substrate) and the kinematical diffuse component for the scattering by the crystal on the substrate. The calculation of the kinematical scattered component involves incident, specularly reflected and diffracted waves (case 1) or refracted and diffracted waves (case 2), as shown in Fig. 9. The main processes, determining the scattering by the object on the substrate are:

- scattering/diffraction of the primary incoming wave (kinematic case)
- scattering/diffraction and reflection of the primary incoming wave
- scattering/diffraction of the modified (reflected) incoming wave
- scattering/diffraction and reflection of the modified (reflected) incoming wave

The total scattering amplitude is then the sum of four components:

$$A_1(\mathbf{q_1}) \approx \sum_n f_a(\mathbf{q_1}) \int_F \exp[i\,(\mathbf{q}^{\parallel} + \mathbf{q_1}^{\perp}) \cdot \mathbf{r_n}]\,dV \tag{II.66}$$

$$A_2(\mathbf{q_2}) \approx R(\alpha_f) \sum_n f_a(\mathbf{q_2}) \int_F \exp[i\,(\mathbf{q}^{\parallel} + \mathbf{q_2}^{\perp}) \cdot \mathbf{r_n}]\,dV \tag{II.67}$$

$$A_3(\mathbf{q_3}) \approx R(\alpha_i) \sum_n f_a(\mathbf{q_3}) \int_F \exp[i\,(\mathbf{q}^{\parallel} + \mathbf{q_3}^{\perp}) \cdot \mathbf{r_n}]\,dV \tag{II.68}$$

$$A_4(\mathbf{q_4}) \approx R(\alpha_i)\,R(\alpha_f) \sum_n f_a(\mathbf{q_4}) \int_F \exp[i\,(\mathbf{q}^{\parallel} + \mathbf{q_4}^{\perp}) \cdot \mathbf{r_n}]\,dV \tag{II.69}$$

The main process determining the scattering by the object buried under the substrate is diffraction and refraction of the modified (refracted) incoming wave and the scattering in this case is described by the amplitude:

$$A_5(\mathbf{q_5}) \approx T(\alpha_i)\,T(\alpha_f) \sum_n f_a(\mathbf{q_5}) \int_F \exp[i\,(\mathbf{q}^{\parallel} + \mathbf{q_5}^{\perp}) \cdot \mathbf{r_n}]\,dV \tag{II.70}$$

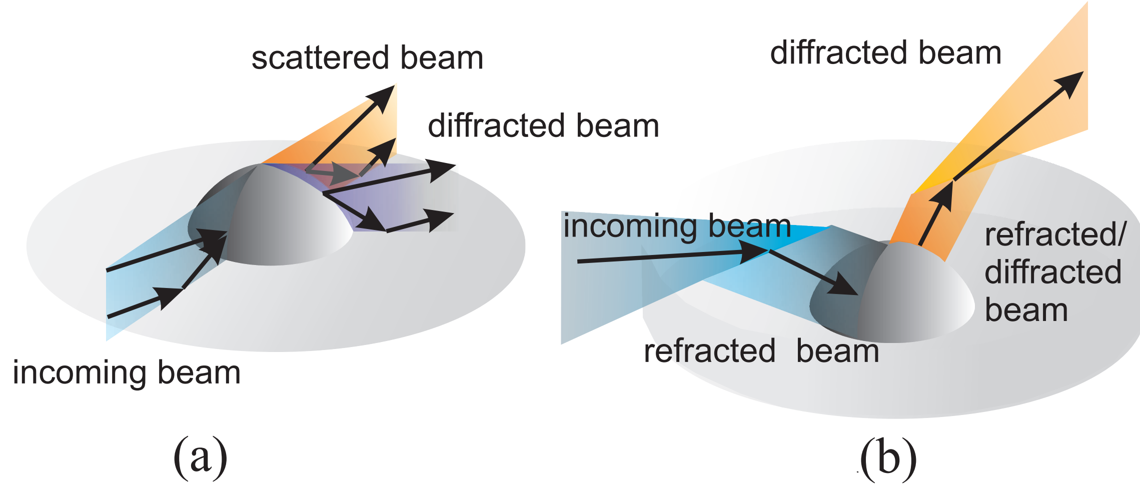

Figure 9: Schematic representation of scattering by an object on the substrate surface (a), and by an object buried under the substrate surface (b) under grazing incidence.

In each particular case the diffuse intensity depends strongly on the transmission or reflection Fresnel coefficients T and R which themselves are functions of the incoming and outgoing angles α_i and α_f. The vertical components of the diffraction vectors $\mathbf{q_d}$ with d = 1-5 are different for all five waves and are determined by their corresponding vertical components of incoming $\mathbf{k^{IN}}$ and outgoing $\mathbf{k^{OUT}}$ wave vectors given as [112]:

$$\mathbf{q_1} = -\mathbf{k^{OUT}} - \mathbf{k^{IN}} \quad \text{(II.71)}$$

$$\mathbf{q_2} = \mathbf{k^{OUT}} - \mathbf{k^{IN}} \quad \text{(II.72)}$$

$$\mathbf{q_3} = -\mathbf{k^{OUT}} + \mathbf{k^{IN}} \quad \text{(II.73)}$$

$$\mathbf{q_4} = \mathbf{k^{OUT}} + \mathbf{k^{IN}} \quad \text{(II.74)}$$

$$\mathbf{q_5} = -\mathbf{K^{OUT}} - \mathbf{K^{IN}} \quad \text{(II.75)}$$

where $\mathbf{K}$ denotes the wave vector in the substrate material. In the first case the angular dependence of the coefficients determines the influence of the reflected wave amplitudes on the total intensity pattern. For the angles below the critical angle of the substrate, α_c, the influence of these amplitudes is the largest, but for angles above α_c the effect diminishes rapidly until only the kinematical amplitude A_1 is significant.

Experimentally the waves scattered or diffracted in the grazing incidence regime from the non-buried island can be detected only separately. The conditions when only diffracted component is analysed define the *grazing incidence diffraction* (GID) case. If the scattered component is investigated the *grazing incidence X-ray scattering* (GIXS) geometry is used. If the scattered signal is investigated in the vicinity of the primary X-ray beam spot, the special regime - *grazing incidence small angle scattering* (GISAXS)- is defined. In detailed form these techniques will be described in IV.3.

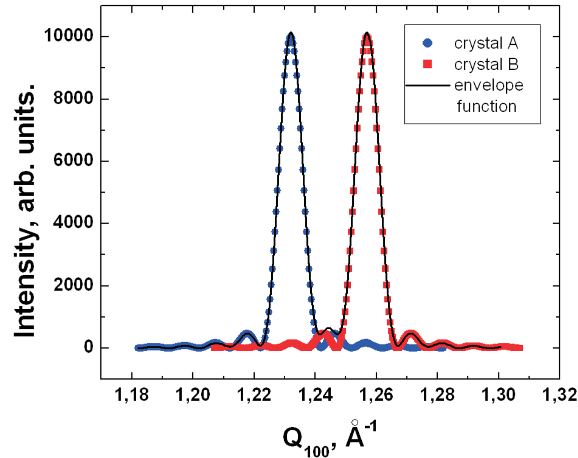

Figure 10: Intensity distribution in [100] direction of reciprocal space modulated by overlapping of Fourier transformed shape functions stemming from two circle-shaped single-crystals (size 10 nm) having corresponding lattice constants of 0.5 nm and 0.51 nm. The envelope intensity profile is given by addition of intensity profiles from single-crystals.

II.11.3 Strained island in GID. Iso-strain approximation.

As shown previously, the scattering amplitude of a crystal with final dimensions is described by the Fourier transform of the crystal shape function and the atomic positions within the crystal volume (see Eq. II.29). If two crystallites having slightly different lattice constants, simultaneously scatter an incoming X-ray wave, the resulting intensity profile can be interpreted as the overlap of squared Fourier transforms of the corresponding crystal shape functions. As an example, the linear intensity distribution along the [100] direction for disc-shaped crystals having diameter of 10nm and lattice constants 0.5 nm and 0.51 nm, is shown in Fig. 10 .

The resulting envelope intensity function in Fig. 10 represents the sum of two single intensity distributions from crystallites. Using this approximation, the crystal with a continuous strain profile can also be roughly subdivided to a number of single sub-crystals, the "iso-strain areas" (ISA) [57] so that the final intensity distribution is the sum of the intensity profiles from all ISAs.

In the in-plane case of GID where only lateral lattice constants of the crystal are probed (the vertical lattice constant is related to the z-direction in real space) the ISA model is assumed to be applicable to crystals with strain field gradient parallel to the crystal z-axis. The structure can be then treated as a vertical stacking of sub-crystals (ISAs) with shape functions primarily defined by ISA lateral dimensions.

For a vertical arrangement of iso-strain areas the vertical position above the sub-

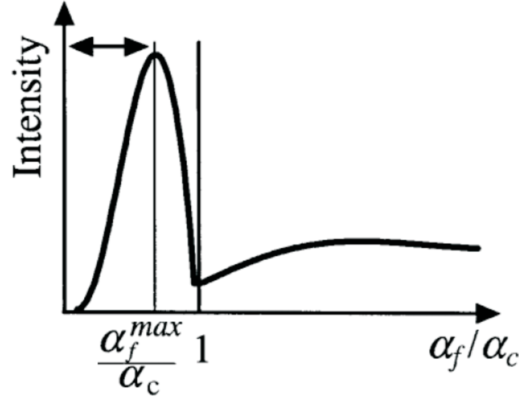

Figure 11: General form of the intensity distribution for scattering by a single ISA under grazing incidence conditions.

strate surface is also important. If one assumes the ISAs are sufficiently thin, so that their vertical positions can be described by average height, z_{ISA} , the total scattering amplitude in the particular point of reciprocal space with a defined value of lateral diffraction vector component $\mathbf{q}^{\|}$ - ISA with a particular lateral lattice constant - described in DWBA, Eq.(II.66), can be rewritten as [58]:

$$F(\alpha_i, \alpha_f) = F_0\,|\mathbf{k}|(\alpha_i + \alpha_f)\,\exp(i\mathbf{q_z}z)\,t(\alpha_i, z)t(\alpha_f, z) \tag{II.76}$$

where t(α) = 1 + r(α) exp(-i k $\alpha_{i,f}$ z) is a *modified transmission coefficient.* In the case of a fixed incoming angle α_i, the scattered intensity profile is mainly determined by the $t(\alpha_f, z)$ component:

$$I(\alpha_f, z) \approx |t(\alpha_f, z)|^2 \tag{II.77}$$

In the GID regime with $\alpha_i \leq \alpha_c$, this function possess a general form shown in Fig. 11 (Plot taken from [59]).

The main feature of this function is the pronounced maximum at α_{max}. Information about the height z_{ISA} of a particular iso-strain area over the substrate surface can be derived from α_{max}:

$$z_{ISA} = \frac{1}{|\mathbf{k}|\alpha_{max}}\arccos(\frac{\alpha_{max}}{\alpha_c}) \tag{II.78}$$

Depending on the relative vertical position of the ISA to the substrate surface this maximum will shift from values with $\frac{\alpha_{max}}{\alpha_c} < 1$ for $z_{ISA} > z_{substrate}$ up to $\frac{\alpha_{max}}{\alpha_c} \Rightarrow 1$ for $z_{ISA} \approx z_{substrate}$.

II.12 X-ray reflectivity of thin films

X-ray reflectivity (XRR) is a powerful tool for investigating multilayered thin film structures. XRR is highly sensitive to electron density gradients irrespective of the crystalline nature of the system [60]. The main advantage of this technique is that it allows the density and the thickness of thin layers to be determined.

The main goal of analysis of the XRR profile is the determination of the refractive indices of all layers in the structure. The reflectivity for a system with n thin layers can be calculated using Parratt's recursive method. For an arbitrary layer j that is bound by interfaces *j - 1* and j, the total reflectivities at the two interfaces, r_{j-1}^F and r_j^F are related to F_{j-1} by [61]:

$$r_{j-1}^F = \frac{F_{j-1} + r_j^F \exp(-iq_j t_j)}{1 + F_{j-1} \cdot r_j^F \exp(-iq_j t_j)} \tag{II.79}$$

where r_j^F is the *total* reflection coefficient at interface j, defined as the ratio of outgoing to incoming electric wave amplitudes, and F_{j-1} is related to q_j by:

$$F_{j-1} = \frac{q_{j-1} - q_j}{q_{j-1} + q_j} \tag{II.80}$$

with q_j=$4\pi f_i/\lambda$, and $f_i = \sqrt{\alpha_j^2 - 2\delta - 2i\beta}$. α_j is the incident angle in respect to the interface j.

The boundary condition for Eq. II.79 is found at film/substrate interface n where r_n^F=F_n due to the fact that substrate is semi-infinite [62]. Starting from the downmost interface with j=n, each r_{j-1}^F coefficient up to the r_0^F for the uppermost interface can be recursively determined using Eq. II.79.

Since most interfaces are not ideal on the length scale probed by the hard X-rays the nonideality of the interface has to be taken into account in the reflectivity calculations. For a non-ideal interface, the average electron density profile along the specimen normal is assumed to be modelled by an "*error function*" (the Névot-Croce roughness [63]):

$$r_j^{N-\sigma} = r_j^N \exp(-2\sigma_j^2 k_0^2 f_j f_{j+1}) \tag{II.81}$$

where $k_0 = 2\pi/\lambda$ - is the wavevector. The modified reflection coefficient $r_j^{N-\sigma}$ is then used for further calculations.

Chapter III

Elastic deformation of SK-islands

III.1 General elasticity theory

The general theory of elasticity is quite complicated even for simple homogeneous media [64]. Only the simplest linear elastic deformation process used for interpreting the data in this thesis will be briefly summarized in this chapter.

The main goal of elasticity theory is to define the displacement field **u**(x,y,z). **u** is a vector that defines the displacement at any point *P'* in a strained body from its original (unstrained) position *P*. The displacement vector **u**(x, y, z) is then given by:

$$\mathbf{u}(x,y,z) = u_x(x,y,z), u_y(x,y,z), u_z(x,y,z) \tag{III.1}$$

where components u_x, u_y, and u_z represent projections of **u** on the x, y, z axes of a orthogonal coordinate system. Usually one is only interested in the determination of local deformations, i.e. the deformation that acts on a volume element dV after it has been displaced some amount. The local strain ϵ, is defined by nine components of the strain tensor ϵ_{ij} acting on an elementary volume element dV.

The relation between the displacement field **u**(r) and the local strain tensor ϵ_{ij} can be derived by considering a uniform elongation in one direction. In this case the vector **u** only has a component in x-direction, so $|u(r)| = |u_x| = a \cdot x$, where a is some constant. The relative elongation of the length element l_0 is given by l, defining the displacement of each point with initial coordinate x_0 to the point $x_0 + dx$. For this deformation the elementary formula for strain can be written as:

$$\epsilon_{xx} = \epsilon_x = \frac{(l - l_0)}{l_0} = \frac{(u_x(x+dx) - u_x(x))}{dx} = \frac{du_x}{dx} \tag{III.2}$$

If the deformation takes place in all three main directions, the corresponding expressions for ϵ_{yy} and ϵ_{zz} should be defined. The deformations in main directions given by components ϵ_{xx}, ϵ_{yy}, and ϵ_{zz} describe the *normal strains* due to forces acting along

the normals to the surfaces of a unit cubic volume element dV. The deformations in the orthogonal directions are described by *shear strains*:

$$\epsilon_{ij} = \epsilon_{ji} = \frac{1}{2}(\frac{du_i}{dx_j} + \frac{du_j}{dx_i}) = \frac{1}{2}\gamma_{ij} \qquad \text{(III.3)}$$

giving:

$$\epsilon_{\mathbf{ij}} = \begin{pmatrix} \epsilon_x & \epsilon_{xy} & \epsilon_{xz} \\ \epsilon_{xy} & \epsilon_y & \epsilon_{yz} \\ \epsilon_{xz} & \epsilon_{yz} & \epsilon_z \end{pmatrix} = \begin{pmatrix} \epsilon_x & \gamma_{xy}/2 & \gamma_{xz}/2 \\ \gamma_{xy}/2 & \epsilon_y & \gamma_{yz}/2 \\ \gamma_{xz}/2 & \gamma_{yz}/2 & \epsilon_z \end{pmatrix} \qquad \text{(III.4)}$$

In the case of small deformations (ϵ <0.01) the generalized approximation called *Hookes law*, mechanical stress is directly proportional to strain. The relation between stress σ_{kl} and deformation ϵ_{mn} tensors, is given by:

$$\sigma_{kl} = C_{klmn}\epsilon_{mn} \qquad \text{(III.5)}$$

and vice versa:

$$\epsilon_{kl} = S_{klmn}\sigma_{mn} \qquad \text{(III.6)}$$

where C_{klmn} and $S_{klmn} = (C_{klmn})^{-1}$ are respectively the *elasticity tensor* and its *compliance stiffness tensor*. In the general case the elasticity tensor has 81 components. For materials with cubic symmetry there are three coefficients: $C_{11} = C_{1111} = C_{2222} = C_{3333}$, $C_{12} = C_{1122} = C_{2233}$, etc., and $C_{44} = C_{1212} = C_{2323}$ etc. In isotropic materials two independent elastic coefficients are sufficient, the *Young modulus E* and the *Poissons ratio* ν:

$$E = (C_{11} - C_{12})(C_{11} + 2C_{12})/(C_{11} + C - 12) \qquad \text{(III.7)}$$

$$\nu = C_{12}/(C_{11} + C_{12}) \qquad \text{(III.8)}$$

The main mechanical constants at RT for the materials used in this thesis are given in Table III.1[1]. For shear stresses the shear modulus $G = E/(2(1+\nu))$ is useful. In

Material	C_{11}, GPa	C_{12}, GPa	C_{44}, GPa	E, GPa	ν, GPa
InAs	83.4	45.4	39.5	51.4	0.35
GaAs	118.8	53.8	59.4	85.3	0.31
AlAs	120.2	57	58.9	83.5	0.41

Table III.1: Mechanical constants of InAs, GaAs and AlAs crystals at RT.

[1]taken from www.ioffe.rssi.ru/SVA/NSM/Semicond/

this case Hookes law for each separated strain component can be written as:

$$\begin{aligned} \epsilon_x &= \frac{1}{E}(\sigma_x - \nu(\sigma_y + \sigma_z)) \quad \gamma_{xy} = \frac{\tau_{xy}}{G} \\ \epsilon_y &= \frac{1}{E}(\sigma_y - \nu(\sigma_z + \sigma_x)) \quad \gamma_{yz} = \frac{\tau_{yz}}{G} \\ \epsilon_z &= \frac{1}{E}(\sigma_z - \nu(\sigma_x + \sigma_y)) \quad \gamma_{zx} = \frac{\tau_{zx}}{G} \end{aligned} \tag{III.9}$$

With stress tensor defined as:

$$\sigma_{\mathbf{ij}} = \begin{pmatrix} \sigma_x & \tau_{xy} & \tau_{xz} \\ \tau_{xy} & \sigma_y & \tau_{yz} \\ \tau_{xz} & \tau_{yz} & \sigma_z \end{pmatrix} \tag{III.10}$$

The above relations are used in the main algorithm for the linear solution of mechanical problem in the applied finite element program (see below).

III.1.1 Mechanical model of pseudomorphic growth

The growth of the film is called *pseudomorphic* if the overgrowing crystalline material inherits the lateral lattice constant of the underlying substrate. In materials with cubic crystal symmetry it will lead to an *orthogonal* deformation in the direction along the substrate surface normal.

The pseudomorphic deformation can be found in terms of the model describing the *biaxial normal deformation* (see fig. 1), where only equal normal stresses act perpendicularly to the x and y-oriented sides of the cube with volume V_0, and no stress in z-direction exists. In this case only the relations for normal components of elastic deformation need be considered:

$$\epsilon_x = \epsilon_y = \epsilon = \frac{1}{E}(\sigma - \nu\sigma), \epsilon_z = \frac{1}{E}(-2\nu\sigma) \tag{III.11}$$

where $\sigma = \sigma_{xx} = \sigma_{yy}$ ($\sigma_{zz} = 0$). Now replacing σ by ϵ_z the relation between the lateral and vertical deformation can be written as:

$$\epsilon_z = -\frac{2\nu}{1-\nu} \cdot \epsilon \tag{III.12}$$

The relative volume change after material is pseudomorphically strained can be approximated by:

$$\Delta V = V - V_0 \approx (\epsilon_x + \epsilon_y + \epsilon_z) \cdot V_0 \tag{III.13}$$

where V_0 and V are respectively the initial material volume before and the final volume after deformation. Using equations for ϵ this relation can be rewritten:

$$\frac{\Delta V}{V_0} = 2\epsilon\frac{1-2\nu}{1-\nu} \tag{III.14}$$

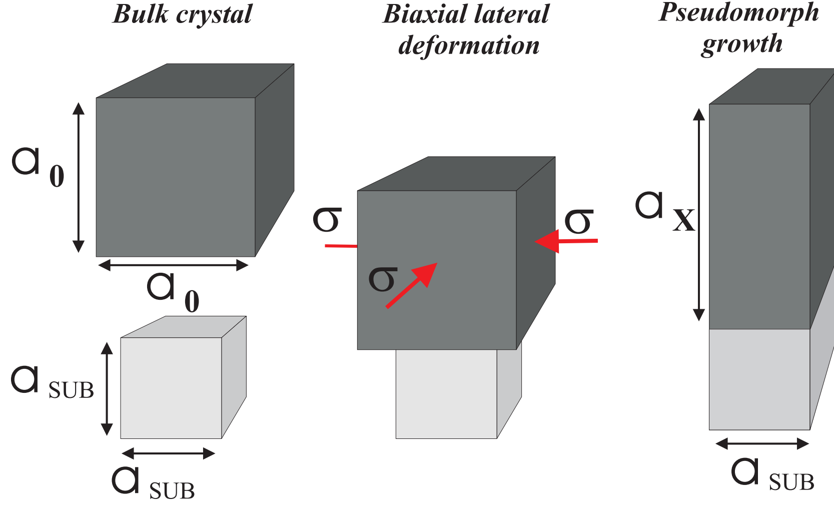

Figure 1: The mechanical modelling of pseudomorphic growth. (left) separated bulk crystals of film and substrate. (middle) the biaxial lateral deformation acting on the film. (right) elastically strained film pseudomorphically grown on the substrate.

Now, if initial volume of the material together with its mechanical properties are known then for a particular lateral deformation one can estimate the changes of material dimension in z-direction (dimensional changes in x-y directions are determined by the deformation).

III.1.2 Boundary conditions for the search of the diffracted signal from elastically strained islands.

To describe the atomic displacements within the unit cell of a cubic crystal the biaxial lateral deformation model should be rewritten in terms of crystal lattice constants. The lattice constant of the undeformed bulk crystal is a_0 and the lateral lattice constant of the pseudomorphically strained crystal is equal to that of the substrate material a_{sub}. The lateral deformation in this case is given by:

$$\epsilon = (\frac{a_{sub} - a_0}{a_0}) \tag{III.15}$$

Now eq. III.14 can be rewritten in the form:

$$\frac{a_X a_{sub}^2 - a_0^3}{a_0^3} = 2(\frac{a_{sub} - a_0}{a_0})(\frac{1-2\nu}{1-\nu}) \tag{III.16}$$

where a_X is the vertical lattice constant changed due to the orthogonal deformation of the cubic lattice. For known a_{sub}, a_0 and ν the a_x value can be calculated.

The lattice constants of the material determine the positions of corresponding reflections in reciprocal space. The three main components of reciprocal vector are related to the crystal lattice constants by:

$$q_x = \frac{2\pi}{a_x}, \quad q_y = \frac{2\pi}{a_y}, \quad q_z = \frac{2\pi}{a_z} \tag{III.17}$$

Let us assume the bulk lattice constant of the substrate material to be smaller than the bulk constant of the overlayer, $a_{sub} < a_0$, and both materials to have the same crystal structure and crystallographic orientation. In this case the relative positions of Bragg reflections will differ in reciprocal space by values:

$$\Delta q_x = \Delta q_y = \Delta q_z = \frac{2\pi}{a_{sub}} - \frac{2\pi}{a_0} \tag{III.18}$$

If growing material undergoes pseudomorphic deformation and inherits the lateral lattice constant of the substrate, the relative position of both Bragg reflections is then described by:

$$\Delta q_x = \Delta q_y = 0, \quad \Delta q_z = \frac{2\pi}{a_{sub}} - \frac{2\pi}{a_X} \tag{III.19}$$

where a_X should be calculated from Eq. III.12. In reciprocal space, the line connecting the positions of Bragg reflections for the pseudomorphically deformed material and the same material in its fully relaxed (bulk) state is the *relaxation line*. It describes the relaxation process of the strained material [65],[66].For out-of-plane reflections the relaxation line together with lines connecting the substrate bulk reflection with that of the film in its bulk and pseudomorphically strained states define the so-called *relaxation triangle* [67]. The relaxation triangle in the vicinity of the $(Q_x, 0, Q_z)$ reflection ($Q_y = const = 0$) for a film grown on a (001)-substrate is shown in Fig. 2(a). If 3D material undergoes elastic relaxation, the elastic strain field varies gradually from its maximum to its minimum value and the diffraction pattern is no longer described by a single Bragg reflection. It becomes diffuse and is mainly concentrated within the area defined by the relaxation triangle [68].

For mapping in the vicinity of in-plane reflections in GID-geometry ($Q_z \approx 0$) the region of interest in reciprocal space is restricted by the position of substrate Bragg peak and bulk reflection of the film building the relaxation line. Fig. 2(b) schematically shows the area for measurement along the radial (Q_x, $Q_y = Q_x$,0) direction.

III.2 Overview of methods for strain field computation in microscopic structures

Strain caused by lattice mismatch between the dots and the substrate/matrix materials is very important for both self-organisation mechanisms and for the opto-electronic

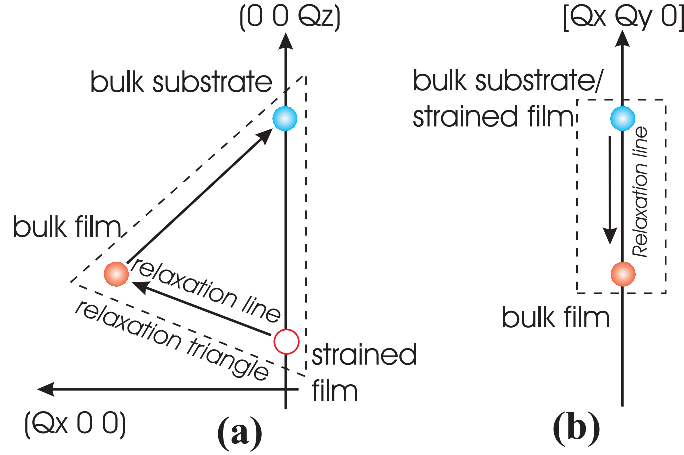

Figure 2: Areas of interest for reciprocal space mapping in the cases of out-of-plane (a) and in-plane (b) reflections for [001] oriented substrate and film (island) crystals with different bulk lattice parameters. Relaxation lines define the directions of elastic relaxation of the film (island) material.

properties of the QD system. Knowledge of the strain distribution in and around the dots as well as its impact on the electronic band structure are of great importance.

The mechanical strain distribution in solids can be treated in different ways depending on the complexity and size. The main approaches are based on *quantum-mechanics* or *atomistic elasticity* and numerical calculations using a *continuum mechanical* model.

In the atomistic elasticity (EM) model the strain energy is introduced in terms of few-body potentials $E = f(V_2(\mathbf{r}), V_3(q))$ between actual atoms, where $V_2(\mathbf{r})$ is a two-body term depending on the actual atomic position vector $\mathbf{r}$, and V_3(q) - a three-body term, a tensor dependent on the bond angle q. The functional form of these terms is taken to be strain-independent. The strain is determined by minimizing E with respect to atomic positions $\mathbf{r}$. Atomistic elasticity has been used to determine strain in quantum dots [69], with V_2 and V_3 taken from the valence force field model [70].

In case of atomistic quantum-mechanical approach (QMA) one does not have to assume any model for interatomic interactions. Instead the total electron and nuclear energy $E_{tot}(\mathbf{r})$ for each atomic configuration are computed using the Schrödinger equation. This approach has been applied for small (<100 atoms) atomic wires and clusters [71] but it is impractical for larger island structures with more than 10^4 atoms.

The finite element method (FEM) is based on linear elasticity theory. The thermo-elastic mechanical problem, related to the difference of lattice parameters between

island and substrate materials, is described by differential equations at particular points (nodes) and which are then solved to reveal the approximate deformation of the solid. This method was developed and applied to study the strain fields in different island systems, such as Si/Ge [72] or InGaAs/GaAs [74].

For small systems with a lattice mismatch far below 1% all three approaches yield similar results. but discrepancies arise for strains ≈1%. Calculations show noticeable differences [75]. Since the self-assembled growth of InAs/GaAs quantum dots deals with relatively large dimensions and lattice mismatches of up to 7%, the first two methods do not provide sufficient versatility and require long computation times. For that reason, the strain distribution in quantum dots of arbitrary shape or (and) elastic properties should be solved numerically using the finite element method [110]. A detailed description of the FEM method is given below.

III.3 Finite element analysis

III.3.1 Introdunction to FEM method

The finite element method (FEM) is a computer-based numerical technique that is used to solve different types of engineering problems, such as stress analysis, heat transfer, fluid flow, etc. FEM analysis is based on solving a system of equations that describes the chosen parameter - in this work displacement - in a continuous physical system. The main power of FEM lies in its ability to solve the problems numerically which can not be solved analytically [76].

The FEM analysis involves the partitioning of a continuous object into a finite number of *elements*. The materials properties and the governing relationships are applied over these elements and expressed mathematically in terms of unknown values at specific points in the elements called *nodes*. Each element has a simple geometrical shape, such as a triangle or quadrilateral. The standard element shape facilitates the development of the equations that relate the displacement behaviour within each element. This piecewise approximation of the physical continuum model on finite elements provides good precision even with simple approximating functions. By simply increasing the number of elements one can achieve higher precision.

To completely define a finite element model the nodal points, elements, loads, supports and element related data, i.e. material properties, must be defined. The program then formulates a set of simultaneous equations, which are the equilibrium equations corresponding to each *degree of freedom* (DOF) - directions in which movement can occur - at each nodal point. A *nodal point* can have up to six degrees of freedom - translation and rotation about the principal x, y, and z directions. When the FEM model is loaded it begins to deform - the force at each nodal point depends on the force at every other node - so that the whole system acts like a system of springs, deflecting until all forces balance. Since there are usually hundreds or thou-

sands of equilibrium equations generated in the typical finite element model, the use of a digital computer is mandatory.

In the stress analysis, used in this thesis, the equilibrium equations are solved for the *displacements* at each nodal point. In order to define a model that accurately represents the physical object, a sufficiently fine *mesh of elements* must be defined. In addition, the type of element and appropriate *boundary conditions* must be applied to represent the physical behavior of the model.

Because FEM models usually involve the preparation of a large number of nodal points and elements, the process of *data preparation* and *data analysis* has developed into a special field in finite element analysis. These steps are referred to as *pre-processing* and *post-processing* and involve a large amount of user interaction. In contrast, the analysis process (solving the differential equations) is done entirely by the computer.

The first step in preparing a finite element model involves defining the input data. In the case of the FEM model considered in this work, it consists of the following steps:

- definition of the nodal points (x, y, z coordinates) and elements
- definition of the element related material properties: modulus of elasticity, Poisson ratio, and thermal expansion coefficient
- specification of the boundary conditions, locations where the part is limited in motion or attached to an adjacent part
- Specification of the load (in present case - the load due to thermal expansion)

The actual analysis is usually done in a *batch environment*, since this phase does not require any user interaction. During this phase, the program performs the following steps:

- formulates equations that describe the stiffness of each element and then assembles the equations for all of the elements in a set of simultaneous equations that represent the total structure stiffness
- solves the system of equations for the displacements at each nodal point

The final phase is post-processing. The primary goal of this phase is to make sense of the large amount of data that is generated during the analysis. The process of data examination can be done by retrieving specific data arrays or by reviewing the graphical output. Contour plotted displacements at nodal points, nodal or elemental strains and deformed shapes can be displayed.

FEM has the following advantages:

- irregularly shaped parts can be analyzed

- can be applied to complex objects composed of several different materials with complex boundary conditions
- provides displacements throughout the entire model

III.3.2 Modeling of elastic strain in SK-island

For the calculation of the diffuse intensity pattern from a SK-island an exact knowledge of the displacement fields within the island are required. In the FEM method the elastic strain field in the island with lattice mismatch relative to the substrate is calculated using *thermo-elasticity* (TE) theory. This approach has been applied to simulate elastic deformations at coalescent island boundaries [77] in WV [78] and in SK islands [79]. In the TE model the elastic misfit strain ϵ_{el} is induced by a corresponding thermal strain ϵ_{th}:

$$\epsilon_{th} = \alpha \Delta T \tag{III.20}$$

where α is the thermal expansion coefficient of the material and ΔT is the relative temperature change. The elastic strain in SK-islands is amulated by assigning different hypothetical thermal expansion coefficients to the substrate and island:

$$\alpha_{sub} = 0, \quad \alpha_{isl} = \epsilon_{el}^{max} \tag{III.21}$$

with $\epsilon_{el}^{max} = (a_{sub} - a_{isl})/a_{isl}$ representing the real lattice mismatch between island and substrate crystals. In this case for a temperature increment $\Delta T = 1$ the maximum thermal strain at the island/substrate interface $\epsilon_{th} = \Delta\alpha = \alpha_{isl} - \alpha_{sub}$ will exactly correspond to ϵ_{el}^{max}. The deformation of the island/substrate system for particular boundary conditions initialized by the island thermal expansion is shown schematically in Fig. 3. The full relaxation of the heated island which is not rigidly connected to the substrate is shown in Fig. 3(b). If island is fixed (glued) on the substrate surface (Fig. 3(c)) it undergoes expansion to relax its thermal strain. The relaxation of this thermal strain due to island lateral deformation (Eq. III.20) will reach its maximum at the top of the island and will gradually fall to zero at the island/substrate interface where the lateral expansion is inhibited and the island elastic energy reaches its maximum. Island relaxation in the direction perpendicular to the substrate will be governed by the relation:

$$\epsilon_{th}^{\perp} = \alpha^{\perp} \Delta T \tag{III.22}$$

where $\alpha^{\perp} = \alpha(-2\nu/(1-\nu))$. For islands fully surrounded by the substrate matrix (Fig. 3(d)) the deformation field is more complicated, since in this case island expansion is limited in all directions.

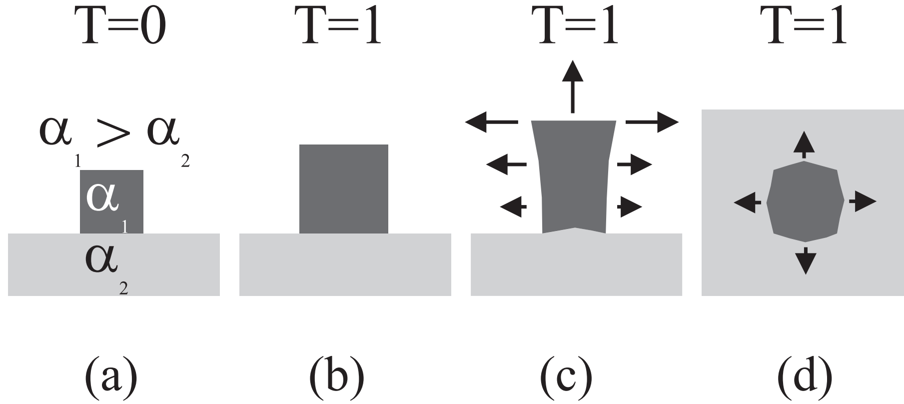

Figure 3: Schematic principle of the thermo-elastic approach for the simulation of strain fields in SK-islands. (a) initial condition T=0, thermal expansion coefficient of island is larger than that of the substrate; (b) island is not rigidly connected to the substrate. At T=1 island undergoes full elastic relaxation; (c) island is rigidly "glued" to substrate surface. At T=1 uppermost parts of island undergo maximal elastic relaxation. At the island/substrate interface, where the elastic strain energy reaches its maximum value, elastic deformation of the substrate is possible. (d) at T=1 complicated deformation of the island buried in the substrate matrix takes place.

III.3.3 Finite element modeling of SK-island

The optimization of the FEM model plays crucial role because it directly influences the computation time and precision of the final solution. In the frame of this thesis the SK-islands are assumed to be rotationally symmetric, with the shape of a rotational trapezoid. This assumption which ignores crystallographic anisotropy of the InAs/GaAs(001) system was found to be a sufficiently good approximation to describe the strain field in islands [80],[81]. The strain field in the substrate material should also be taken into account. Here the strain field in the island is of interest and so, the 2D rotationally symmetric body can be used as an approximation. The structure model used for the calculation of the displacement field in non-capped elastically strained SK-island by means of finite element method [2] is shown in Fig. 4. Because of rotational symmetry only half of the central 2D cross-section of the island/substrate system is used. The model island (light blue) is rigidly connected to the wetting layer of the same material and connected to the substrate material. The red line between island and wetting layer is a feature of the finite element program. It verifies that after meshing the closest nodes of island and wetting layer are connected to each other [3]. The necessity of application of this function is the inhomogeneous meshing

[2]FEM package ANSYS/Multi-physics was used

[3]command CPINTF. See ANSYS Commands Reference at www.cesup.ufrgs.br/ansys/

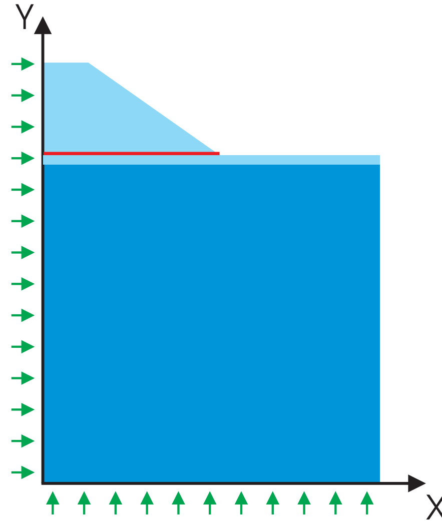

Figure 4: Finite element model of a SK-island on the substrate. The island is rigidly situated on the wetting layer, which is connected to the substrate. The motion of axial nodes is fixed in the directions shown by the arrows representing the system boundary conditions.

within the island region due to its complex shape forcing the standard element shape to be changed to fill the whole area within the island. The boundary conditions are represented by arrows pointing towards the directions in which the motion of nodes on principal axes (X and Y) is fixed. To mesh the model, the specific 2-D coupled-field solid element [4] defined by four nodes with up to four degrees of freedom per node was used with its axisymmetric property switched on.

III.3.4 Finite element solution for the SK-islands

The substrate material is taken to be AlAs. The lateral and vertical components of strain field in non-buried and buried islands calculated using FEM method are shown in Fig. 5 and Fig. 6. An axially symmetrical islands with constant chemical composition of InAs and island heights/island radius = 0.5 are used. The following features can be observed for both models:

- in both cases the islands tend to expand along the island/substrate interface(s) but are constrained by the substrate
- the non-buried island on the substrate reduces its extensional lateral mismatch strain gradually from its maximum value of $\epsilon^{\|} = (a_{AlAs} - a_{InAs})/a_{InAs} \approx$-0.067

[4]element PLANE13. Online ANSYS manual at http://www.cesup.ufrgs.br/ansys/realtoc.html

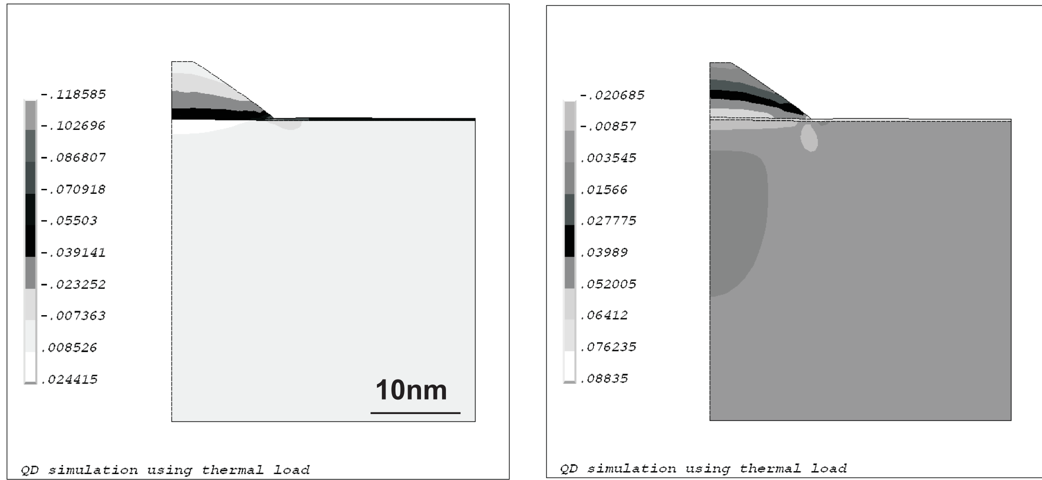

Figure 5: FEM solution for axially symmetric InAs island on the AlAs substrate. Left: lateral component of the strain field. Right: Vertical component of the strain field. The over-strain at island edge ($|\epsilon| > 0.067$) is caused by the stress singularity point at island edge.

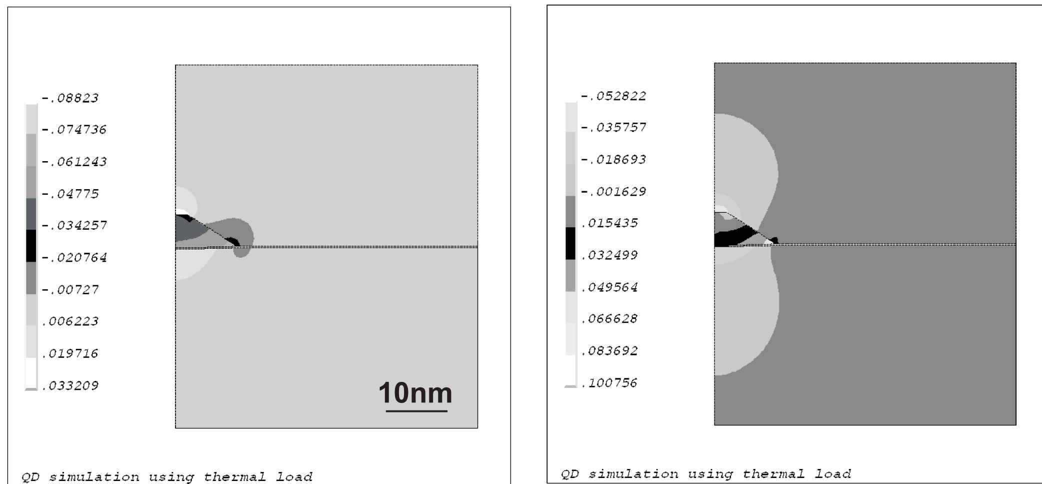

Figure 6: FEM solution for axially symmetric InAs island in the AlAs matrix. Left: lateral component of the strain field. Right: Vertical component of the strain field.

toward the island top by expansion. In the buried island the expansion is more complicated.

- the substrate also undergoes deformation in directions along the island/substrate interface(s), providing a strain field in the substrate of the opposite sign to the island strain. For non-buried islands this strain decays downwards and becomes insignificant at substrate depth of about two island heights. In the case of a buried island this substrate strain decays in the same manner both upwards and downwards from the island basement. In lateral direction substrate strain decreases much faster.

- when an island tries to expand, it compresses the substrate along the free surface adjacent to the island edges. This provides a driving force for the repulsion between the strain fields of neighboring islands. Experimentally island repulsion phenomena has been observed for the Ge/Si(001) system [28].

- for the non-zero contact angle between island and substrate there is a stress singularity point at the edge. Here the mechanical stress reaches an infinite value [82]. The material in the direct vicinity of this point undergoes over-deformation (see strain scale). It was found that for islands with increasing height the stress at the island edge is a potential source of dislocations leading to plastic relaxation of stress in the island [83]. The strain energy at island edges is considered to be the cause of plastic relaxation of coalescent islands during the Ostwald ripening process [84].

Chapter IV

Experimental equipment and techniques

IV.1 Six-circle X-ray diffractometer

IV.1.1 Device overview

X-ray diffraction experiment requires precise control of the sample positioning relative to the incident X-ray beam, and of relative positioning of sample and detector. In the simplest case (coplanar diffraction) to set the sample in Bragg conditions it is necessary to move simultaneously the sample and the detector within the common plane with corresponding angle misfit θ ($\theta - 2\theta$ scan). $\theta - 2\theta$ geometry creates two degrees of freedom for sample scanning (δ, ω) and additional two degrees of freedom for sample alignment on the beam (χ, ϕ) (see Fig. 1). Such set-up is realized on a *four-circle diffractometer* [85]. Implementation of more complicated diffraction geometries (non-coplanar XRD and GID) requires the higher device flexibility. This leads to the appearance of further degrees of freedom for sample and detector (Fig. 1(right)). This particularity supplied such type of devices with an abbreviation *six-circle diffractometer* [86]. Here three angles (χ, ϕ, and ω) are used to align and scan the sample. The detector can rotate around two perpendicular axes, δ and γ. The sixths angle, α, enables the rotation of the whole apparatus with respect to the incident beam what is necessary to control the angle of incidence α_i. Under a movement of α, the detector position remains constant with respect to the sample surface, but changes with respect to the incident beam. The 2θ position of the detector in this case is a function of both degrees of freedom of the detector and of the incident beam angle:

$$\cos(2\theta) = \cos(\delta)\cos(\gamma)\cos(\alpha) - \sin(\gamma)\sin(\alpha) \quad \text{(IV.1)}$$

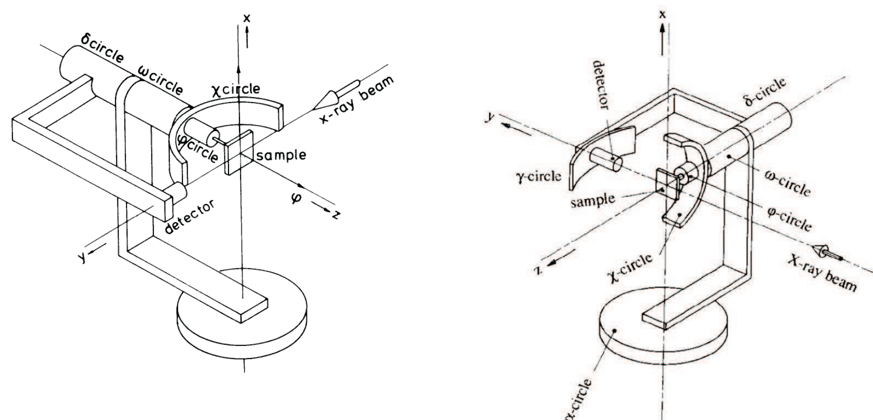

Figure 1: Four-circle (left) and six-circle (right) diffractometers.

IV.1.2 Diffractometer BW2

The six - circle X-ray diffractometer at the BW2 wiggler beam-line [87] (Fig. 2) is a highly versatile instrument for different kinds of X-ray diffraction experiments[1] [89], [88]. The X-ray radiation comes from a wiggler in the DORIS electron storage ring. The beam passes through a Si(111) double-crystal monochromator, which provides the photon energy selection in the range of ≈7 - 12 keV necessary for X-ray diffraction experiments. The focussing of the primary beam on the sample is provided by X-ray mirrors. The motors used on the diffractometer can be separated into three main groups: motors for *beam collimation* (slits), motors for *instrument alignment*, and the motors for *sample/detector movement* during the measurement. Slits and their related motors can be subdivided into *absorber* slits, *monitor* slits, and *detector* slits. Absorber slits regulate the initial horizontal width of the incoming X-ray beam. The incoming beam produced by the wiggler magnet is narrow in the vertical direction (<1mm). The horizontal width of the direct beam is adjustable (*absslit* function) from 1 - 20 mm. After the monochromator the beam goes through a *monitor* (ionization chamber), which measures the intensity of the primary beam. The whole monitor system including monitor slits can be moved horizontally and vertically (motors *moy* and *moz*). The photon flux can be reduced by introducing an iron or aluminium attenuator of known thickness between the absorber slits and the monitor (motor *attn*).

The beam collimation before the sample is achieved using two sets of vertical (*slud*) and horizontal (*sllr*) straight niobium slits. The beam size can be varied down to zero. The background noise due to scattering by the air can be reduced by the front *flight tube slit* (*ftslit*) with the minimum size of 0.5 mm.

[1] www.hasylab.desy.de/facility/experimental stations/stations/BW2.htm

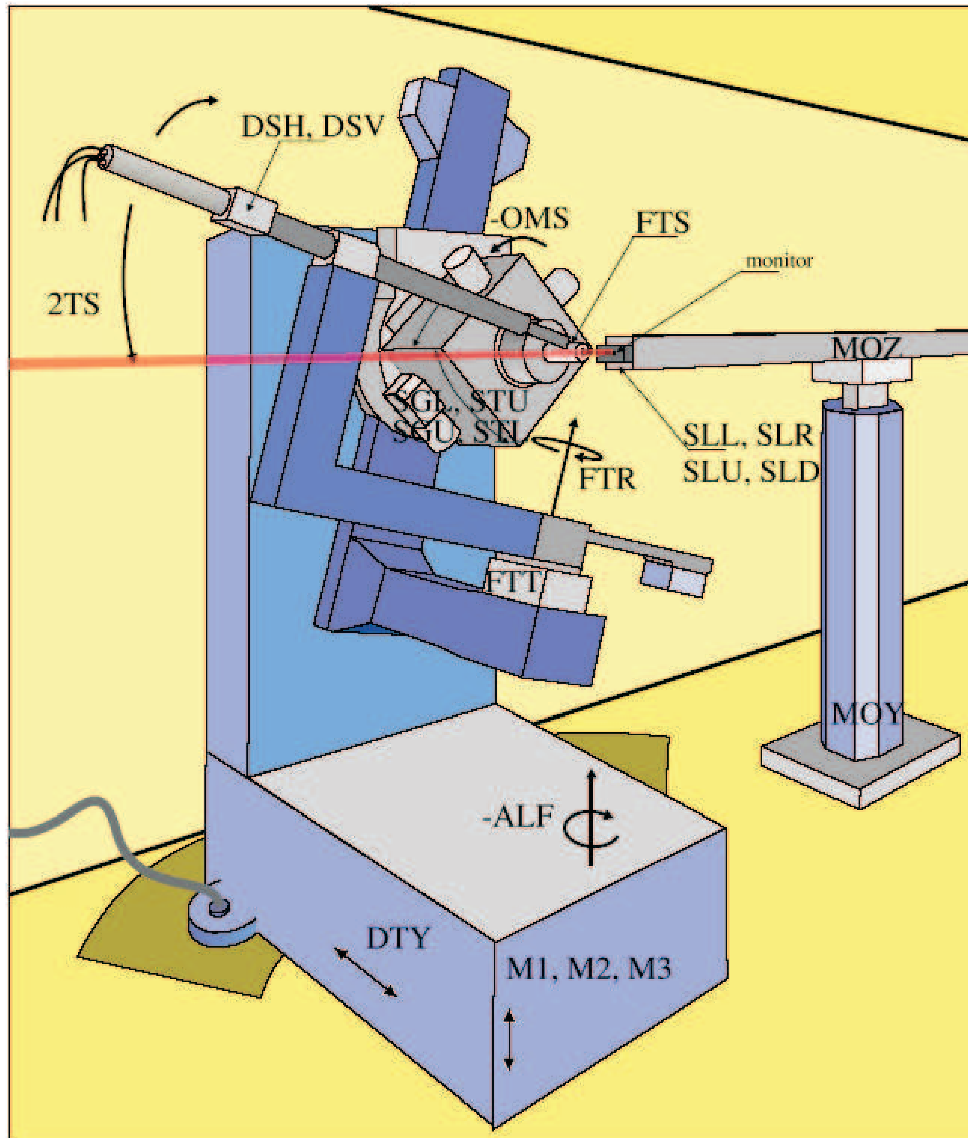

Figure 2: BW2 diffractometer.

The detector is mounted at the end of the flight-tube. The appropriate angular resolution of the detector is provided by the vertical (*dsv*) and horizontal (*dsh*) detector slits with the minimum size of 0.5 mm.

The sample and diffractometer alignment proceeds by means of adjustment of the position of the sample surface relative to the incident beam, position of detector relative to the sample, and diffractometer position relative to the beam. Sample alignment is performed by moving and tilting it in the beam (motors *stl*, *stu*, *sgl*, *sgu*). Sample alignment using a laser beam is convenient. Here the sample surface normal is brought parallel to the sample rotation axis by tilting the sample so that when it is rotated the laser spot remaines fixed. The sample is positioned to intersect half of the incident beam using motor *dty* (diffractometer translation along y axis).

To align the detector relative to the sample, the detector arm is moved with the flight tube translation motor (*ftt*) parallel to the sample surface normal. To keep the common position of the sample and the detector in the area of the incoming X-ray beam, the whole diffractometer can be moved with the help of three motors (*m1*, *m2*, and *m3*) using the special command *flom*. In grazing incidence geometry the sample movement is controlled by motor *alf* moving the whole diffractometer relative to the incident beam.

The rotation of the sample is provided by the motor *oms*, the rotation of the detector arm - by the motors *2ts* and *ftr*. These three motors determine the degrees of freedom for the area, where the detector can collect the signal scattered from the sample. The movement of motors *oms*, *2ts*, and *ftr* are controlled by executing macros, which provide the movement of the sample-detector system in reciprocal (h, k, l) space.

IV.2 Special equipment

IV.2.1 Vacuum chamber for X-ray diffraction experiments

X-ray diffraction experiments under ultra-high vacuum conditions were performed using a "baby-chamber" - a portable vacuum chamber with Be-hemispherical window (see Fig. 3). The Be hemispherical window is transparent for the X-ray photon energies above 6 keV. The vacuum is maintained by an ion getter pump (pressure $< 5 \cdot 10^{-9}$ mbar). To maintain the high weight of the chamber properly aligned on the diffractometer a specially designed holder is used.

IV.2.2 He-chamber for X-ray diffraction experiments

In diffraction experiment using highly intensive synchrotron radiation the effects of the sample-beam interaction cannot be neglected (see section VI). Hence contact between the sample and the ambient air during experiment should be avoided. The

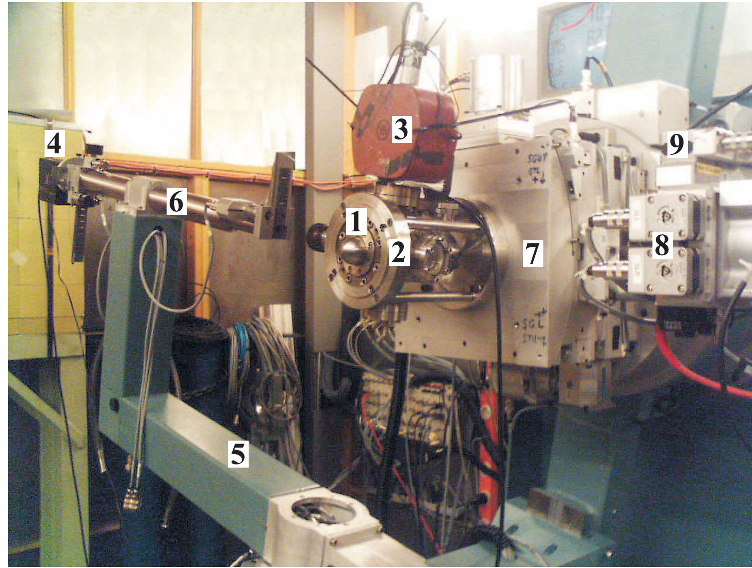

Figure 3: BW2 diffractometer set-up with UHV X-ray chamber. 1 - Be window of the chamber, 2 - chamber metal holder, 3 - vacuum pump, 4 - X-ray eye, 5 - detector arm, 6 - detector flight tube, 7 - sample goniometer table, 8 - monitor (incoming beam) slits, 9-monitor electronics.

diffraction experiments on samples, which had been exposed to air, were performed in a He atmosphere. For this purposes, the special chamber constructed in the University of Würzburg was used (Fig. 4). The chamber has side walls made of Kapton foil, transparent for X-ray radiation. It can be filled with He gas with a slight overpressure.

IV.3 X-ray diffraction geometries

IV.3.1 Terminology

The main parameter determining the difference between scattering geometries is the position of the diffraction vector $\mathbf{Q}$ determined by the incoming $\mathbf{K^{IN}}$ and scattered $\mathbf{K^{OUT}}$ wave vectors.

$$\mathbf{Q} = \mathbf{K^{OUT}} - \mathbf{K^{IN}} \tag{IV.2}$$

The vertical component of reciprocal vector, $\mathbf{q_z}$, is set to be parallel to the crystal(substrate) surface normal. The mutually orthogonal $\mathbf{q_x}$ and $\mathbf{q_y}$ components lie in crystal(substrate) surface plane. If both vectors $\mathbf{K^{IN}}$ and $\mathbf{K^{OUT}}$ are in the plane of surface normal, this diffraction set-up is called *coplanar*. If in the coplanar geometry only variations of the $\mathbf{q_z}$ component are analyzed, this case is called *symmetrical*. If variation of $\mathbf{q_z}$ and $\mathbf{q_x}(\mathbf{q_y})$ components are necessary, an *asymmetrical* setup is used.

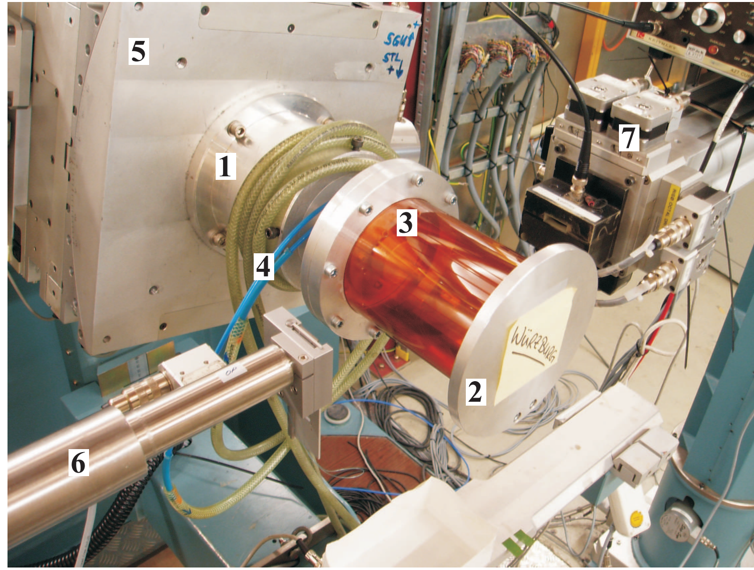

Figure 4: BW2 diffractometer set-up with the He-chamber. 1- chamber connection unit for the diffractometer. 2 - metal holder for the Kapton foil screen (3), 4 - connection to the He line, 5 - sample goniometer table, 6 - detector flight tube, 7 - monitor slits

For a thick substrate crystal with a flat surface the **Q** are restricted. The first limitation is due to the fact that the Ewald sphere has a maximum radius of $1/\lambda$. In the presence of a strongly absorbing thick flat crystal one half of the sphere is "shadowed" by the sample. The vertical components for the incoming and outgoing wave vectors are also limited by:

$$\mathbf{k_z^{IN}} \leq 0 \text{ and } \mathbf{k_z^{OUT}} \geq 0 \tag{IV.3}$$

This leads to the appearance of additional "dead" zones, or sub-spheres, within the Ewald sphere, or half-spheres for the flat sample, with radius of $1/(2\lambda)$, which are inaccessible.

For a [001]-oriented zinc-blende substrate crystal the accessible part of the reciprocal space is shown in the Fig. 5. Here the marked lines and colored slices represent 1D scans and 2D cuts of reciprocal space. The reflections being in the dead areas can be brought into the allowed part of the reciprocal hemisphere by in-plane rotation of the sample (angle θ in the Fig. 5).

The general diffraction geometry is shown in Fig. 6. Here each of the incoming and outgoing wave vectors is determined by two main angles, θ and α, corresponding

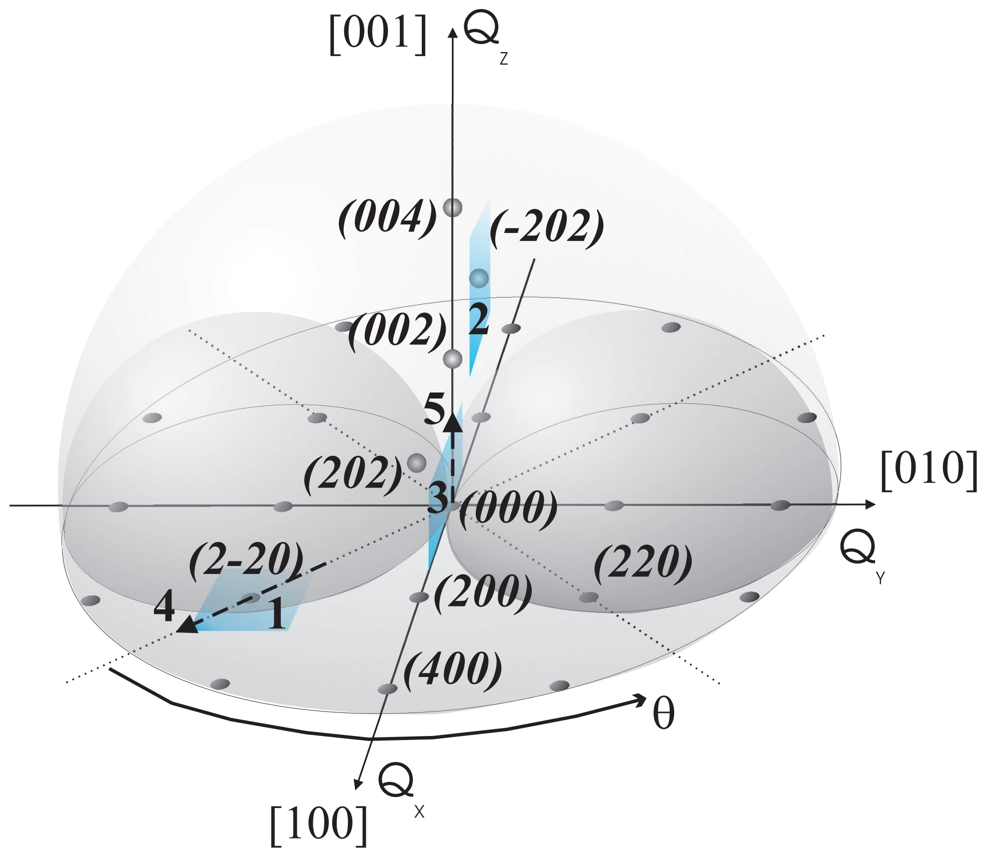

Figure 5: Accessible part of the reciprocal space for [001]-oriented zinc-blende single-crystal. **Q** values inside the volumes limited by two small hemispheres are forbidden and can be brought into the allowed part of reciprocal space by in-plane rotation of the whole coordinate system (angle θ). Numbered lines and slices of reciprocal space represent the main diffraction geometries used. 1 - GID in-plane mapping; 2 - HRXRD out-of-plane mapping; 3 - GISAXS out-of-plane mapping; 4 - GID line scanning; 5 - XRD/reflectivity.

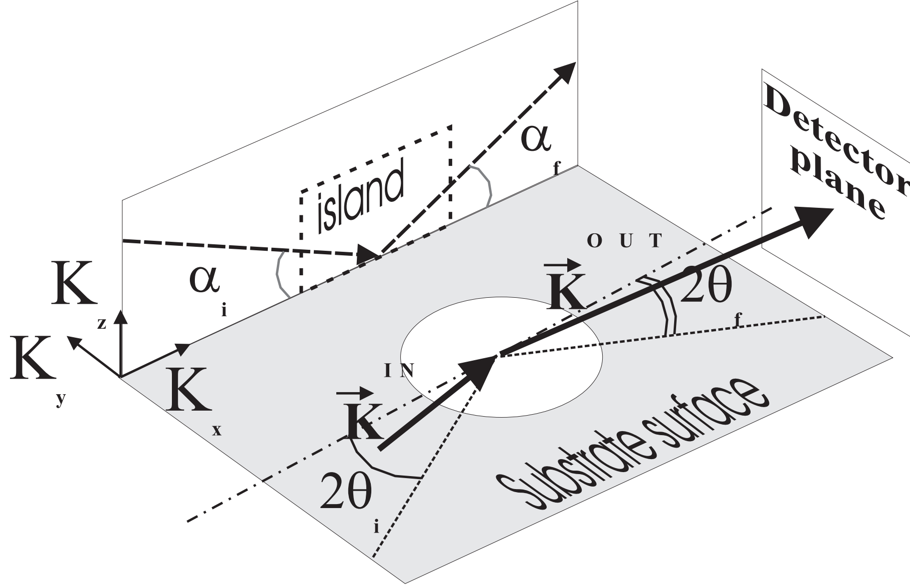

Figure 6: Diffraction geometry in angular space. General case.

to projections on the $x(y)$, and z- axes. Using these angles, vector $\mathbf{Q}$ can be written:

$$\mathbf{Q} = k \begin{pmatrix} \cos(\alpha_f)\cos(2\theta_f) - \cos(\alpha_i)\cos(2\theta_i) \\ \cos(\alpha_f)\sin(2\theta_f) - \cos(\alpha_i)\sin(2\theta_i) \\ \sin(\alpha_f) + \sin(\alpha_i) \end{pmatrix} \quad \text{(IV.4)}$$

where $k = |\mathbf{k}| = 2\pi/\lambda$.

IV.3.2 Grazing incidence small angle X-ray scattering (GISAXS)

In the GISAXS geometry the momentum transfer varies in the vicinity of the sample surface normal, see Fig. 7. In the grazing incidence regime with $\theta_i = 0$, the components of the diffraction vector are:

$$\begin{aligned} \mathbf{q_x} &= k(\cos(\alpha_f)\cos(2\theta) - \cos(\alpha_i)) \\ \mathbf{q_y} &= k(\cos(\alpha_f)\sin(2\theta)) \\ \mathbf{q_z} &= k(\sin(\alpha_f) + \sin(\alpha_i)) \end{aligned} \quad \text{(IV.5)}$$

where the vertical resolution $\delta(\mathbf{q_z})$ is determined primarily by the angles $\alpha_i = \alpha_f$ and is in the order of 10^{-3} $\mathring{A}^{-1}$. The absolute value of the vertical component is close to zero. From Fig. 5 (cut 3) the one lateral component, say $\mathbf{q_y}$, does not have any restrictions. GISAXS can allow one to investigate the lateral dimensions of the objects, which are smaller then 0.1μm. The main restriction is the lateral resolution:

$$\frac{d\mathbf{Q_y}}{d\theta}\delta(\theta) + \frac{d\mathbf{Q_y}}{d\alpha_f}\delta(\alpha_f) \approx 2k(\delta(\theta) + \alpha_f\theta\delta(\alpha_f)) \approx 1 \cdot 10^{-3}\mathring{A}^{-1} \quad \text{(IV.6)}$$

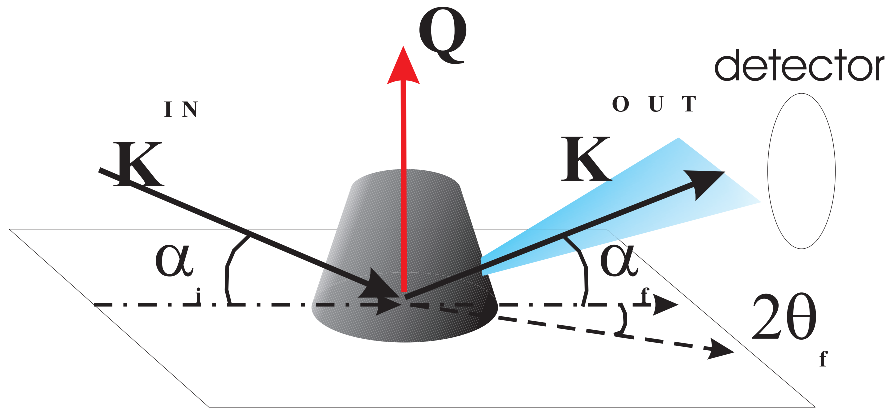

Figure 7: Grazing incidence small angle X-ray scattering geometry.

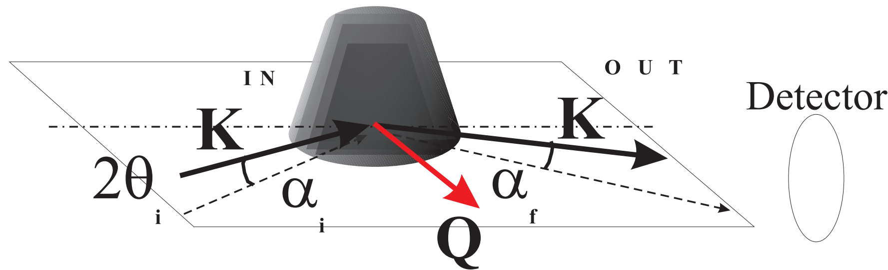

Figure 8: Grazing incidence X-ray diffraction geometry.

When the small values of q_z and q_y vectors are used (area close to the specular primary beam), the GISAXS geometry is used for analysis of shape and spatial distribution of sub-micrometer small crystals [90],[91].

As the diffuse scattered intensity measured in GISAXS is rather weak, long integration times are required to obtain sufficient statistics of the recorded signal.

IV.3.3 Grazing incidence diffraction (GID)

In the GID geometry, a reflection process at the sample surface due to small angles of incidence and exit, $\alpha_{i,f}$, is combined with a diffraction process, Fig. 8. Consequently, the investigated Bragg reflection lies within the $\mathbf{q_x}-\mathbf{q_y}$ plane, and the Bragg condition is fulfilled for a sample azimuth for which the reflection lies close to the border of the forbidden zones (cut 1 and line scan 4 in Fig. 5). The reciprocal space coordinates

are related to the angles by:

$$\begin{aligned} \mathbf{q_x} &= -\mathbf{q}_{\|} \cos\beta \\ \mathbf{q_y} &= -\mathbf{q}_{\|} \sin\beta \\ \mathbf{q_z} &= k(\sin(\alpha_f) + \sin(\alpha_i)) \end{aligned} \tag{IV.7}$$

with $\mathbf{q}_{\|} = k\sqrt{\cos^2(\alpha_i) - 2\cos(\alpha_i)\cos(\alpha_f)\cos(2\theta) + \cos^2(\alpha_f)}$, and $\sin\beta = \frac{k\cos(\alpha_f)\sin(2\theta)}{\mathbf{q}_{\|}}$. The GID-resolution is typically about $5 \cdot 10^{-3} \mathring{A}^{-1}$. As $\mathbf{q_z}$ is also virtually zero in this geometry, only lattice strains parallel to the sample surface can be obtained in GID. In addition, the negligible vertical component of the diffraction vector allows GID-data to be analysed using the kinematical approximation. The main advantage of GID is its sensitivity to thin layers near the surface. In GID experiments on nano-scale objects, the incoming beam covers the maximum surface area and so provides the highest possible intensity. This is especially important if the surface densities of scattering objects (islands) are small.

IV.3.4 Surface-sensitive asymmetrical X-ray diffraction (GI-HRXRD)

This technique combines the advantages of GID and coplanar diffraction (XRD). It is the sensitivity to thin layers at the sample surface due to the small incidence angle, and the highly resolved finite vertical momentum transfer $\mathbf{q_z}$ makes the geometry sensitive to the vertical arrangement of atoms. The GI-HRXRD technique exploits a fourth degree of freedom in reciprocal space, as illustrated in Fig. 9. In the GI-HRXRD geometry, all three components define the respective values of the diffraction vector $\mathbf{Q}$. The diffraction plane, i.e. the plane spanned by $\mathbf{K^{IN}}$ and $\mathbf{K^{OUT}}$, can be rotated around the diffraction vector $\mathbf{Q}$. In GI-HRXRD, the incidence angle α_i is fixed below the substrate critical angle. For such α_i the scattering geometry becomes surface sensitive. The probed reciprocal lattice points (RLP) for which grazing angle is allowed are those which lie within the dead zones and are inaccessible in coplanar XRD geometry, e.g. (202) reflection, (reciprocal cut 2 in Fig. 5) .

This geometry requires a special set-up where the detector can be moved over a large angular range around two axes, in our case, driven by motors *ftr* and *2ts*. In addition, due to the small incidence angle, most of the incident intensity is specularly reflected. Hence this scattering geometry is only feasible with very intense synchrotron X-ray sources.

IV.3.5 X-ray reflectometry (XRR).

X-ray reflectometry represents an extreme case of coplanar XRD. Here only the vicinity of the origin of reciprocal space is probed. Similar to GISAXS, XRR is completely

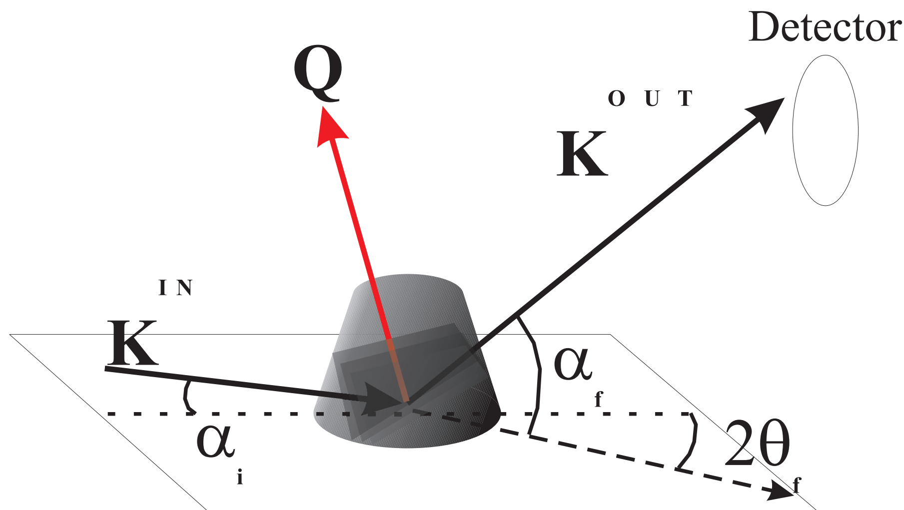

Figure 9: Grazing incidence X-ray diffraction geometry.

insensitive to the crystalline state of the sample. Only the variation of the average electron density (refractive indices of the constituent materials) in the sample is important in XRR. Therefore this geometry is suited to determine layer thicknesses, composition, interface and surface roughness [101], [102],[103].

Due to the coplanar geometry only the vertical component of the diffraction vector $\mathbf{q_z}$ need to be considered, Fig. 10. In XRR the incidence angle α_i is commonly referred as ω, and the scattering angle as 2θ. The exit angle is then $\alpha_f = 2\theta$-ω. For typical angular resolution $\Delta\omega = \Delta\theta = 0.01°$ the reciprocal space resolution is:

$$\begin{aligned} |\Delta \mathbf{q_z}| &= |\frac{\delta \mathbf{q_z}}{\delta \omega}|\Delta\omega + |\frac{\delta \mathbf{q_z}}{\delta \theta}|\Delta\theta \\ &= 2k\sin(\theta)\sin(\omega-\theta)\Delta\omega + 2k\cos(\omega)\Delta\theta \\ &\approx 2k\Delta\theta \approx 1.5\cdot 10^{-3}\text{Å}^{-1} \end{aligned} \tag{IV.8}$$

IV.3.6 Summary

The main differences between the diffraction geometries for [001]-oriented crystals are summarized in Table IV.1.

IV.4 Surface imaging tools: Atomic force microscopy

Atomic force microscopy (AFM) is a *scanning probe technique* that can resolve nanometer size features [92]. The basic principle is illustrated in the Fig. 11. AFM works by bringing a cantilever, typically made of silicon or silicon nitride with a tip size in

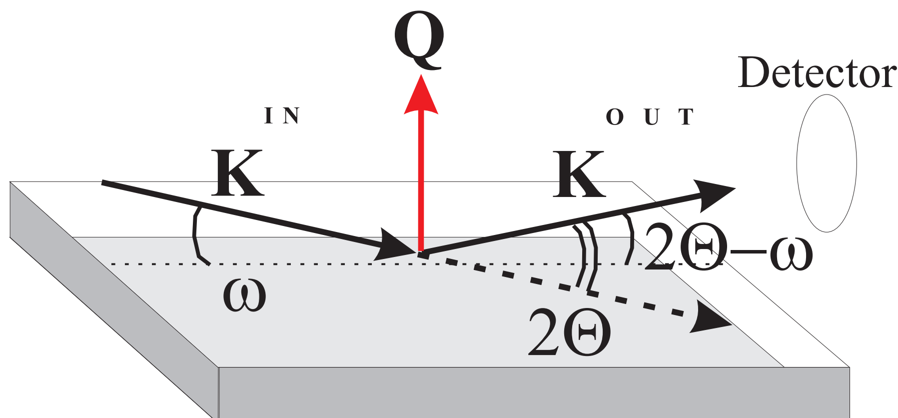

Figure 10: Geometry of X-ray reflectometry.

diffraction geometry	Sensitivity to atomic arrangement in lateral ($\mathbf{q_x}$, $\mathbf{q_y}$) and vertical ($\mathbf{q_z}$) directions			Sensitivity to crystallite/island shape and relative arrangement		
	$\mathbf{q_x}$	$\mathbf{q_y}$	$\mathbf{q_z}$	$\mathbf{q_x}$	$\mathbf{q_y}$	$\mathbf{q_z}$
GISAXS	no	no	no	yes	yes	no
GID	yes	yes	no	yes	yes	no
GI XRD	yes	yes	yes	yes	yes	yes
XRR	no	no	no	no	no	yes

Table IV.1: Sensitivity of different diffraction geometries.

the order of nanometers, in contact with the surface to be imaged. A repulsive force from the surface applied to the tip bends the cantilever upwards. The amount of bending, measured by a laser spot reflected onto a split photo-detector, can be used to calculate the force using Hookes law:

$$\Delta z = \frac{\delta F}{k_c} \tag{IV.9}$$

where Δz is the change of cantilever position along z axis detected by the photo-detector, δF is the force applied to the cantilever, and k_c is the spring constant of the cantilever. Experiments have shown that a repulsive force of 1nN changes the cantilever height by $1\mathring{A}$. By keeping the force constant while scanning the tip across the surface, the vertical movement of the tip follows the surface and so the surface topography can be measured.

The AFM can work well even in air. In addition, AFM measurement does not depend on the conductivity of the sample. This makes AFM an excellent tool for fast

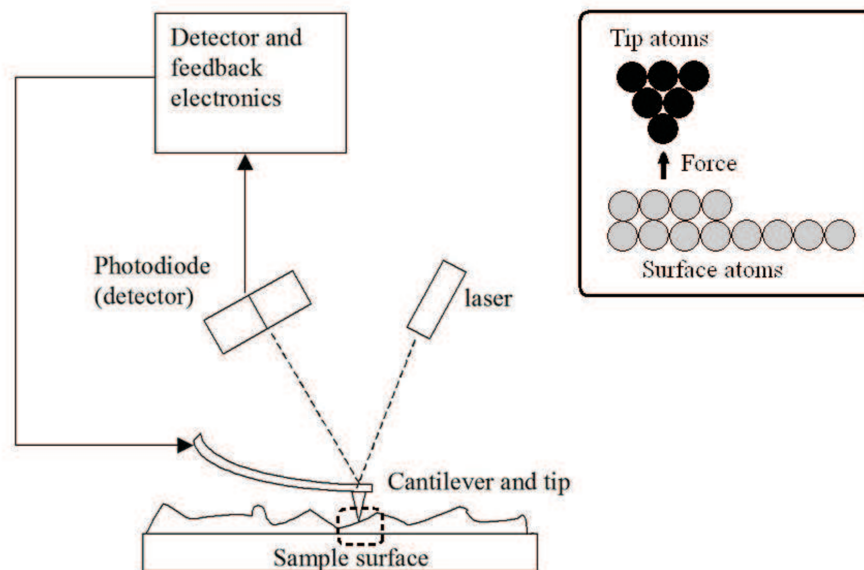

Figure 11: Schematic of an AFM.

surface topography investigations. In the ideal case the resolution of AFM depends on the radius of the cantilever tip [93]:

$$d_{exp} = 2\sqrt{d_{real}(R_{tip} + d_{real}/4)} \tag{IV.10}$$

where d_{real} is the real lateral size of the measured object, d_{exp} the lateral size of the object determined by AFM, and R_{tip} is the radius of cantilever tip. The tip radius is the front part of the conical tip closest to the sample surface. For surfaces with nanometer height roughness - in our case nm-size islands - the resolution decreases rapidly. If we consider an island size of 20 nm and tip radius of 1 nm, then according to Eq. IV.10 the estimated island size will differ from its real value by at least 10%.

IV.5 Numerical techniques.

IV.5.1 Calculation of intensity patterns from elastically strained islands.

The displacement field derived from the finite element (FEM) model was used to calculate the diffuse intensity distribution.

For non-buried islands on the substrate the kinematical calculations were made by numerical integration (Eq. II.53) using the island dimensions as a boundary con-

ditions for shape function. For buried islands the model calculations involved the displacement field generated in the surrounding matrix material.

A net of acquisition points was created to retrieve the 2D displacement field from the 2D FEM solution. At these points the vertical and lateral projections of displacement vector were calculated. At each point (X,Y) in the FEM coordinate system, the mechanical displacement was determined using a spline procedure. The derived 2D displacement field was then used for the numerical computation of integral (II.53).

IV.5.2 Calculation of GISAXS intensities.

In a GISAXS experiment the scattering amplitudes can be determined using the crystal shape integral (see II.6).

The software package IsGISAXS, developed by *R.Lazari* [94] can simulate out-of-plane ($\mathbf{q_x}$, 0, $\mathbf{q_z}$) GISAXS intensity distributions using both kinematic (BA) and distorted wave (DBWA) approximations [95].

In this thesis the IsGISAXS program was used to determine the island shape (including size distribution and inter-island correlation effects) by numerical calculations.

IV.5.3 Calculation of XRR intensity profiles.

The calculation of the theoretical reflectivity curves and the best-fit model optimisation were done using the *fewlay* software package [96]. This program is based on the approximate solution (Parrat; L.N'evot and P.Croce, see II.12) for dynamical scattering from layered structures [98].

Chapter V

Theoretical study of the correlations between island shape and strain and the X-ray diffuse pattern.

In this chapter the sensitivity of the island strain field to changes in island morphology and composition will be investigated. The limits of the simplified linear and FEM approaches to describe the process of elastic relaxation in islands will be discussed.

V.1 Island without displacement field. Shape function.

In this section the features of diffuse pattern related to the shape function will be shown.

Kinematical approach. In the absence of a displacement field an island can be described as a single crystal with a particular lattice constant and shape. The position of island diffraction maxima can be derived using the equation:

$$|\mathbf{Q_{hkl}}| = \frac{2\pi}{d_{hkl}} \tag{V.1}$$

where d_{hkl} is a distance between crystal lattice planes of the order (hkl). For a [001]-oriented single crystal, the projection of each component of diffraction vector $\mathbf{Q}$ on each principal axis in reciprocal space can be simplified to:

$$|\mathbf{Q}| = \frac{2\pi n}{a} \tag{V.2}$$

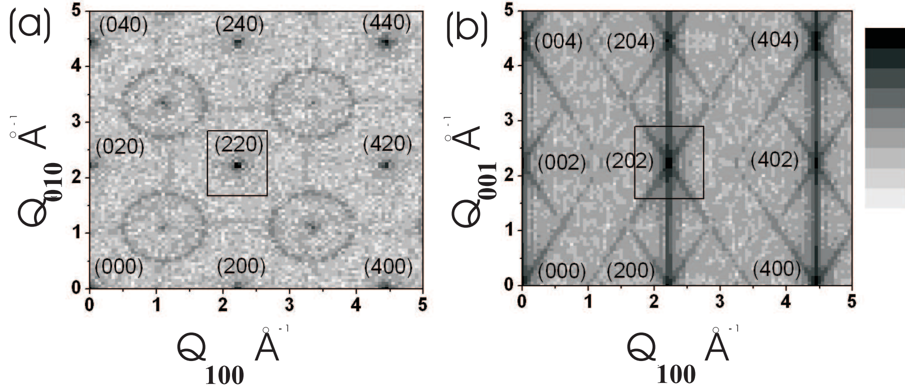

Figure 1: In-plane ($\mathbf{Q_{100}}, \mathbf{Q_{010}}, 0$) (a) and out-of-plane ($\mathbf{Q_{100}}, 0, \mathbf{Q_{001}}$) (b) reciprocal space cross-sections calculated for conical island (a=5.6533Å, H=50Å, R_0=100Å, α=26.5°). The areas around (202) and (220) Bragg reflections, marked by black rectangles, are shown in Fig. 2 with higher resolution

where a is a crystal lattice constant, and n is the order of the Bragg reflection. The intensity distribution around central diffraction maximum of each reflection is described by the Fourier transformed crystal shape function.

To show the shape function effect, the diffuse intensity pattern of a conical island (a=5.6533Å, height H=50Å, diameter D=200Å, base angle [1] α=26.5°) is presented in Fig. 1. The kinematically calculated in-plane ($\mathbf{Q_{100}}$, $\mathbf{Q_{010}}$, 0) and out-of-plane ($\mathbf{Q_{100}}$, 0, $\mathbf{Q_{001}}$) patterns are shown. On both reciprocal space slices, the intensity maxima from reflections of four orders can be observed, corresponding to the zinc-blende crystal structure. Pronounced differences between in-plane and out-of-plane reciprocal lattice point shapes can be observed. In the in-plane projection, the allowed Bragg reflections are the points. In addition, ring-like intensity patterns are found around forbidden Bragg reflections. These intensities are parts of out-of-plane truncation cones (see below) coming from allowed Bragg points below the investigated reciprocal space cut.

This pattern is orders of magnitude weaker, than that of allowed reflections. In Fig. 1(b) one can see vertical and tilted stripes going through the maximum positions of the allowed Bragg reflections. These stripes are results of truncation effects on the island outer surface and are called *truncation rods.* Higher resolution reciprocal space maps around the (220) and (202) Bragg reflections are shown in Fig. 2. It can be seen, that the Fourier transformation of an [001] axially symmetric strain-free island is an axially symmetric function with the symmetry axis along the $\mathbf{Q_{001}}$ direction. The complex oscillatory behavior of the intensity pattern in Fig. 2(a) can be described

[1] angle between the island base normal and the normal to the cone surface

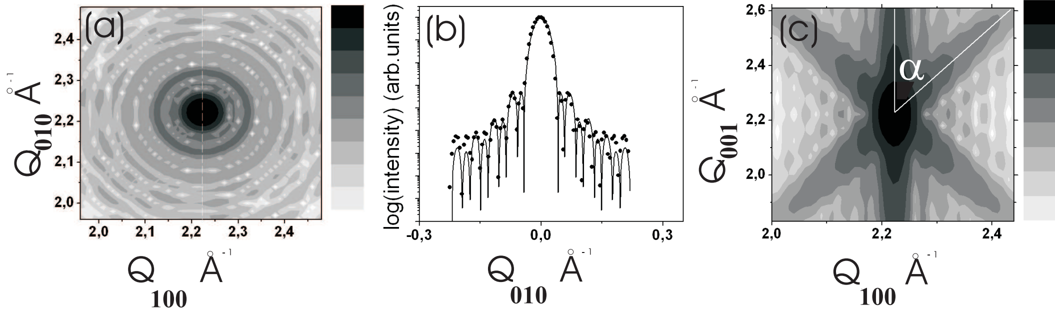

Figure 2: Calculated intensity patterns in the vicinity of (220) (a) and (202) (c) island Bragg reflections. Intensity distribution along dashed line cut on plot (a) calculated using atomistic (full circles) and analytical (line) approaches is shown on plot (b).

analytically by scattering amplitude:

$$F(\mathbf{Q}, R, H, \alpha) = \int_0^H 2\pi R_z^2 \frac{J_1(|\mathbf{Q}_\parallel| R_z)}{|\mathbf{Q}_\parallel| R_z} \qquad \text{(V.3)}$$

where $\mathbf{Q}$ is the diffraction vector with its in-plane projection $\mathbf{Q}_\parallel$, R is the island base radius, H the island height, α the island base angle, and $J_1(x)$ a Bessel function of first order.

The line scan through the Bragg peak maximum (dashed line in Fig. 2(a)) calculated using both atomistic island model and analytical expression V.3 are plotted in Fig. 2(b). For a strain-free island both approximations agree well. The full width half maximum (FWHM) in Fig. 2(b) is related to the maximum island base diameter (FWHM=0.0155 $\mathring{A}^{-1}$ corresponds to an island diameter of $\approx 200\mathring{A}$). From the angle between the tilted and vertical intensity streaks in Fig. 2(c) one can determine the island base angle α.

Distorted wave approximation (DWBA). In principle Fourier analysis can reveal information about the island morphology and crystal structure for nanoscale strain-free islands. Real SK-islands are *not* strain-free and the combined effects of shape function and strain field on the diffuse intensity pattern have to be taken into account (see II.8). The analysis of the shape function alone for strained islands is only possible in the GISAXS scattering geometry (see IV.3.2), when the diffuse pattern in the vicinity of the primary beam is measured. To get a detectable signal from real island samples, the grazing incidence geometry is used (see IV.3.3). Under these conditions, four-beam scattering takes place (see II.11.2).

To establish the sensitivity of GISAXS to changes of the parameters of the lens-shaped islands, model calculations for $\alpha_{in} = 0.15°$ were carried out. In the calculations the lens-shaped islands were approximated by rotational trapezoids. The island height-to-radius ratio (HRR) was varied. The calculated out-of-plane GISAXS pat-

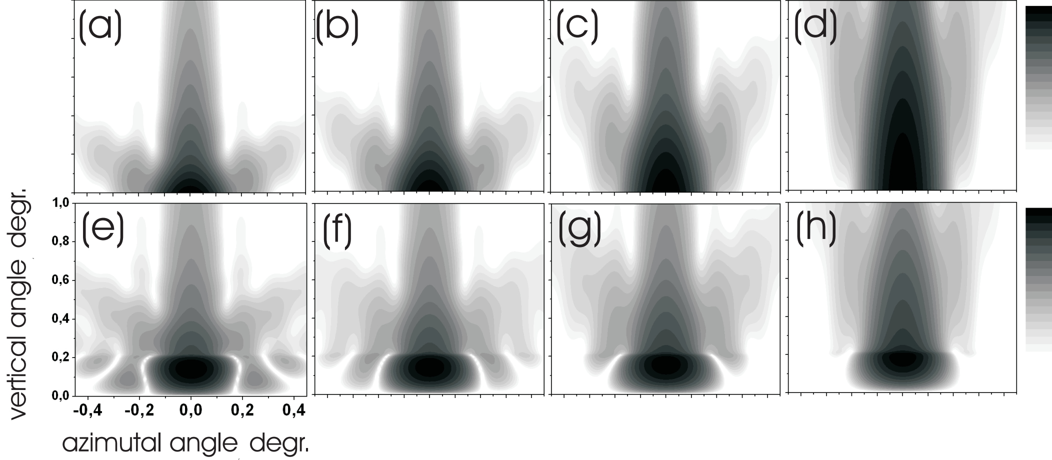

Figure 3: Calculated out-of-plane island GISAXS patterns in kinematical (upper row) and DWBA (lower row) approximations. Conical islands with base radius R_0=30nm and varying HRR ratio (HRR=1 (a,e), 0.75 (b,f), 0.5 (c,g), and 0.25 (d,h)) were used.

terns for conical island (R_0=30nm) with varying HRR parameter are shown in Fig. 3. Both kinematic and DWBA calculations are presented. Reflection/refraction effects cause significant changes in the kinematic diffraction pattern.

V.2 Island with displacement field. Linear approximation versus FEM.

Before the complex FEM model is discussed, a simplified approximation for strain relaxation will be considered using iso-strain area model (see II.11.3). The assumptions of this model are fulfilled for islands, in which the lattice constant varies linearly from the bulk substrate crystal value at the base to the bulk value of island material at the top. The corresponding changes in vertical lattice displacements are determined by Hookes law (see Eq. III.12).

The linear approximation (LA) has obvious advantages: It can be easily implemented (see App. B), it is independent of the mechanical properties of the substrate and does not require complex calculations using FEM. The main weakness of the LA approach is that it describes the deformation in the island independently on its shape and mismatch strain relative to the substrate.

The morphology of the island, constrained by the substrate strongly influences the displacement field (see next sections). The applicability of the LA approximation to islands with low (ϵ_{max} =-1%) and high (ϵ_{max} ≈-6.7%) lattice mismatch will be compared to the FEM results.

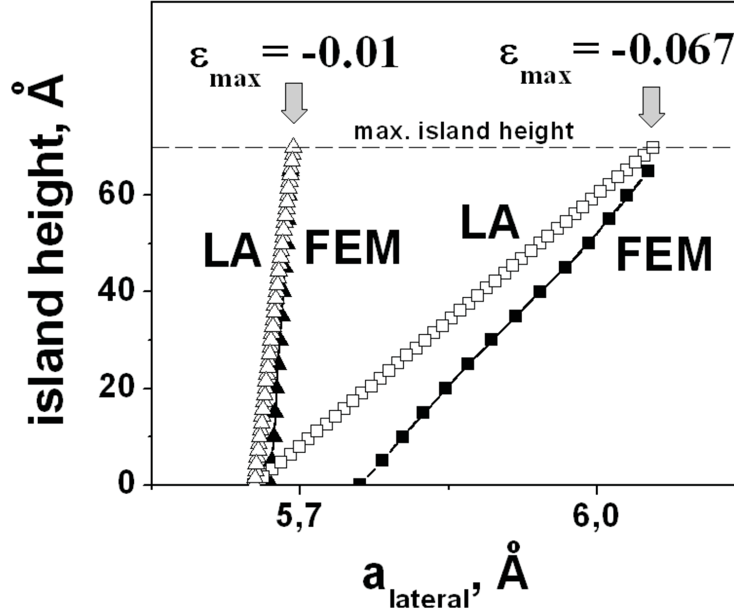

Figure 4: Lateral lattice constant profile as a function of island height, calculated for strained conical islands for low (ϵ_{max}=-0.01 and high (ϵ_{max}=-0.067) misfit deformation values for the LA and FEM.

Conical islands with base radius R_0=15nm and height H=7nm were usd for the model calculation[2].

Low deformation case. The lateral lattice constant distributions as a function of the island height for island with ϵ_{max} =-1%, derived from LA and FEM (in the case of FEM $\epsilon_{lateral} = \epsilon_{xx}$ values along the island vertical symmetry axis[3]), are shown in Fig. 4. It can be seen, that for small lateral deformation both methods yield similar results. To analyse the island 3D strain profiles the reciprocal space maps (RSM) in the vicinity of in-plane (220) and out-of-plane (202) substrate bulk reflections shown in Fig. 5 were calculated. Diffraction vector values are given in reciprocal lattice units (r.l.u.) relative to the bulk substrate. It can be concluded, that for deformations up to ≈1% the strain field in the island can be adequately described by the LA.

Large deformation case. For ϵ_{max} ≈-6.7% large discrepancies between LA- and FEM- calculated lateral strain profiles are found (Fig. 4). The difference is largest at the island base and diminishes continuously towards the top. The origin is the island/substrate mismatch, which has to be taken into account. The interaction at the interface leads to a mutual deformation of the island and the underlying substrate

[2]these dimensions are intermediate between island sizes for InAs/GaAs(001) and InAs/AlAs(001). See VIII

[3]axis Y in 2D FEM model

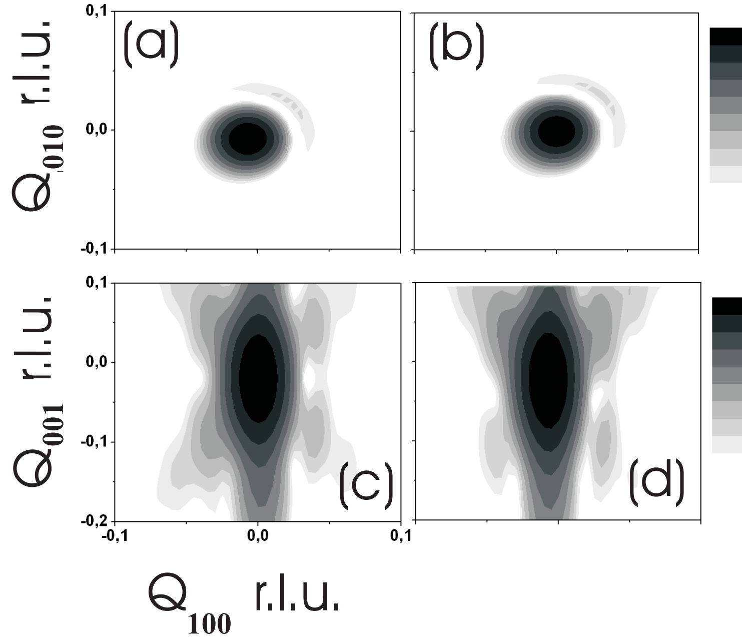

Figure 5: Diffuse intensity patterns, calculated in the vicinity of the in-plane (220) (a,b), and out-of-plane (202) (c,d) substrate Bragg reflection (Q_{100}= Q_{010}= Q_{001}=0, [r.l.u.]) for gradually strained conical islands with a maximum misfit deformation ϵ_{max}=-0.01. Island displacement fields were created using LA (a,c) and FEM (b,d).

(see III.3.4).

Calculated in-plane and out-of-plane RSMs are shown in Fig. 6. For both approximations, the influence of the shape function on the in-plane intensity pattern should also be noticed. In the radial direction ($\mathbf{Q_{100}}$=$\mathbf{Q_{010}}$), the intensity decay from the position corresponding to the island lateral lattice constant at its base towards the position of bulk island material (negative **Q** values on the plot) takes place. Within this range of **Q** values, the intensity distribution is related to changes in the island dimensions. This effect will be analysed in the next section. The additional intensity streaks on the in-plane pattern are complex. It is known, that the shape and position of these streaks are connected to the lateral deformation field gradient in the islands.

Under high deformation the outer parts of the conical islands undergo bending (see III.3.4), which changes the shape of the iso-strain areas. Compared to the LA diffraction pattern, the out-of-plane FEM patterns then also reveal difference. For lattice mismatches greater than -1% only FEM calculations give reliable values for island displacement field.

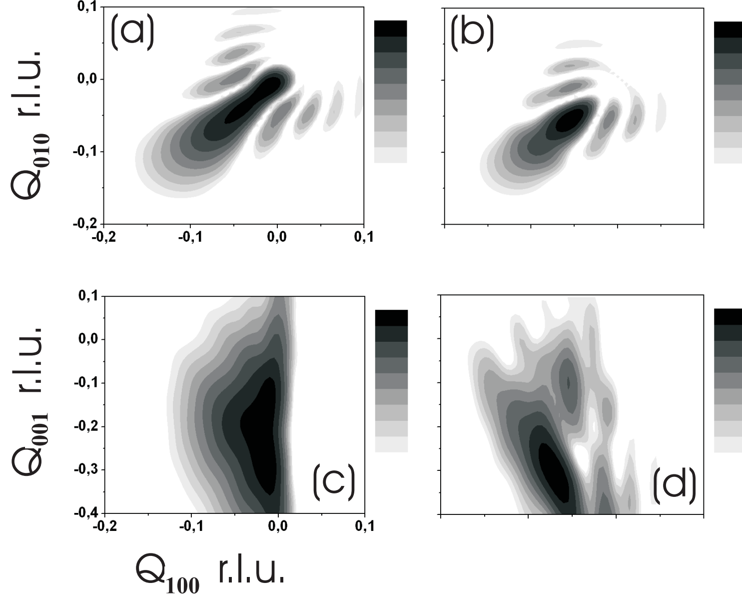

Figure 6: Diffuse intensity patterns, calculated in the vicinity of the in-plane (220) (a,b), and out-of-plane (202) (c,d) substrate Bragg reflection (Q_{100}= Q_{010}= Q_{001}=0, [r.l.u.]) for gradually strained conical islands with a maximum misfit deformation ϵ_{max}=-0.067. Island displacement fields were created using LA (a,c) and FEM (b,d).

V.3 Limitations to analytical shape extraction for strained islands using in-plane diffraction.

The in-plane diffuse intensity pattern from strained islands contains information about the island lateral displacement field and shape function. The effect of both parameters on the diffuse pattern is complex. Certain simplifications, based on ISA island model (see II.11.3), can be used to separately analyse the lateral strain profile and the shape of non-capped quantum dots. To provide a sufficient resolution of each ISA zone with particular lateral lattice constant, the vertical gradient of lateral strain field should be maximal. If the radial in-plane reflection (i.e. (220)) is analysed, then this limitation can be written as [97]:

$$\frac{dQ_{\parallel}}{dz}H \to \infty \tag{V.4}$$

where $Q_{\parallel} = |\mathbf{Q}_{\parallel}| = \sqrt{Q_x^2 + Q_x^2}$, z is the height of particular ISA over the substrate level, and H is the maximum island height.

The second limiting parameter is the lateral size *R(z)* of each particular iso-strain area, which should be large enough to provide the sufficient sharpening of ISA shape

function, and so, the maximal separation of neighboring ISA reflections:

$$R(z) \to \infty \tag{V.5}$$

Both limitations are considered in the relation [97]:

$$\frac{dQ_{\parallel}}{dz} H R(z) \gg 1 \tag{V.6}$$

In the LA model (suitable approximation for Eq. V.4), the lateral lattice constant a in the island with the lattice mismatch relative to that of the substrate (a_{sub}) changes linearly as a function of z up to its maximum a_{top} value at height H at the top of the island:

$$a = a_{sub} + \frac{a_{top} - a_{sub}}{H} z \tag{V.7}$$

In equation V.7 we introduce the mismatch strain, defined as $\epsilon_{max} = \frac{a_{sub} - a_{top}}{a_{top}}$. Then:

$$a = a_{sub} - \frac{\epsilon_{max} a_{top}}{H} z \tag{V.8}$$

For conical islands, the radius of each ISA as a function of z is given by:

$$R_{ISA} = R_0 - \frac{z}{\tan(\alpha)} \tag{V.9}$$

where R_0 is the island base radius, and α is the island base angle.

The size of each ISA in reciprocal space is given by Δ_{ISA} (FWHM). It is related to the ISA diameter D_{ISA}=2R_{ISA}:

$$\Delta_{ISA} = \frac{2\pi}{D_{ISA}} = \frac{\pi}{R_{ISA}} \tag{V.10}$$

For island with gradually vanishing lateral dimensions Δ_{ISA} from linear becomes an asymptotical function for R_{ISA} values in the vicinity of island top ($\Delta_{ISA} \to \infty$ for $R_{ISA} \to 0$). Equation V.9 can be rewritten in the form:

$$R_{ISA} = R_0 - \frac{H}{\tan(\alpha)} \frac{(a_{sub} - a)}{\epsilon_{max} a_{top}} = R_0 - \frac{H}{\tan(\alpha)} \frac{\epsilon_{ISA}}{\epsilon_{max}} \frac{a_{ISA}}{a_{top}} \tag{V.11}$$

where ϵ_{ISA} is the lateral misfit strain of particular ISA with lateral constant a_{ISA} relative to the substrate. Function Δ_{ISA} becomes irresolvable ($R_{ISA} = R_0 - \frac{H}{\tan(\alpha)} = 0$) for:

$$\frac{\epsilon_{ISA}}{\epsilon_{max}} \frac{a_{ISA}}{a_{top}} \to 1 \tag{V.12}$$

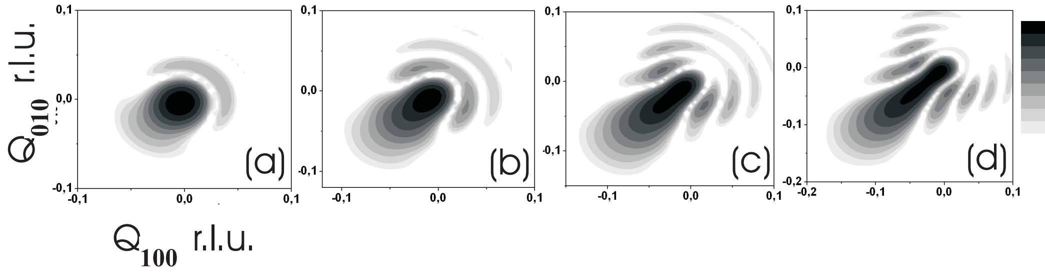

Figure 7: In-plane reciprocal space cuts in the vicinity of the (220) substrate Bragg reflection ($Q_{100} = Q_{010} = 0$ r.l.u.) for LA deformed conical islands (H=70$\AA$, R$_0$=150$\AA$) with island/substrate lattice mismatches ϵ_{max}=-1.7% (a), -3.2% (b), -5.3% (c), and -6.7% (d).

From last equation follows, that for islands with low lattice mismatch ($\epsilon_{max} \rightarrow 0$), the asymptotical broadening effects (for $\epsilon_{ISA} \rightarrow \epsilon_{max}$) on diffraction pattern will appear much earlier, than for structures with larger mismatch.

To visualize this effect, the same island model as in previous section was used to calculate the in-plane diffuse intensity patterns in the vicinity of (220) substrate Bragg reflection. Patterns (Fig. 7) were created for islands gradually deformed using the LA for maximal lateral lattice mismatch ϵ varying from -1.7% up to -6.7%. For a given strain profile, the values of island radius ($\Delta_{ISA}/2$) for particular lattice constants obtained from the patterns in Fig. 7 (scans transversal to the radial direction) are shown as lines in Fig. 8. For the smallest lattice mismatch a discrepancy between estimated and nominal values arises already in the direct vicinity of island base. For largest mismatch the same situation occurs near the top of the island. In a real island structures with high nominal lattice mismatch where interdiffusion of substrate material in the island takes place, the maximum mismatch strain will be reduced. In this case, the influence of the broadening effect increases, and so the uncertainty in the analytically estimated island lateral dimensions also increases.

V.4 Morphology induced changes in island's strain field.

In this section, the sensitivity of the island displacement field to island morphology variations will be analysed. Since only axially-symmetric islands are considered only the deviation of island vertical dimensions relative to its lateral dimensions are significant. For model InAs islands the effect of the height to radius ratio (HRR) on island displacement field was investigated. The main goal was to analyse the specific changes in the island diffuse pattern (Fourier transformation of island strain field).

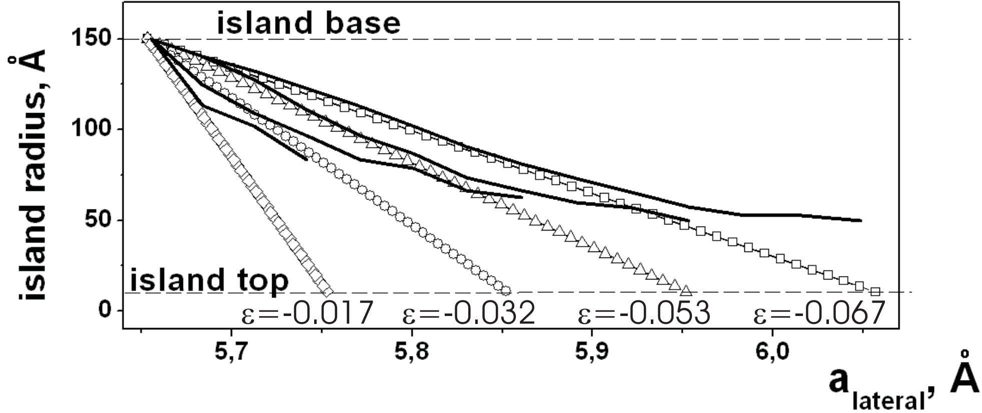

Figure 8: The radius of iso-strain areas with different lateral lattice constant, extracted from the diffraction patterns in Fig 7. (black lines). The nominal radius changes are ♢ (ϵ=-1.7%), ◯ (ϵ=-3.2%), △ (ϵ=-1.7%), and □ (ϵ=-6.7%).

Conical islands with a base radius of 200$\AA$ and ϵ_{max}=-0.067 for the HRR values varying from 0.25 up to 1 (HRR=1 is the upper physical limit for hemi-spherical droplet wetting the substrate) were considered. The distributions of lateral strain components within the vertical island symmetry axis calculated using FEM are shown in Fig. 9. The vertical axis on the plot is given as height over the substrate surface, with negative values corresponding to the underlying substrate material. It can be seen that for different HRR values the lateral strain profile undergoes significant changes. The LA is only satisfied for the model with HRR=0.5 (Fig. 9(b)). For the HRR<0.5 (Fig. 9(a)), the island does not relax completely at the top. For HRR>0.5, a full strain relaxation and further over-relaxation (≈0.2%) occurs. The nature of this effect is complicated and is primarily related to the mechanical solution for the strained cone (wedge) on a flat surface [54]. The mechanical strain energy is proportional to the square of the strain (U∼ ϵ^2) [55]. For ϵ_{max}=-0.067 conditions with HRR>0.5 do not correspond to a minimum energy state. This could be the reason, why islands with HRR above 0.5 are not found in the nature [56].

The in-plane intensity distributions along the radial $\mathbf{Q_{110}}$ direction in the vicinity of the (220) GaAs Bragg point (vertical dashed line on the plot) are shown in Fig. 10. All profiles have been rescaled relative to the maximum intensity. Taking the intensity distribution in Fig. 10(b) as a reference, the effect of underrelaxation (Fig. 10(a)) is very clear. However, the tiny overstrain effect cannot be seen because it is mashed by the finite size induced peak broadening. The peaks in Fig. 10(c,d) arise from the increase in fully relaxed material in the island. In Fig. 11 the out-of-plane diffuse intensity distributions in the vicinity of the (202) GaAs Bragg reflection (Q_{100}= Q_{001}=2.22$\AA^{-1}$, Q_{010}=0, the upper right corner of the plot box) are shown. It can be

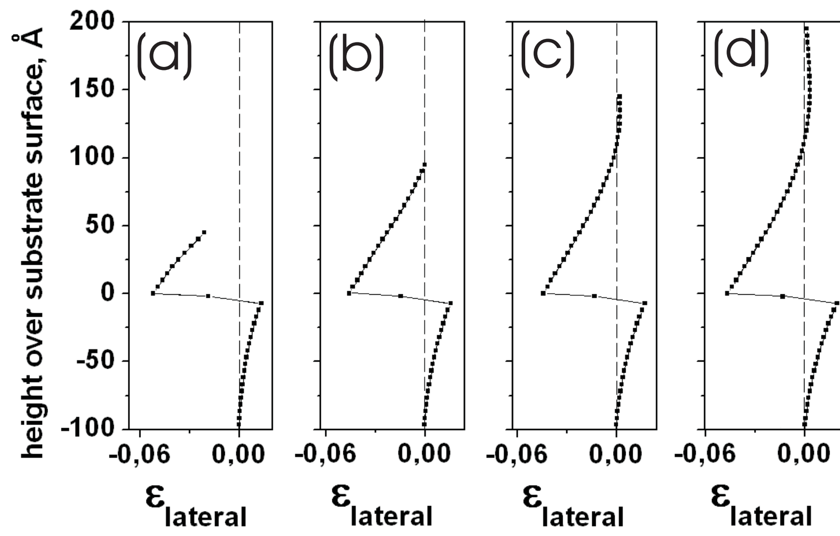

Figure 9: FEM lateral strain profile along the island vertical symmetry axis, for conical InAs island with HRR=0.25 (a), 0.5 (b), 0.75 (c), and 1 (d). The zero-strain position is indicated by the dashed vertical line.

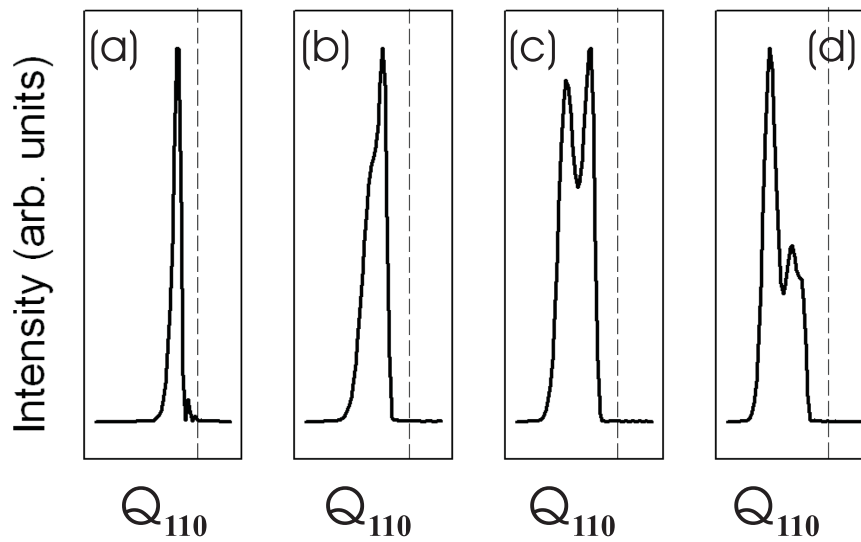

Figure 10: Calculated intensity distribution along the radial Q_{110} direction in the vicinity of the (220) GaAs Bragg position (vertical dashed line) for conical InAs islands with HRR=0.25 (a), 0.5 (b), 0.75 (c), 1 (d).

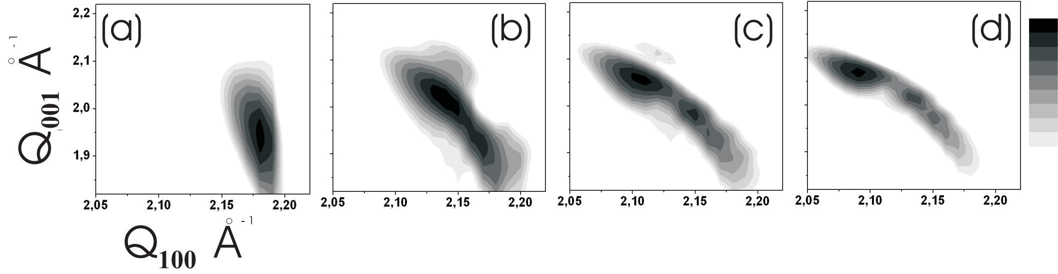

Figure 11: Calculated diffuse intensity patterns in the vicinity of the (202) GaAs Bragg position (Q_{100}= Q_{001}=2.22$\AA^{-1}$, Q_{010}=0) for conical InAs islands with HRR=0.25 (a), 0.5 (b), 0.75 (c), 1 (d).

seen, that with increasing HRR values the intensity in the diffuse intensity pattern shifts gradually towards the position for relaxed bulk InAs ((Q_{100}=Q_{001}=2.07$\AA$)).

The changes in island height to width ratio strongly modify the strain field in the island. The diffuse intensity patterns represent a fingerprints of an island with a specific HRR value.

V.5 Effects of interdiffusion.

In real structures grown at temperatures near 500°C interdiffusion takes place. In this section *homogeneous* and *front diffusion* will be considered: in the first case diffusion leads to the homogeneous intermixing within the whole island volume, in the second case, the diffusion proceeds along the z-axis, creating zones with different concentrations of substrate material.

Homogeneous interdiffusion. For modelling the homogeneous diffusion process, the assumption is made, that the intermixing with the substrate material reduces the island mismatch.

A conical island model with HRR=1 on a GaAs substrate was used for the calculation with nominal In concentrations of C_{In}=1, 0.5, and 0.2. The FEM calculated lateral strain profiles are shown in Fig. 12. The elastic deformation is reduced proportional to the value of C_{Ga}=1-C_{In}. The corresponding calculated out-of-plane diffraction patterns in the vicinity of the (202) GaAs Bragg reflection (upper right corner on the plots) are shown in Fig. 13. Here the diffuse intensity is localized within the relaxation triangles for the corresponding $In_xGa_{1-x}As$ alloy. The relaxation of islands with an arbitrary HRR, composed of a particular $In_xGa_{1-x}As$ alloy is summarized in Fig. 14. Here the lateral strain value at the top of the island is shown for different HRR values. For HRR=0 $\epsilon_{lateral}^{top}$ represents the maximum mismatch strain for a pseudomorphically grown film of the same chemical composition.

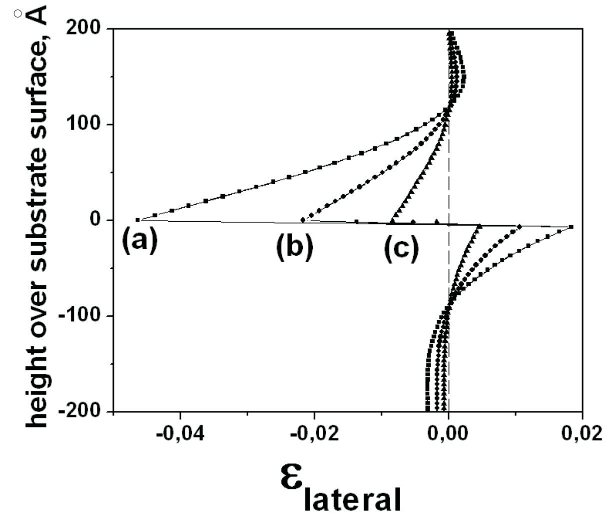

Figure 12: FEM calculated lateral strain profile distribution along the vertical symmetry axis of conical islands (HRR=1) of InAs (a), $In_{0.5}Ga_{0.5}As$ (b), and $In_{0.25}Ga_{0.75}As$ (c) on a GaAs substrate.

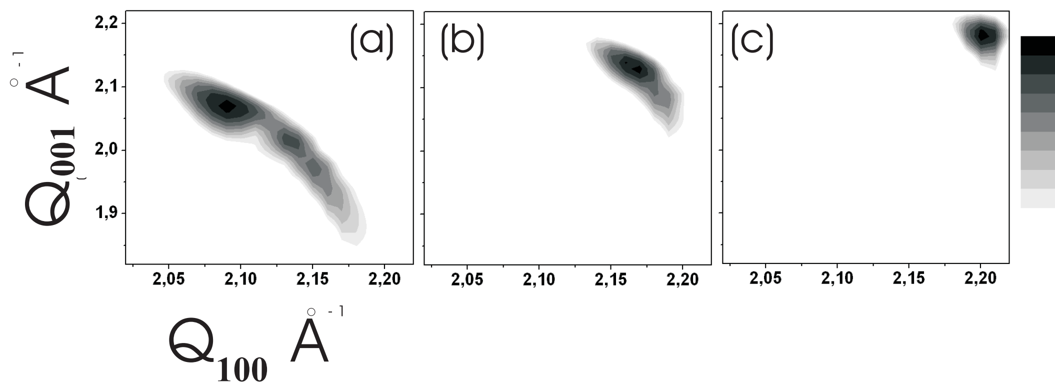

Figure 13: Calculated diffuse intensity patterns in the vicinity of the (202) GaAs Bragg reflection for conical islands (HRR=1) of InAs (a), $In_{0.5}Ga_{0.5}As$ (b), and $In_{0.25}Ga_{0.75}As$ (c).

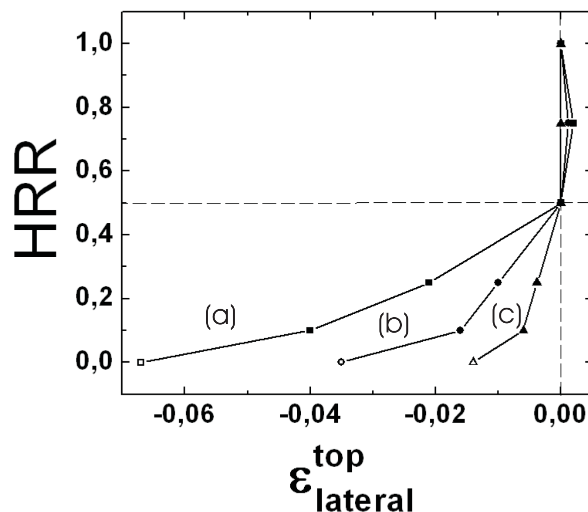

Figure 14: FEM calculated lateral strain values at the top of conical islands with varying HRR of InAs (a), $In_{0.5}Ga_{0.5}As$ (b), and $In_{0.25}Ga_{0.75}As$ (c).

Front diffusion.

A conical island with base radius R_0=200nm and HRR=1 with initial island lateral composition is shown in Fig. 15(a). Figures 15(b, c, d) show simplified island compositions. The calculated diffuse intensity patterns in the vicinity of (220) and (202) GaAs Bragg reflections are shown in Fig. 16. It can be seen, that the simplification of the initial concentration profile with three- or two-layer approximations (Fig. 16(b/f, c/g)) does not significantly modify the strain field in the island. Relative intensity changes occur but the overall shape of pattern remains almost unchanged. However, the diffraction pattern for averaged composed island looks significantly different. It can be concluded that the two-layer approximation represents a reliable simplification for the structural analysis of the islands.

V.6 Finite size effects.

The influence of the island strain field on the diffraction pattern has been discussed under the assumption, that the strain-induced diffraction patterns are sufficiently well localized in reciprocal space.

For small islands size induced broadening effects should be taken into account.

FEM lateral strain profiles were calculated for InAs conical islands on GaAs substrate with HRR=1 and island base dimensions, decreasing from 60nm down to 10nm are shown in Fig. 17. It can be seen, that for islands with equal composition and HRR value, the size reduction only leads to a rescaling of the strain profile. The

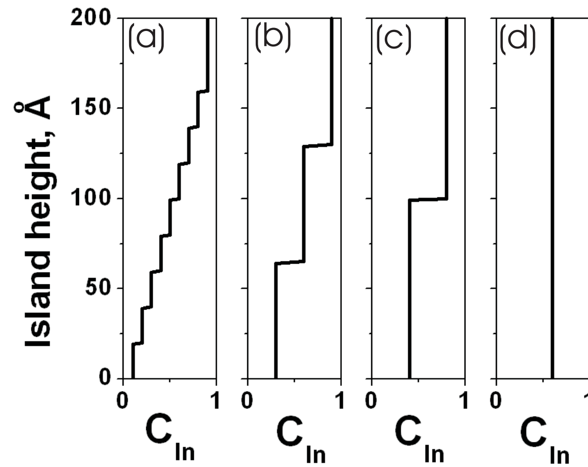

Figure 15: Island with lateral composition profile varying over the island height, with nine zones (a), and approximated by three (b), two (c) zones, and by constant In composition (d).

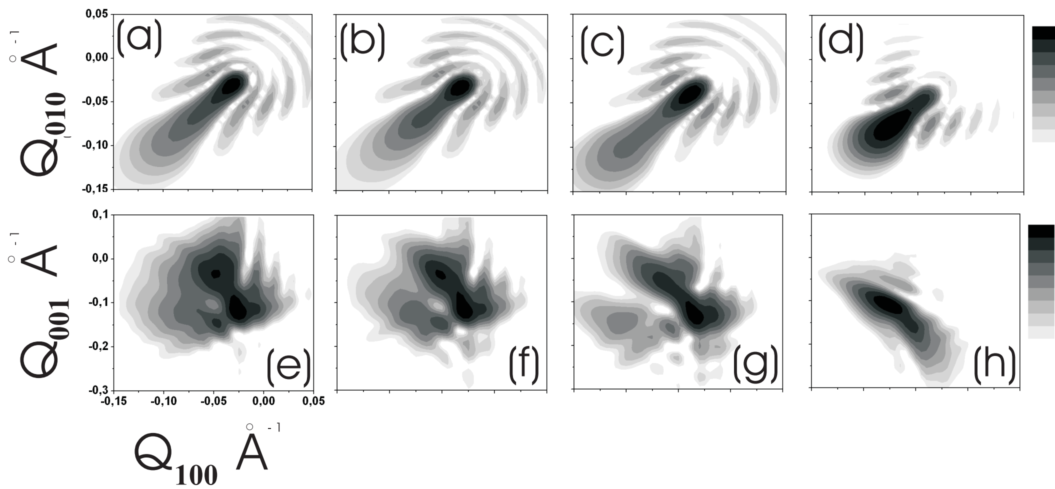

Figure 16: Kinematically calculated diffuse intensity profiles in the vicinities of the (220) (a,b,c,d,) and (202) (e,f,g,h) GaAs Bragg reflections for conical islands (HRR=1) with a composition profile variation along the vertical island axis. Profile with nine layers (a,e), three layers (b,f), two layers (c,g), and by an island model with constant composition (d,h).

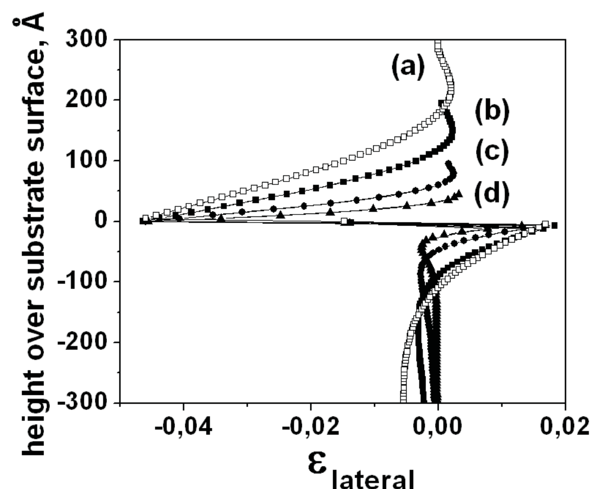

Figure 17: Lateral strain profile distribution along the vertical symmetry axis for conical islands (HRR=1) with lateral size of of 60nm (a), 40nm (b), 20nm (c), and 10nm (d) on GaAs substrate.

calculated diffuse intensity patterns in the vicinity of the primary reflection (out-of-plane GISAX), the (220), and the (202) GaAs Bragg reflections are shown in Fig. 18 and Fig. 19. GISAXS patterns were calculated for an incident angle α=0.2° using the DWBA approximation. The other patterns were calculated using kinematic approximation. In Fig. 18, the Fourier transformed shape function for islands with smaller dimensions are broadened and have reduced intensity. For islands smaller than 20nm (Fig. 18(c)) the shape cannot be any more determined. Size-influenced broadening also strongly affects the strain-induced intensity pattern, when island dimensions are less then 20nm (Fig. 19(b)).

For island sizes below 20nm (Fig. 19(c)) the size-induced effects predominate. For smaller structures (Fig. 19(d)) the diffraction patterns become so broad, that the Fourier pattern of the island strain-field cannot be resolved. The intensity distributions along radial $\mathbf{Q_{110}}$ reciprocal space direction in the vicinity of (220) GaAs Bragg position for all island sizes are shown in Fig. 20.

For sufficiently large islands, the intensity distribution can be correlated with the Fourier transform of island lateral strain field. It can be seen, that for island sizes less then 20nm, this profile is so strongly changed due the size effect, that the strain information cannot be recorded.

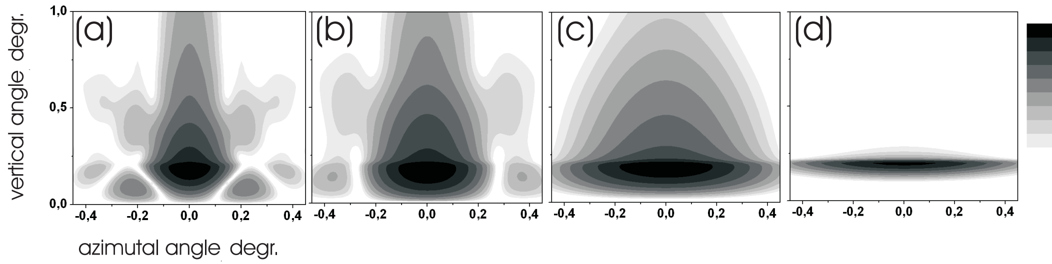

Figure 18: Calculated GISAXS patterns for conical islands (HRR=1) on a GaAs substrate with lateral size of 60nm (a), 40nm (b), 20nm (c), and 10nm (d).

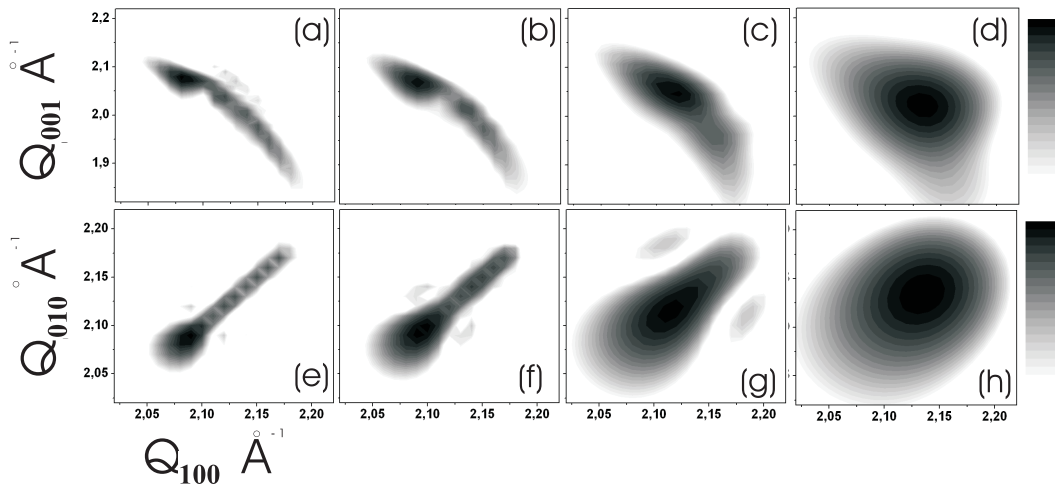

Figure 19: Kinematically calculated diffuse intensity profiles in the vicinities of the (202) (a,b,c,d,) and the (220) (e,f,g,h) GaAs Bragg reflections for conical islands (HRR=1) on a GaAs substrate with lateral size of 60nm (a,e), 40nm (b,f), 20nm (c,g), and 10nm (d,h).

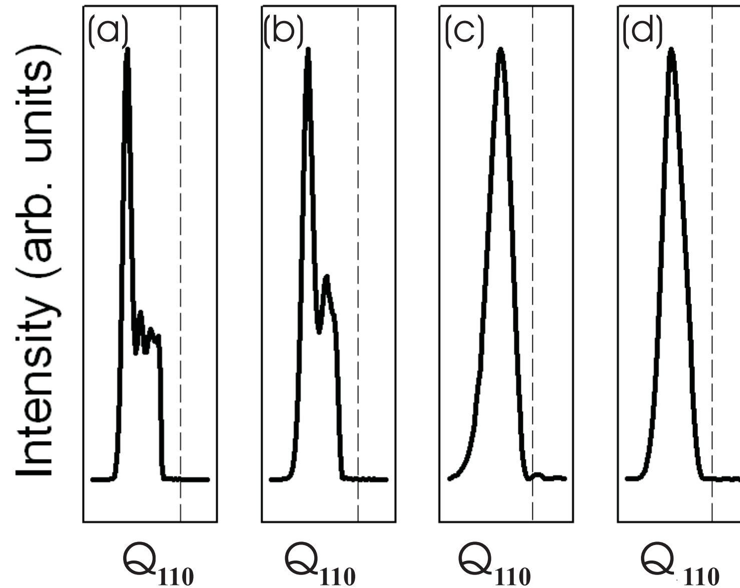

Figure 20: Calculated intensity distribution along the radial Q_{110} direction in the vicinity of the (220) GaAs Bragg position (vertical dashed line) for conical InAs islands with HRR=1 and lateral size of 60nm (a), 40nm (b), 20nm (c), and 10nm (d).

V.7 Conclusions

(!) The limits of applicability of the ISA island model, based on LA deformation approach were investigated. The ISA approximation is sufficient to describe elastic strain relaxation in islands with a lattice mismatch of less than 1% relative to the substrate. In addition, the island HRR should be in the order of 0.5. For smaller and larger HRR value, and large misfit strains the LA deformation model is not applicable.

(!) The applicability of the analytical method for lateral island shape analysis from in-plane Fourier patterns for elastically strained islands with different lattice mismatch were investigated. The method was found to be effective for structures with high lattice mismatch. For low mismatch strains the method was found to yield unreliable results.

(!) The shape of GISAXS patterns was found to be sensitive to changes of the island morphology (island HRR parameter). The effectiveness of GISAXS technique was found to be dependent on the island size. For island sizes below 20nm the technique is not applicable.

(!) The shape of the strain-induced diffuse patterns (in- and out-of-plane) was

found to be sensitive to the island morphology (HRR) and the island chemical composition. It was found, that an arbitrary front diffusion profile in the island can be adequately well approximated by the two layer model.

(!) The condition where the island size does not modify the strain-induced diffraction pattern holds for islands larger then then 20nm. For smaller islands the broadening of the diffuse intensity distribution makes the measurement strain-insensitive.

Chapter VI

Interaction of high-intensity synchrotron radiation with quantum dot samples.

Scientific measurements should record data under reproducible experimental conditions. The prerequisite for reproducible experimental conditions are no or negligible structural changes of the quantum dot samples within the time-period of the experimental investigation. This requirement can be fulfilled only for samples investigated under UHV conditions. Unfortunately, the technological process for the preparation of the quantum dot samples did not enable UHV transfer for all of the samples investigated in this work. Due to this reason only few samples presented in this thesis were measured under UHV conditions.

All other samples were transferred in the air and measured without the uhv-chamber. For such samples the effect of the interaction of high-intensity synchrotron radiation with the quantum dot material should be taken into account. As an example of this interaction, the image of an InAs/AlAs(001) QD sample surface is shown in Fig. 1 after $\approx$24h in air in the GID geometry. The oxide tracks on sample surface marked with arrows correspond to the incoming X-ray beam (10keV) positions. The cause of this effect is the absorption of radiation in the QD-samples that promotes the oxidation of the island sample material. This effect is very significant for the InAs/AlAs(001) island system due to the high reactivity of AlAs. To qualitatively estimate the oxidation damage, two InAs island samples grown on GaAs(001) and AlAs(001) substrates were analysed. In Fig. 2 line scans along the radial $\mathbf{Q_{110}}$ reciprocal space direction near (220) substrate Bragg positions (dashed line) for both samples are shown. The same measurements were done at the beginning (initial) and at the end (end) of a GID experiment. The distributions on the left-hand side of the substrate peak were of main interest, since the intensity is related to the strain field in the islands. The respective intensities were measured by counting on monitor counts and are shown normalized to the intensity values nearest to the substrate. This scal-

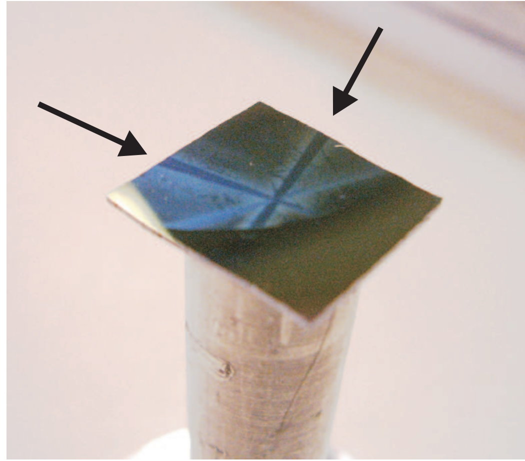

Figure 1: Photograph of a InAs/AlAs(001) sample exposed in air for one day to synchrotron radiation (E=10keV) in GID geometry.

ing is provided to analyse the relative changes of intensity distributions between the initial and final curves. It can be seen, that at the end the signal has decreased for both samples. It represents the change in the quantum dot samples due to oxidation during the measurement period. The relative intensity losses were estimated to be a factor of 4 for dots grown on GaAs(001) and 9 for dots grown on AlAs(001). Hence the affected island volume being correspond to factor of 2 and 3. Interesting, the intensity profile for both samples did not changed after oxidation. This effect will be discussed later (see VIII.3).

From Fig. 2 it can be also seen that in the vicinity of substrate reflection almost no intensity changes for both samples was found. To prove the assumption of negligible structural changes in the substrate material, an AlAs(001) 100nm thick layer pseudomorphically grown on GaAs(001) substrate was investigated [1]. The sample was exposed to the X-ray beam in GID geometry on air and then investigated using XRR[2]. The reflectivity curves for different exposure times are shown in Fig. 3. The first XRR scan measured in a He atmosphere is shown as a solid line. No significant changes in the vertical electron density profile in the AlAs layer are apparent. To avoid oxidation of the quantum dot samples during the X-ray measurement they were kept in a protective He atmosphere (see IV). Fig. 4 shows experimental reciprocal space maps in the vicinity of the (202) AlAs Bragg reflection measured on the same InAs/AlAs(001) quantum dot system in the air and in the He-chamber.The better quality of the map recorded in the He environment is clearly visible.

[1]Due to the high chemical reactivity of AlAs the oxidation effects occur within the shortest possible times.

[2]XRR is sensitive to the changes of layer chemical composition

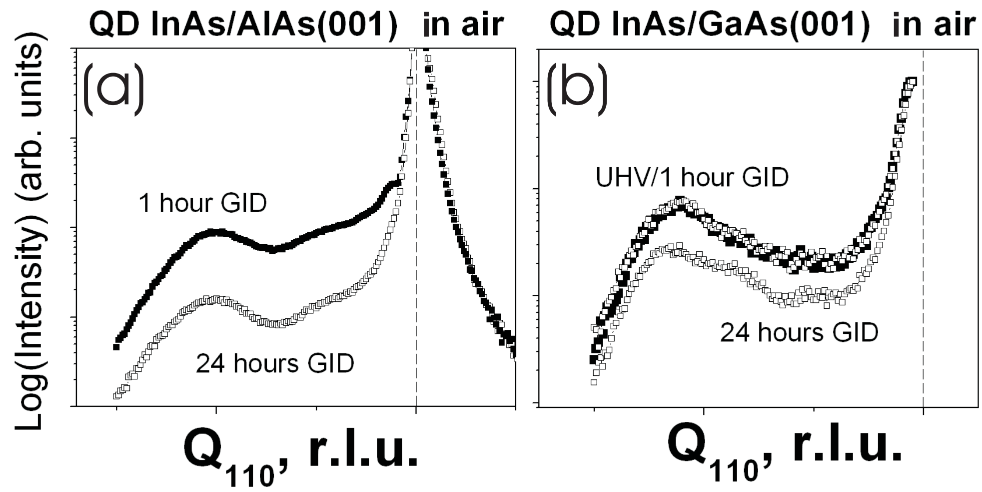

Figure 2: Intensity distribution along the $\mathbf{Q_{110}}$ reciprocal space direction in the vicinity of the (220) AlAs and GaAs substrate reflections (vertical dashed lines) for (a) InAs/AlAs(001) and (b) InAs/GaAs(001) quantum dot samples, exposed to air and to synchrotron radiation (10keV). For sample (b) the UHV-measured intensity profile is given as a reference.

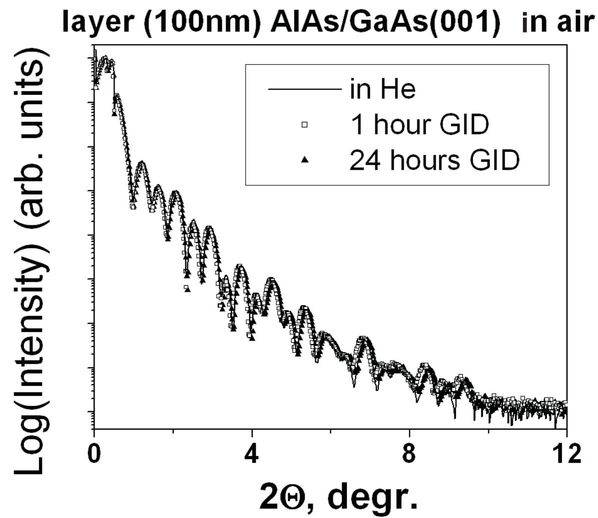

Figure 3: Reflectivity scans for AlAs layer 100nm exposed in air to synchrotron radiation (E=10keV).

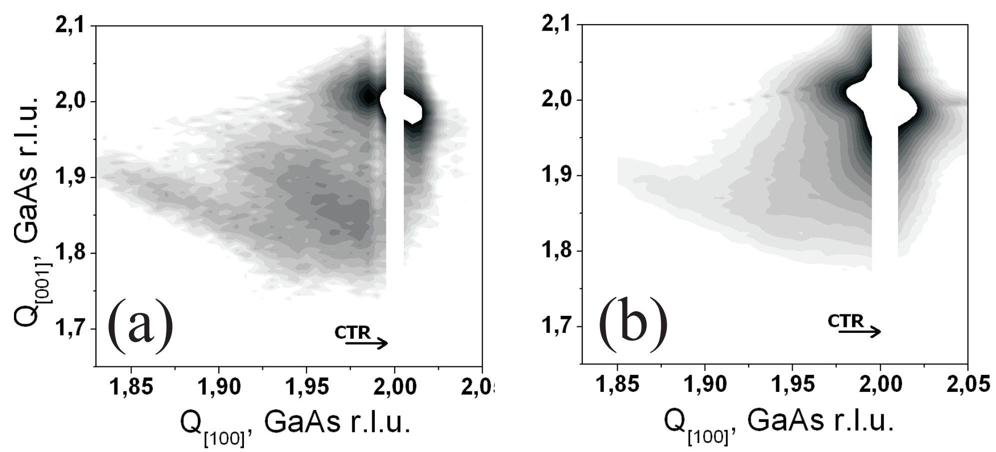

Figure 4: (202)AlAs RSM of the InAs/AlAs(001) quantum dot system measured (a) in He-atmosphere and (b) in air recorded at 10keV.

Chapter VII

Homogeneous islands

Islands grown in the homogeneous growth regime are particularly interesting as building blocks for optical devices exploiting 3D quantum confinement effects. For these application the following requirements have to be fulfilled:

- Reliable control of island size uniformity.
- Precise control of island surface density.
- Knowledge of the chemical composition of the islands.

The sub-micrometer size of the islands limits the techniques available to characterize such systems. At the moment the main tools for determining island distribution and surface density in non-capped systems are imaging techniques such as scanning tunneling microscopy (STM) [99] and atomic force microscopy (AFM) [100]. A disadvantage of these methods is the fact that good resolution can only be achieved over a small area of the sample. In the case of the InAs/GaAs(001) system AFM/STM provide images of relatively good quality but hardly permit an occurate determination of the average island size (island distribution) and the statistically relevant island surface density. For the InAs/AlAs(001) system the island shape analysis is more complicated, because the typical island dimensions are comparable with the resolution of a standard AFM (see IV). Precise analysis is only possible using electron-microscopy techniques.

For comparative analysis of macroscopic samples X-ray techniques have several advantages. Using grazing incidence X-ray methods, such as GID, GIXRD and GISAXS, the main parameters of island system can be determined with high accuracy because the measurements average over sample areas of several square centimeters [112].

VII.1 InAs/GaAs(001) island systems

For our investigations we used three QD samples prepared by MBE-deposition of InAs at 500°C onto GaAs(001) single-crystal wafers [30].The InAs deposition was

Sample	Deposited InAs, ML	ρ_{AFM}, 10^9 cm^{-2}	ρ/ρ_A
A	2.5	9.5	1
B	2.1	6.3	0.66
C	1.8	3.2	0.33

Table VII.1: Comparison of dot surface density values ρ_{AFM} from AFM images for samples A, B and C with different amount of deposited InAs. ρ/ρ_A is the dot density of sample B and C relative to sample A, respectively.

performed at the rate F_{In}=0.2 monolayers (ML) per second and As_4 to In flux ratio F_{As_4}/F_{In} ≈10. The amount of deposited InAs was 2.5 ML (sample A), 2.1 ML (sample B), and 1.8 ML (sample C).

VII.1.1 AFM

The surface topography was analysed using AFM. Large scale topographical images of all three sample surfaces together with FFT images of the same areas (inserts) are shown in Fig. 1(a,c,e). To illustrate the island distribution and size in the appropriate scale, magnified images with height markers are shown in Fig. 1(b,d,f).

They reveal that the dot density ρ increases together with the amount of deposited InAs. The corresponding values are summarized in Table VII.1. The density increases linearly and extrapolates to zero dot density at about 1.5 ML deposited InAs reflecting the amount of InAs in the wetting layer. With RHEED we observe a transition from 2D-growth to dot formation at 1.7 ML. The dot's size does not change within the accuracy of AFM micrographs. The respective average island first neighbor distances of 75nm (A), 95nm (B), and 115nm (C) were determined.

For all three samples islands were found to have approximately equal dimensions, being slightly elongated in [110] direction (vertical direction on the AFM images) ($\frac{W_{110}}{W_{1-10}} \approx 1.25$). Average island dimensions were found to be: island width W≈70±7nm and island height H≈10±1nm, with HRR≈0.3.

From the FFT images in Fig. 1 it can be seen, that for the sample A with the highest island surface density a positional correlation effects between the islands can be resolved. For samples B and C with lower coverage inter-island correlation is not detectable.

VII.1.2 GISAXS

Diffraction experiments were performed in the grazing-incidence geometry at an X-ray photon energy of 9.6keV in the He chamber. For the sample A with the highest island surface density, the experimentally measured out-of-plane GISAXS map in the vicinity of the specular reflection for an incoming beam angle α_i=0.2° is shown in

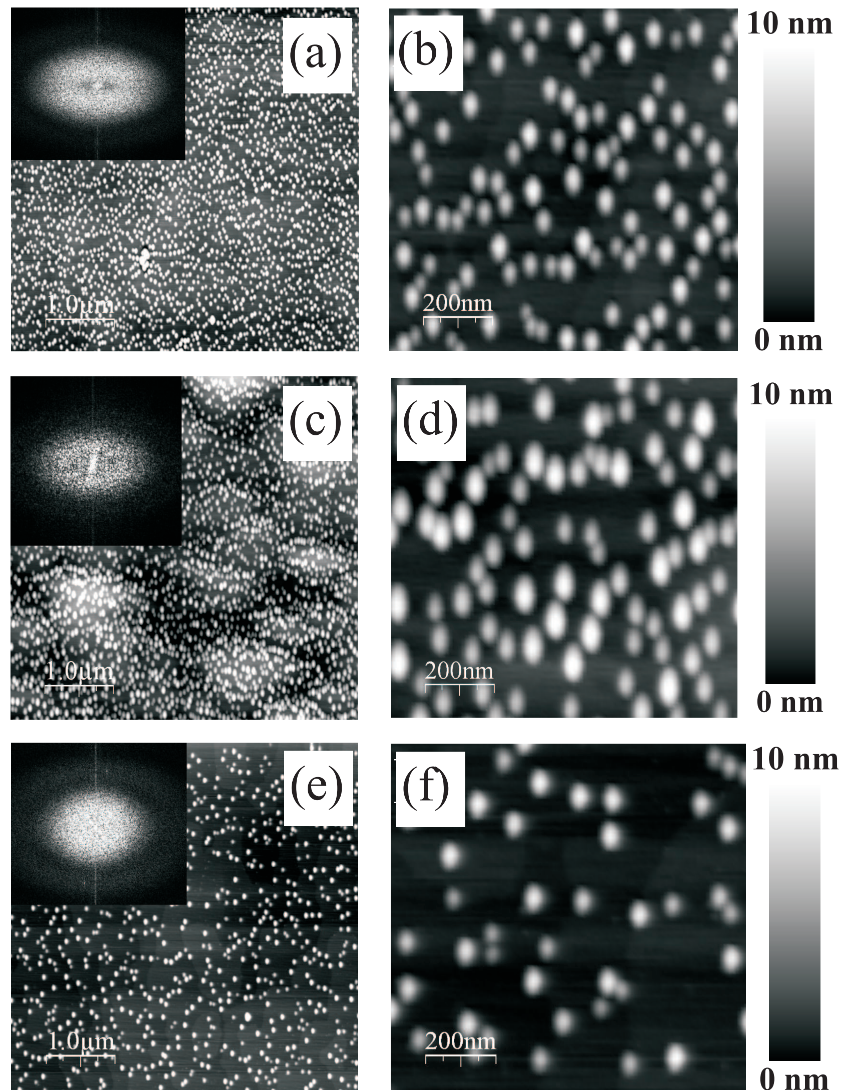

Figure 1: AFM images of samples with different amount of deposited InAs ((a,b) sample A, (c,d) sample B, (e,f) sample C) for surface areas of 25 μm^2 (a,c,e) - inserts are corresponding FFT images - , and 1 μm^2 (b,d,f). The [110] crystallographic direction is towards the top of the page.

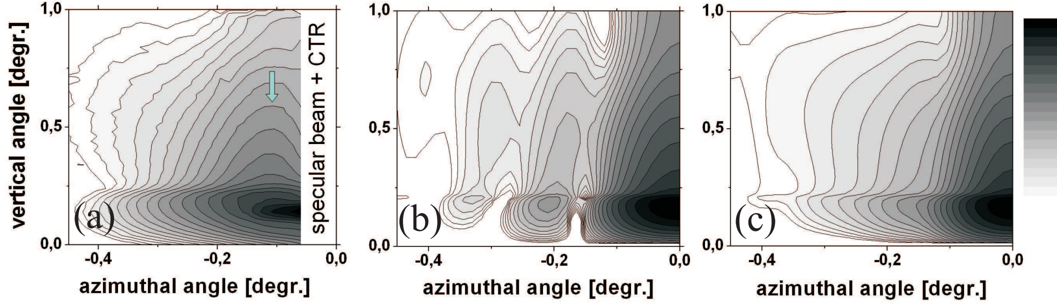

Figure 2: (a) Experimentally measured out-of-plane GISAXS pattern; (b) GISAXS pattern calculated in DWBA for a single island having the experimentally (AFM) determined dimensions; (c) GISAXS pattern calculated for an uncorrelated group of islands with Gaussian size distribution (σ=0.2)

Fig. 2(a). Here the GISAXS-pattern is presented in angular coordinates (vertical angle (α_f) vs. azimuthal in-plane angle). At the vicinity of zero azimuthal angle, the truncation rod (CTR) and specular reflection appear. The Fourier transform of the island shape function calculated using the DWBA for a single island with the AFM-determined dimensions is shown in Fig. 2(b). The island was approximated by a rotational trapezoid with width W, height H, and base angle α. The same calculation done for an uncorrelated Gaussian distribution of islands sizes (σ=0.2), gave the best fit, as shown in Fig. 2(c). The calculated pattern in Fig. 2(c) shows a good agreement with the experimental data. The fit gave an island base angle α ≈30±5°. The calculations for different island widths changes ΔW=20 (island inisotropy) did not significantly change the calculated GISAXS pattern. The intensity maximum of the experimental pattern (Fig. 2(a)) marked by the arrow was found to be unreproducible for non-correlated islands. This peak arises from positional correlation similar to the FFT-pattern in Fig. 1(a). The angular position of the maximum is $\alpha_{azimuth}$=0.1±0.005° and is correlated with the island-neighbor distance d:

$$\frac{2\pi n}{d}{=}k\sin(\alpha) \approx \tfrac{2\pi}{\lambda}\alpha \tag{VII.1}$$

or

$$d \approx \frac{n\lambda}{\alpha} \tag{VII.2}$$

where k is the absolute value of wavevector $\mathbf{k}$, λ is incoming radiation wavelength, and n is the order of the correlation maximum. Assuming that the observed peak is a first-order island correlation peak, from Eq. VII.2 the island short-range correlation length is ≈75±5nm.

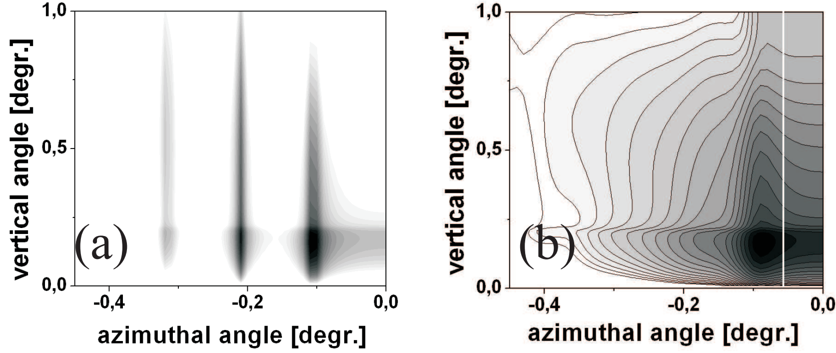

Figure 3: DWBA calculated GISAXS patterns in the case of specially correlated islands with correlation length Λ_{exp} (a,b). Image (a) corresponds to the quasi-periodic array of dots, when image (b) represents a highly distorted para-crystal island ordering. White line represent the border at the right side from which experimental signal cannot be analysed.

To verify the island correlation effect the inter-island correlation length determined experimental GISAXS pattern (Λ_{exp}) was varied as a fit parameter. As a model for island ordering the para- crystal approximation [108],[109] was used [1]. The calculated GISAXS pattern in the case of quasi-ideal island super-lattice [2] with a corresponding correlation length is shown in Fig. 3(a). The same calculation for a strongly distorted para-crystal is shown in Fig. 3(b). It can be seen, that the correlation length Λ_{exp} for the calculated GISAXS pattern is close to the experimental one.

The correlation length Λ_{exp} is an important parameter, which can be used for the analysis of island surface density. However, to make conclusions about the island surface density, knowledge about the correlation length alone is not enough. The short-range nature of the observed correlation peak is the limiting factor. It can lead to the situation, where islands form domains, which have the observed periodicity, but overlap over larger distances [111],[112].Conclusions about island packing density can be made by comparing the average inter-island distance, estimated from AFM images with the island correlation length found from GISAXS. If these values are comparable, the islands cover the surface of a the wafer homogeneously and the inter-island distance can be used to determine the island surface density.

The position of the correlation maximum in the GISAXS pattern was measured by performing azimuthal line scans for fixed α_f=0.4 at different sample rotations around the surface normal, see Fig. 4. Anisotropy in the inter-island correlation distance can be observed: the azimuthal maximum position changes from 0.09° to 0.11° for orthogonal angles giving an anisotropy coefficient of ≈1.2. For highest island surface

[1] approximation of a quasi-periodically distorted lattice of quantum dots
[2] small island super-lattice distortions

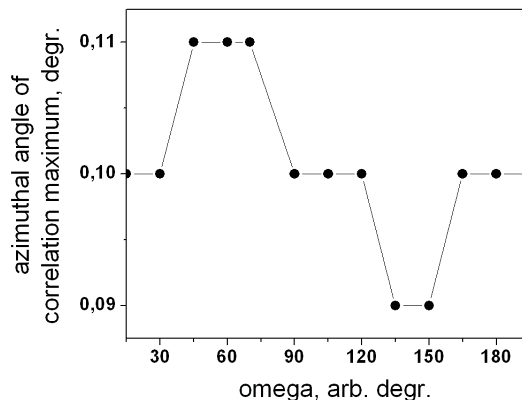

Figure 4: The azimuthal position of GISAXS correlation maximum for different position of the sample (angle omega). 180-degree oscillatory behavior reveals the anisotropy of inter-island correlation length.

densities the inter-island distances are approximately the dimensions (W) of a single island[3]. For sample A the average island dimensions and island correlation distance are almost equal. Furthermore the anisotropy in the correlation length corresponds to the island shape anisotropy coefficient. This means that the islands are so close to each other, that the inter-island correlation distance is modified.It can be concluded that the studied sample A had an island surface density close to maximum.

The experimental background-subtracted GISAXS patterns for samples B and C are presented in Fig. 5(a,c). The GISAXS intensity signal is directly proportional to the number of scatterers (islands). Since all three investigated samples exhibit the presence of equally shaped islands, the GISAXS patterns acquired with infinite measurement times should be identical for all three systems. On the other hand, for limited but comparable measurement times, the GISAXS patterns from the samples B and C will have lower intensities than that measured for sample A. This decrease in the relative intensity should then be directly proportional to the corresponding difference in the island surface densities.

In Fig. 5(b,d) the same patterns as in Fig. 2(c) are shown rescaled proportional to the relative surface density ratios for samples B and C compared to the sample A. For the sample C with island surface density ratio of about 0.33 relative to sample A, the predicted effect can be observed (Fig. 5(c,d). For sample B with surface density ratio of 0.66 the expected effect is not observed. The reasons for the descrepancy can be the bad sensitivity of GISAXS technique as well as the not equal island size distribution or deviations of the actual island surface densities from those determined

[3]Closer packing is energetically unfavourable, since the island induced strained fields in the underlying substrate regions of neighboring islands creates a potential barrier for further coalescence. See III.3.4

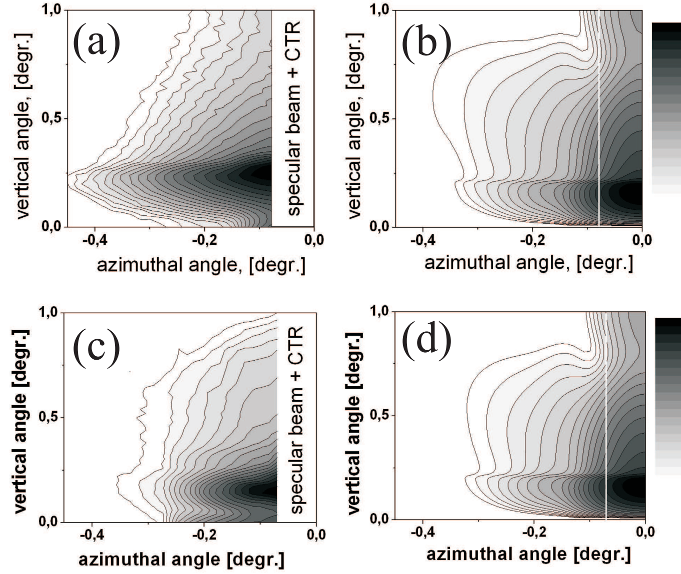

Figure 5: (a,c) experimentally measured and (b,d) DWBA-calculated GISAXS patterns for samples (upper) B and (lower) C.

by AFM. This result is not clearly understood yet.

VII.1.3 GID

Line intensity profiles in radial [110]-directions made in the vicinity of mutually orthogonal (220)-type GaAs Bragg reflections for the sample with the highest island surface density are shown in Fig. 6(a). The intensity distribution contains information about the island lateral strain profile. It can be seen that both intensity profiles are similar which means that the island lateral displacement field is uniform. The island formation process [99] leading to island shape anisotropy [113] observed by AFM, *does not influence* the axial symmetry of the island strain field! The area in the vicinity of the grey arrow is shown in Fig. 6(b). The intensity distributions along [220] and [2-20] directions are shifted in their absolute values to enable their visual analysis. On both curves one can observe a kink on the left side from the GaAs(220)-substrate reflection. These kinks can be associated with island position correlation effects. The position of the kinks marked with arrow in the [110]-directions relative to the substrate is $\approx 0.08 \pm 0.02 \AA^{-1}$, what reveals the inter-island correlation length close to that determined from GISAXS.

To qualitatively explain the effect of island position correlation on the in-plane GID intensity distribution from strained islands, kinematical calculations were made. In Fig. 7(b,c) the diffuse patterns near (220) Bragg GaAs reflection from a single

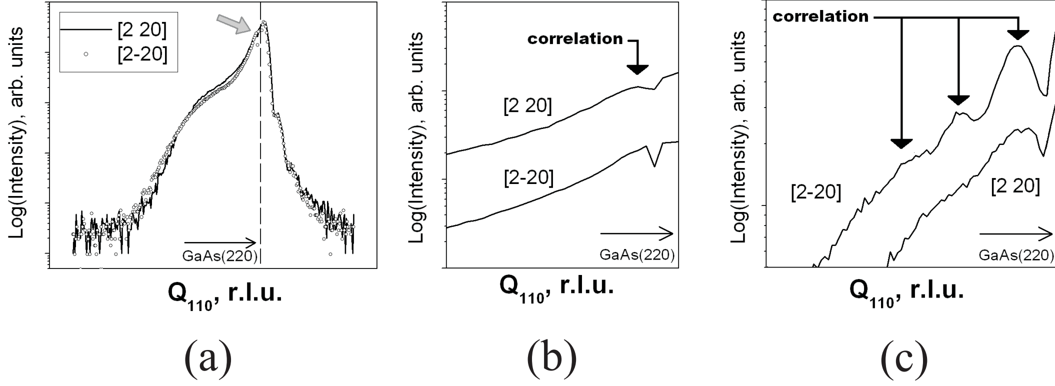

Figure 6: (a) and (b) - Experimentally measured line scans along radial [110] directions in the vicinity of (220)-type orthogonal GaAs Bragg reflections. (b) The enlarged-scale plot of the area indicated by the grey arrow in plot (a). (c) Same line scan for a different sample.

InAs island (Fig. 7(a)) with a linearly changing lateral strain field (see II.11.3) are modulated due to the influence of the 2D periodic island arrangement. In Fig. 7(b) the domain size of the periodic 2D island super crystal is much larger than the unit cell creating fine 2D intensity modulation of the initial pattern. The periodicity of the modulation parallel to each of the main reciprocal space directions is $2\pi/a$, where a is the inter-island distance. Such modulations were experimentally detected for long-range periodic arrays of Ge/Si(001) quantum dots investigated at synchrotron beamlines with high spatial coherence [45]. If the size of the periodicity domain becomes comparable to the unit cell (short-range effects) the pattern becomes sensitive to the periodicity only along the mainly probed crystallographic direction. For the [110] direction, see Fig. 7(c), this intensity modulation corresponds to the short-range inter-island periodicity along $a_{[110]}$. For a para-crystal island arrangement the periodic pattern in Fig. 7(c) will diminish until only weak short-order modulations close to the substrate position will be present. The determination of the correlation maximum position with in-plane GID line scans can be a useful method for investigation of island surface arrangement. As an example, the results in Fig. 6(c) from different island sample, revealed pronounced short-range periodicity of islands (especially in [1-10] crystallographic direction).

In Fig. 8 the GID in-plane and HRXRD out-of-plane reciprocal space maps in the vicinity of (220) and (202) GaAs Bragg reflections are shown for all samples. The acquisition times for the in-plane and out-of-plane plots were comparable. The background signals on the plots are cut off. All in-plane and out-of-plane plots have a common maximum limit, respectively.

The diffuse intensity part around Bragg reflections in Fig. 8 is associated with

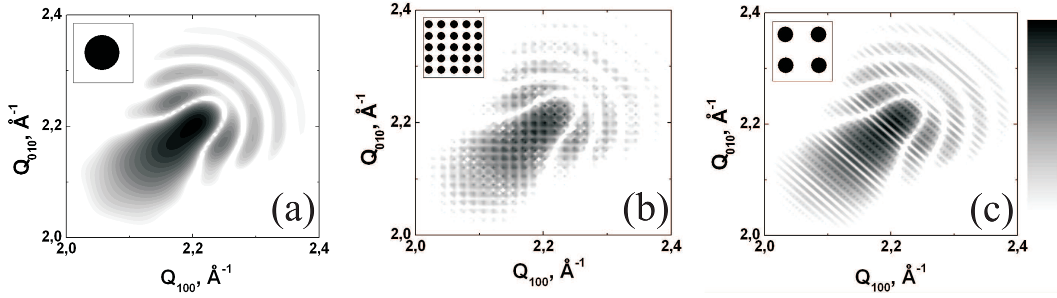

Figure 7: (a) Calculated in-plane map in the vicinity of (220) GaAs Bragg reflection (Q_x=Q_y=$2.222\mathring{A}^{-1}$) for single linearly deformed InAs island. (b) Same calculation for a periodic arrangement of equal islands with superlattice domain size much larger than the superlattice unit cell. (c) Same calculation for a periodic arrangement of equal islands with superlattice domain size equal to the superlattice unit cell.

the elastic distortions in our SK-quantum dot structures except the region close to the Bragg spot, where the substrate signal contributes [72]. The intensity pattern in the very vicinity of Bragg points mainly stems from the strain field in the deformed substrate region directly beneath the dots. The relative intensity decrease of the diffuse patterns qualitatively reflects the decrease of the total amount of scattering QD volume from sample A towards sample C.

In Fig. 8 it can be also seen that for all investigated samples the diffuse patterns are almost equal. The almost equal broadening of the in-plane diffuse part in direction transversal to $Q_{[110]}$ for all samples also reveals their average dot size distributions to remain unchanged within the whole investigated range of deposited InAs.

These findings are in good correspondence with the observations in Fig. 1 that the total deposited InAs volume solely increases the dot surface density. The equality of the diffuse patterns for both reciprocal space projections points to the equal 3-dimensional strain field in the investigated QD systems, and thus, to their equal average chemical composition.

In order to corroborate our findings, line scans in radial [110] reciprocal space direction through the (220) GaAs Bragg reflection ($Q_{[110]}=2 \cdot\sqrt{2}$ GaAs r.l.u.) are shown in Fig. 9. To enable their comparison, all presented line scans were done under equal measurement conditions. In Fig. 9 the intensity shoulder to the left of the (220) GaAs Bragg reflection is related to the strain field in the investigated QDs. It can be observed within the region marked by dashed lines that with decrease of dot surface density the dot related intensity distribution rescales without changing its shape. To the left of the marked region the background noise disturbs the comparison, to the right substrate strain and inter-dot correlation effects, that scale differently with density, add to the signal. We conclude that the QD composition is independent on the deposited InAs volume at the growth conditions applied.

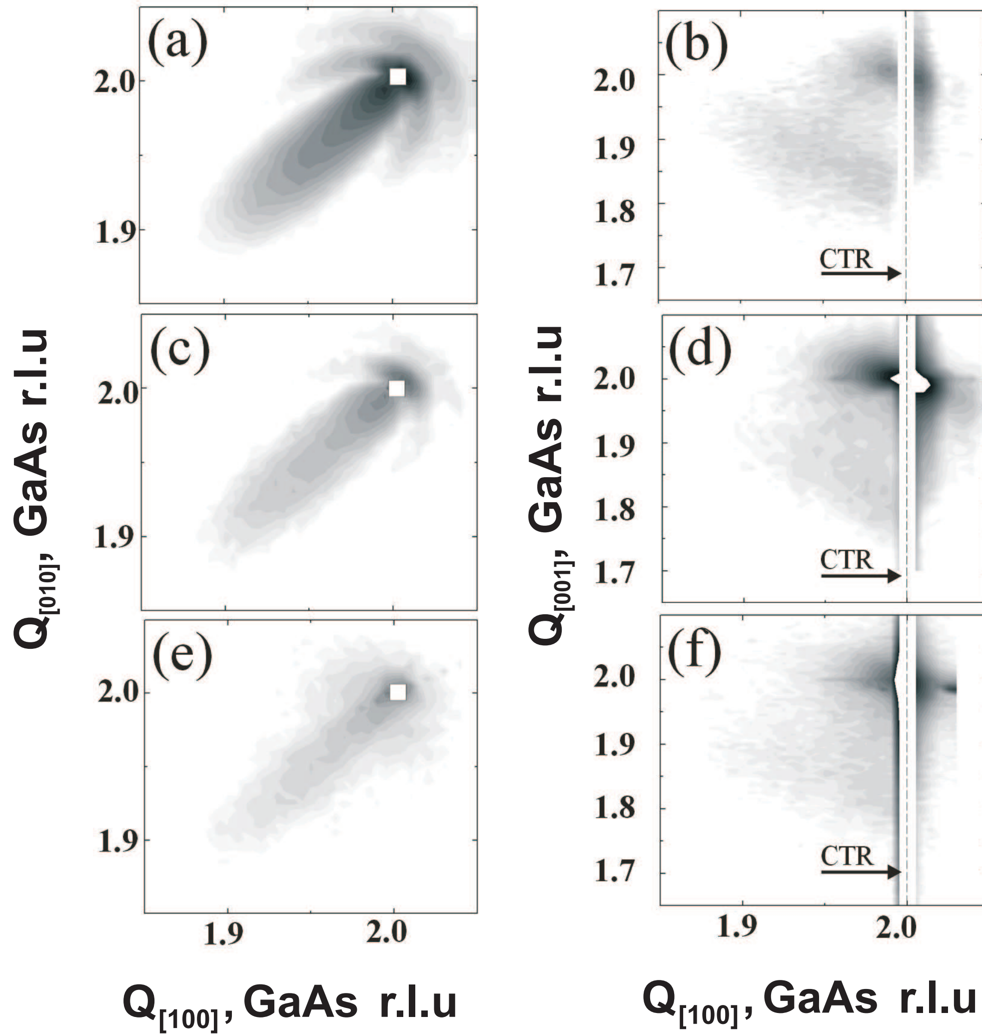

Figure 8: Experimental reciprocal space maps in the vicinity of the (220) GaAs Bragg reflection (a,c,e), and the (202) GaAs Bragg reflection (b,d,f) for samples A (a,b), B (c,d), and C (e,f). The substrate Bragg peaks have coordinates $Q_x = Q_y = 2$ r.l.u. (in-plane) and $Q_x = Q_z = 2$ r.l.u. (out-of-plane) (1 GaAs r.l.u.=$1.11 \AA^{-1}$).

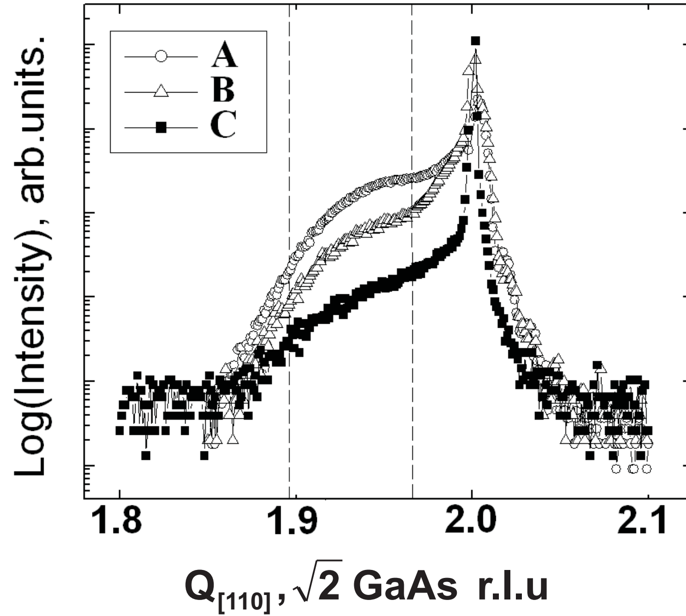

Figure 9: Line scans along the radial [110] direction in the vicinity of the (220) GaAs Bragg reflection for samples A, B, and C. Vertical dashed lines mark the region used for comparison of the dot compositions.

One may expect that the discussed relative intensity differences also quantitatively correspond to the relative changes of the dot surface densities [73]. However, the ratio of the diffraction signals from samples B and C relative to A do not reflect the AFM values in Table VII.1. Assuming a linear relation between the dot density and the diffraction intensity in the marked region of Fig. 9 we would derive the ratios $\rho/\rho_A^{GID} \approx 0.33$ and $\rho/\rho_A^{GID} \approx 0.05$ for sample B and C, respectively. So far this discrepancy is not understood.

VII.1.4 Island composition analysis

The chemical composition of the islands was investigated in different ways. The FEM was used to determine the island shape and composition using an interative modelling procedure. The experimental X-ray diffraction techniques (II.11.3, V.3) were used for the comparison. In the FEM method the strain field in the QD is numerically computed using the thermo-elasticity approach [72]. The extracted strain was then used to calculate the corresponding diffuse intensity distribution in reciprocal space in a kinematical approximation. The obtained distribution was compared to the experimental pattern of sample A. Parameters were adjusted in an iterative procedure to best describe the experimental X-ray data. The calculated reciprocal space maps giving the best correspondence to the experiment are shown

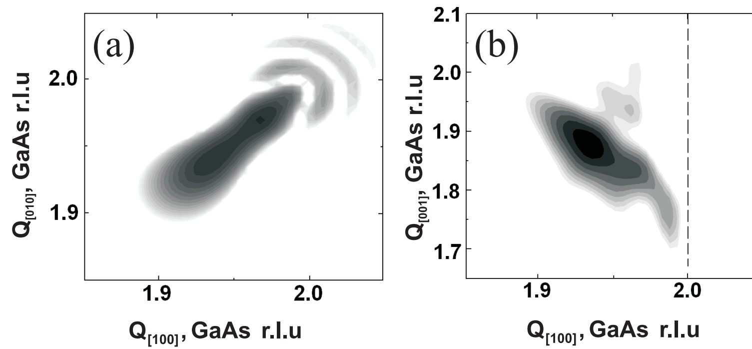

Figure 10: Best corresponding calculated (a) in-plane and (b) out-of-plane diffuse intensity distributions for elastically strained QD model (Fig. 12).

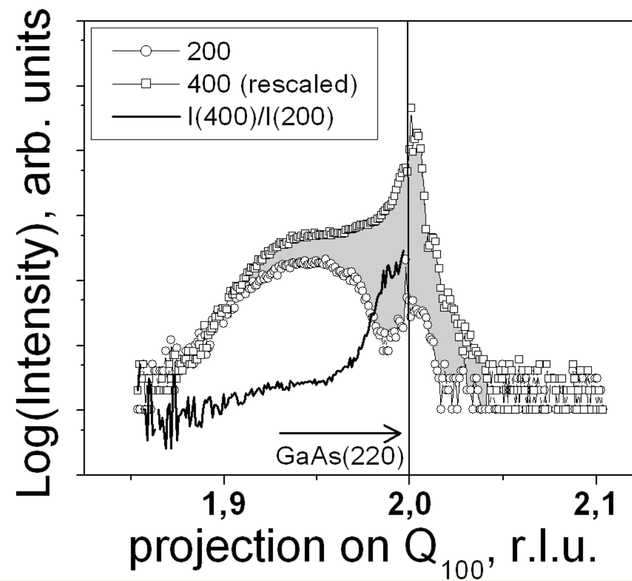

Figure 11: Line scans along the [100] direction in the vicinity of the (400) (squares) and the (200) (circles) GaAs Bragg reflections (marked by the vertical line). The (400) reflection was rescaled to fit the (200)-coordinates. The I(400)/I(200) intensity ratio is given by the black solid line.

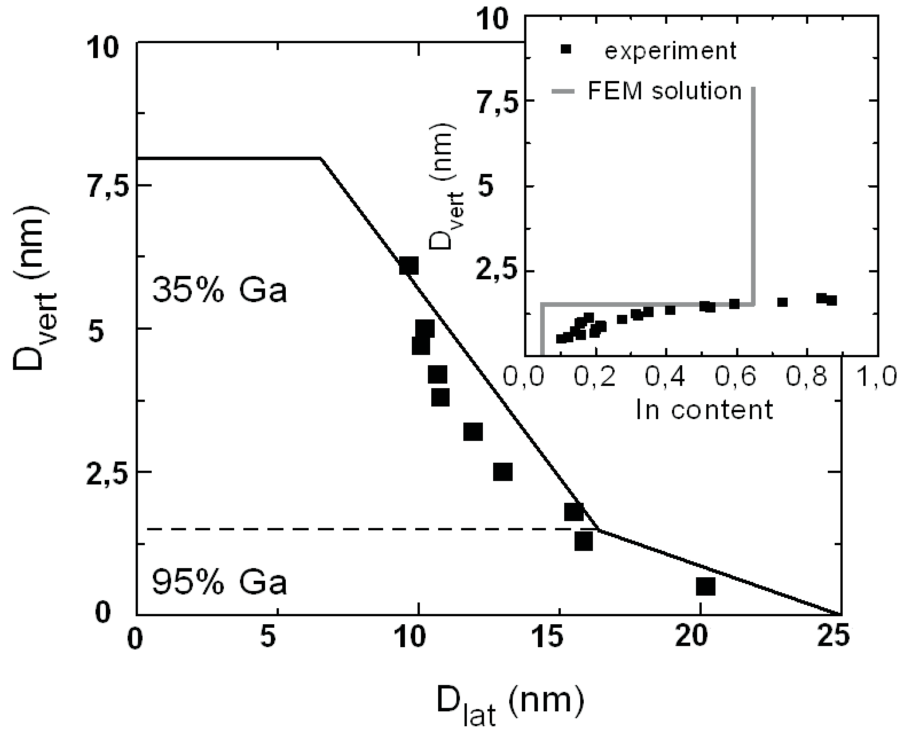

Figure 12: Height dependence (D_{vert}) of the lateral dot extend (D_{lat}) reflecting the geometry of half the central cross-section through the axially symmetric dot. The straight line displays the dot geometry assumed in the FEM based results of Fig. 10. The data points displayed by squares are obtained from experiment by the iso-strain method [58]. The dashed line separates the dot into two parts of different In content. The straight line in the inset displays the height dependence of the In content used for our diffraction intensity maps in Fig. 10. Squares denote data obtained from experiment.

in Fig. 10.

The dot geometry assumed for the results in Fig. 10 is displayed by the straight line in Fig. 12. The assumed dot geometry is in good correspondence with experimental data directly obtained from the in-plane reciprocal space map within the iso-strain model [58]. Corresponding data points are marked by squares in Fig. 12. The thus obtained lateral QD dimensions are approximately 20% smaller than those estimated by AFM. This discrepancy we attribute to the instrumental uncertainty associated with the finite AFM-tip size. For the calculations a dot height of 8 nm was assumed in agreement with AFM data (10nm) if a 2nm thick oxide is taken into account VIII [115].

Furthermore, as can be noted in Fig. 12 we assume the dot to be divided into

two sections having different chemical compositions. The first 1.5nm of the dot base are assumed to be of high Ga-content as a result of strong intermixing of Ga atoms from the substrate. Also this assumption can be corroborated by experimental data comparing the diffraction intensities in the dot-related foothills of the (200) and (400) Bragg spots, Fig. 11, since the ratio of corresponding intensities depends on the group III content of the dots [58]. The corresponding data are marked by squares in the inset of Fig. 12. We note that due to the reduced scattering volume of the dot tips and the decreasing difference of the intensities in the corresponding reciprocal space area the measurement uncertainty of the data points strongly increases with the height in the dot. Data for higher zones in the dots yield unphysical In concentration values and thus are not shown. We, therefore, just regard the experimental data points as a motivation to divide the dot into two regimes of different In-content: a base of high Ga-content and the rest having much lower Ga content. The absolute numbers have then been adjusted to best describe our experimental reciprocal space maps by the FEM based calculations. The best fit is obtained assuming a low In content of only 5% in the base and 65% in the rest of the dot.

From the composition profile and island volume the mean InAs content in island can be estimated. It is close to 50% which is similar to that from cross-section HRTEM images of InAs/GaAs(001) islands [116]. For a given chemical composition and volume of the average island, and the island surface density, the amount of InAs material V^{InAs} incorporated in the wetting layer can be extracted. The atual wetting layer thickness can then be estimated using the equation $h=V^{InAs}/(S\cdot C)$ where S is the unit surface area, and C is the In content in the wetting layer. The amount of pure InAs incorporated in the quantum dots was found to be equivalent to a layer with thickness $t\approx0.3$nm. For 2.5 ML deposedted the InAs volume incorporated in wetting layer was around 1.7 ML or ≈0.5nm. This value does not contradict with the InAs fraction (>0.3 ML^{InAs}) for wetting layer formation in InAs/GaAs(001) island system estimated from STM observations [32]. Assuming the wetting layer composition to be close to that of the island base, the corresponding wetting thickness should be about 10nm or ≈30 ML. Taking into account the small lattice mismatch strain for a Ga-rich alloy in the wetting layer ($<1\%$), this result correlates well with theoretical calculations of the critical WL perturbation thickness amplitude [117]. The wetting layer does not have to be homogeneous. TEM investigations show, that even for buried island systems the uppermost part of the wetting layer around the islands remains In rich [118]. In such situation, the wetting layer thickness can be overestimated by more than 50%. For example, for islands grown at 400°C the WL thickness is 4 ML^{InAs} [114]. For the investigated quantum dot system grown at 500°C the wetting layer thickness of 10-15 ML logically correlates with [114].

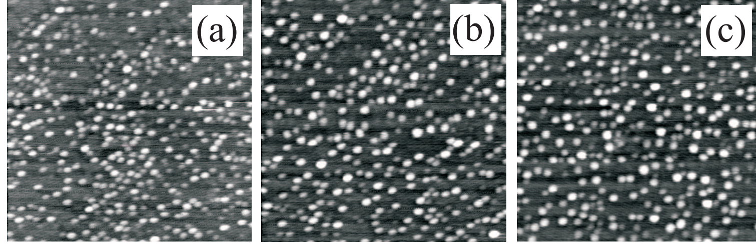

Figure 13: AFM images ($1\mu m^2$) of an AlAs(001) surface after deposition of 2ML (a), 2.2ML (b), and 2.4ML (c) of InAs at temperature T=535°C.

VII.2 InAs/AlAs(001) island systems

Within the homogeneous growth regime the variations of island surface density for InAs/AlAs(001) system are minimal [33]. The island volume increases continuously from initial island formation up to the start of the coalescence regime with increasing amount of deposited InAs (see Fig. 13). This means that for the InAs/AlAs(001) precise determination of the island surface density requires very high sensitivity. To detect tiny surface density differences the inter-island correlation effects can be exploited. For InAs/AlAs(001) systems the island surface density is always high so it should be possible to observe island position correlation effects. In addition, the higher surface density of islands compared to that for InAs/GaAs(001) should improve the scattered intensity. For densely packed island systems the inter-island distance becomes sensitive to the variations in the average island dimensions, which means that variations in the measured correlation length will reveal variations in the island surface density.

To illustrate the sensitivity to the correlation effects in InAs/AlAs(001), the GISAXS pattern measured for a InAs/AlAs(001) sample grown under 500°C is shown in Fig. 14(a). The first-order correlation maxima is clearly resolved giving a short-range inter-island distance of 32±1nm. For the known average island lateral dimensions the calculated GISAXS pattern is shown in Fig. 14(b)). Including the measured inter-island correlation distance gives the modified calculated GISAXS pattern in Fig. 14(c). This pattern agrees with the experimentally measured intensity distribution.

VII.3 Conclusions

To conclude, InAs/GaAs(001) QD's grown with different amount of deposited InAs were studied.

It was found that under the investigated deposition conditions the average dot chemical composition is independent on the amount of deposited InAs. Furthermore,

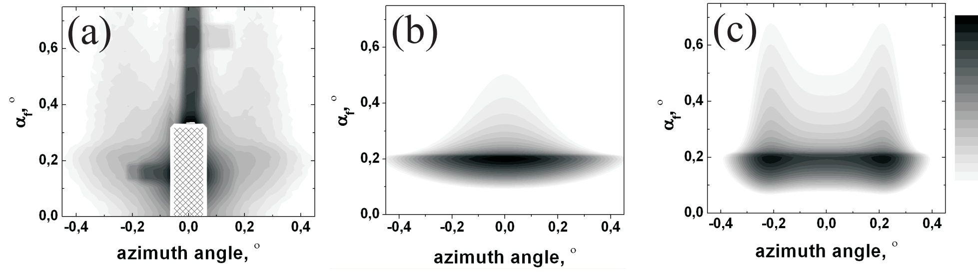

Figure 14: (a) Experimental out-of-plane GISAXS pattern. The marked area with specular reflection was not measured. (b) Calculated GISAXS pattern for single InAs island with width W=30nm. (c) Calculation for same island under influence of island spatial correlation (Λ_{corr}=32nm).

the increase of deposited InAs primarily leads to a proportional increase of the dot surface density while the dot size distribution remains unchanged. The GISAXS and GID was applied to analyse the island positional correlation and to approve the conservation of island size distribution. The average composition of the investigated SK-QDs was found to be close to $In_{0.5}Ga_{0.5}As$. The results establish that the QD size and in particular the QD composition do not depend on the instant of QD formation. This finding indicates that once the critical QD size is reached growth of the particular QD stops. Also, the rate at which substrate material intermixes into the QDs is significant only during the QD formation process and stops once the dot is completed. Furthermore, the intermixing rate does not depend on the instant at which a particular QD starts to form. These findings are important for a better understanding of the nature of the quantum dot intermixing process and its influence on the dot formation.

For InAs/AlAs(001) system the idea about surface density analysis using island positional correlation effects was developed.

Chapter VIII

Investigation of island formation mechanisms

Islands systems prepared in the coalescence regime (see I) are not of great technological interest since their island size non-uniformity. Theoretical studies [84] and experimental observations [28] have shown that the formation of conglomerates of InAs material leads to plastic relaxation due to dislocation formation at the island/substrate interface. Dislocated interfaces form deep traps and non-radiative recombination centers which are undesirable in quantum-dot based optical devices. These systems can be useful for understanding the mechanisms driving island formation.

The main processes controlling island formation in the SK-growth mode are the temperature dependent surface diffusion of deposited InAs and the bulk diffusion of substrate material into the growing island, see Fig. 1(a). Temperature dependent InAs desorption should also be taken into account since it modifies the amount of InAs available. On reaching coalescence stage based on the given material supply model the island system "replies" that under these particular thermo-dynamic conditions it does not need InAs material for the formation of homogeneous islands. The unused InAs is then stored in large conglomerates. The mutual material distribution in such "over-saturated" system is illustrated in Fig. 1(b). Maintaining the constant amount of deposited material on the substrate surface (negligible effect of the process "2" in Fig. 1(a)) and varying only one of the deposition parameters, say substrate temperature, one can analyse the influence of this parameter on the growth process of homogeneous islands by measuring the changes in the distribution of material within the given transport chain. Based on these measurements conclusion about the island formation mechanism can be made. The relative changes of unused InAs volume relative to the volume of elastically strained islands is needed as an indicator of the amount of InAs needed for strained island/wetting layer formation. For such investigation the knowledge of island composition is obligatory. The use of X-ray diffraction with high intensity synchrotron radiation together with FEM-based modelling of diffuse diffraction patterns can yield the required information.

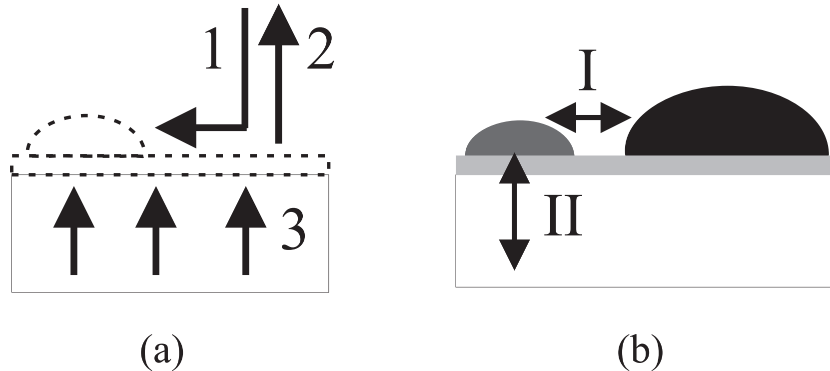

Figure 1: (a) Channels for material supply to islands growing in SK mode: 1- deposited InAs, 2 - desorbed InAs, 3 - interdiffusion of substrate material. (b) Material redistribution for SK-islands in the coalescence regime: I - InAs redistribution between homogeneous islands and InAs conglomerates, II - redistribution of substrate material in the homogeneous islands and the wetting layer.

VIII.1 Investigation of temperature dependent island growth mechanism in InAs/GaAs(001) system

Three InAs/GaAs(001) samles grown at 480°C , 500°C, and 530°C with an InAs deposition rate of 0.04ML/sec were investigated. During MBE growth the volume of InAs deposited was kept constant at 2.7ML (accounted for desorption) which corresponds to the moment of island coalescence.

"Differential mode" AFM images of the samples are shown in Fig. 2. X-ray diffraction measurements were performed on all three samples as described individually for each sample in the following subsections.

VIII.1.1 Structure analysis of islands grown at 530°C

For the sample grown at 530°C the line scan in the radial [110] direction through the (220) GaAs Bragg reflection is shown in a logarithmic intensity scale in Fig. 3(a). For comparison with the 2D maps, the projection of the $Q_{[110]}$ reciprocal lattice vector on the $Q_{[100]}$ axis are used for the horizontal scale. Three different intensity distributions can be observed. First, the strong substrate reflection at Q_{100}=2 r.l.u. marked by "I". Second, the broad intensity distribution (II) starting at the substrate position and decreasing towards smaller Q values corresponds to the signal from the elastically strained quantum dots (see VII). Peak (III) with a broad maximum near Q_{100}=1.89 r.l.u. was not observed for samples grown in the homogeneous stage, so, it presum-

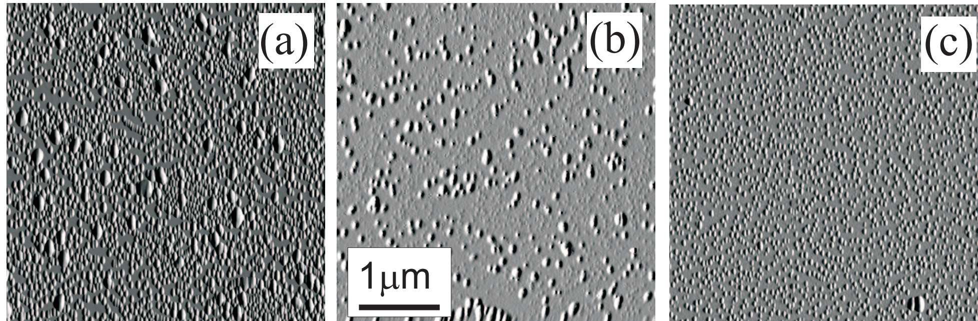

Figure 2: Topographical surface AFM images ($25\mu m^2$) of InAs(2.7ML)/GaAs(001) island systems grown at 480°C (a), 500°C (b), and 530°C (c).

ably corresponds to the conglomerates formed in the coalescence stage. Theoretical calculations (chapter V) have revealed this intensity profile for strained islands with a height to radius ratio (HRR) close to 1. The topographic analysis of the experimental AFM-data gave average HRR value of 0.4. The large discrepancy between the expected and measured HRR values is indicative of non-elastic strain relaxation (chapter V) [107]. The intensity distributions along the [100] direction through the (400) and (200) GaAs Bragg reflections measured under the same experimental conditions are shown in Fig. 3(b). It can be seen that for region III the intensity for both reflections is equal again indicating that the composition of the relaxed island conglomerates is close to that of pure InAs. The intensity of the (200)-signal for the region II is strongly diminished indicating that a high Ga content is present in the elastically strained islands.

The experimental in-plane and out-of-plane diffuse X-ray diffraction patterns measured in the vicinity of the (220) and (202) GaAs Bragg reflections are presented as contour plots in Fig. 4(a,c). In the 2D in-plane plot the peaks from the strained and plastically relaxed islands can be easily distinguished. The out-of-plane plot only has intensity in the region arising from elastically strained dots. The lack of signal from the relaxed islands is probably due to the lower sensitivity in the out-of-plane geometry (typically a factor of 10). This is expected because the AFM image Fig. 2(c) shows a low density of relaxed conglomerates. Direct methods were used (see VII) to provide the sufficient structural information for building a reliable initial FEM model of the elastically strained islands. The iterative procedure was used to modify the FEM model until the calculated diffuse diffraction pattern agreed with the experiment data as shown in Fig. 4(b,d). The best fit model revealed the presence of two zones within the strained islands with composition of $In_{0.05}Ga_{0.95}As$ (island base) and $In_{0.3}Ga_{0.7}As$ (island top) and the average island composition was $In_{0.2}Ga_{0.8}As$.

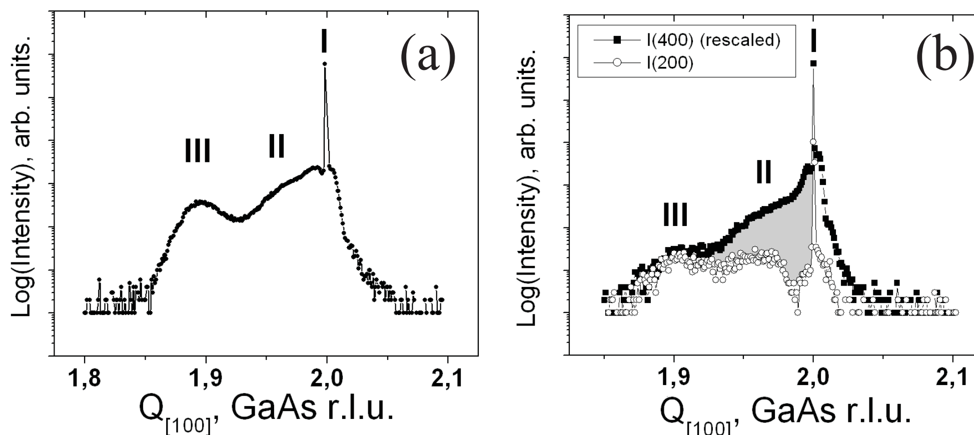

Figure 3: Experimentally extracted intensity profile along radial [110] reciprocal space direction through the (220) GaAs Bragg reflection (a), and intensity profiles along [100] reciprocal space direction through the (400) and (200) GaAs Bragg peaks (b). I - substrate peak, II - signal from elastically strained islands, III - signal from plastically relaxed island conglomerates.

VIII.1.2 Structure analysis of islands grown at 500°C

The X-ray experiments on the sample grown at 500°C were realized under ultra high vacuum conditions. The line scan in the radial [110] direction through the (220) GaAs Bragg reflection is shown on a logarithmic intensity scale in Fig. 5(a). As for the previous sample, there are three contributions to the intensity profile. First, there is more plastically relaxed material on the surface, resulting in a higher integrated intensity of (III) compared to the elastically strained islands (II). The chemical composition analysis (Fig. 5(b)) revealed that the plastically relaxed conglomerates were pure InAs, whereas the elastically strained islands (grey area) had a high GaAs content.

The experimental in-plane and out-of-plane diffuse X-ray diffraction patterns measured in the vicinity of the (220) and the (202) GaAs Bragg reflections together with calculated patterns for elastically strained islands containing 90% GaAs are shown in Fig. 6.

VIII.1.3 Structure analysis of islands grown at 480°C

For the sample grown at 480°C the line scan in the radial [110] direction through the (220) GaAs Bragg reflection is shown in Fig. 7(a). Compared with the previous samples, the region between plastically relaxed and elastically strained islands cannot be clearly separated. The composition analysis (Fig. 7(b)) also did not separate the corresponding intensity distributions. Both signals overlap in reciprocal space, so

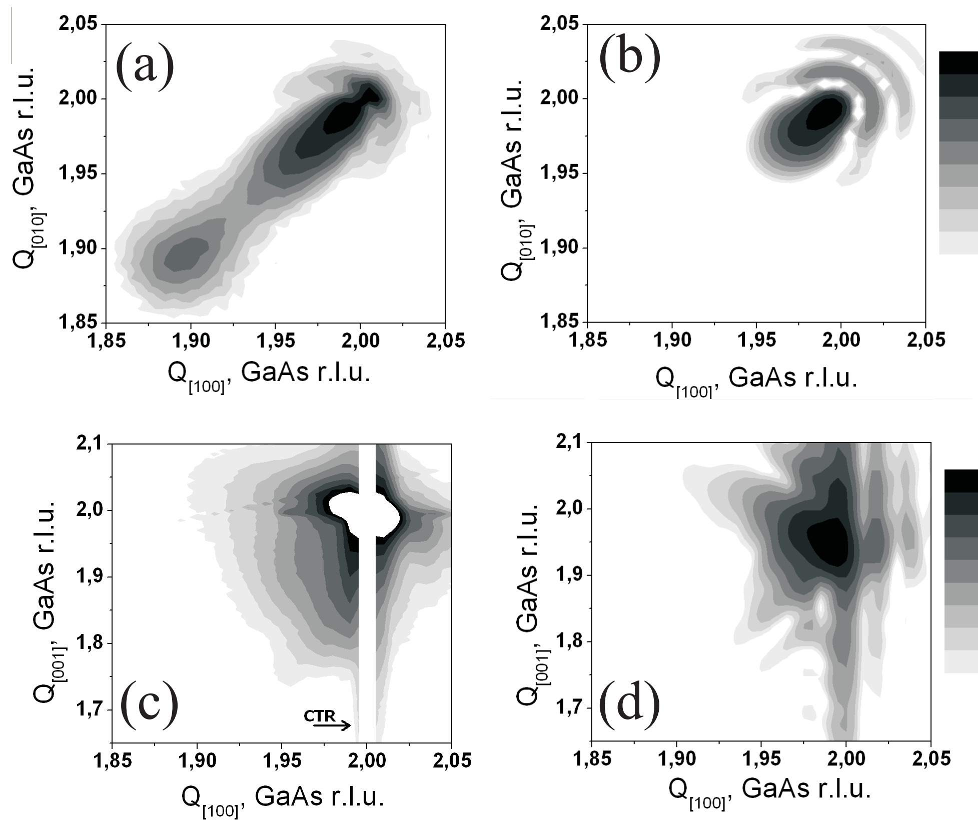

Figure 4: Experimental in-plane (a) and out-of-plane (c) reciprocal space maps in the vicinity of the (220) and the (202) GaAs Bragg reflections for sample grown at 530°C. The white vertical line in (c) at $Q_{[100]}$=2 r.l.u. corresponds to the crystal truncation rod (CTR), where the signal was not measured. Corresponding best-fit calculations of the diffuse intensity from elastically strained islands with an average composition close to $In_{0.2}Ga_{0.8}As$ (b,d).

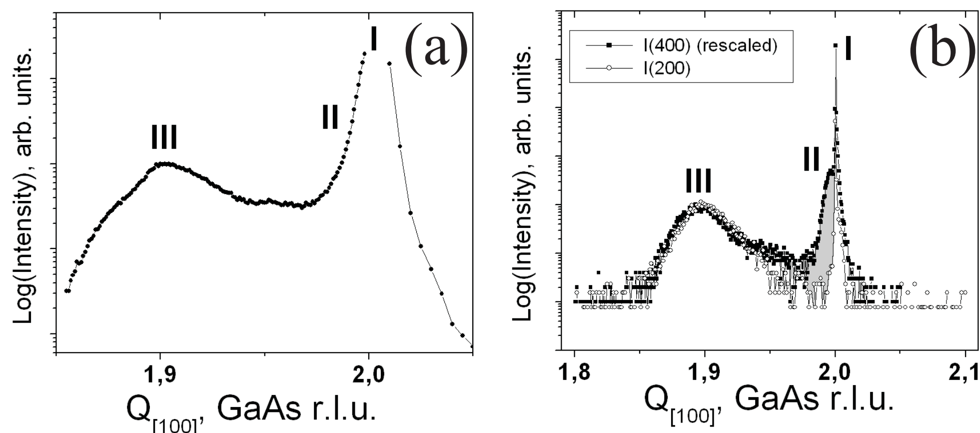

Figure 5: Experimentally extracted intensity profile along radial [110] reciprocal space direction through the (220) GaAs Bragg reflection (a), and intensity profiles along [100] reciprocal space direction through the (400) and (200) GaAs Bragg peaks (b). I - substrate peak position, II - signal from elastically strained islands, III - signal from plastically relaxed island conglomerates.

they cannot be separated analytically. The overlap arises from the broad diffracted signal from the strained islands and their higher In content relative to the previous samples. The 2D intensity distributions (Fig. 8) also did not permit the diffuse signals from the elastically strained islands to be analysed separately.

VIII.1.4 Discussion

Because of the lack of reliable structural data for the sample grown at 480°C additional experimental information about In-enrichment are required. The analysis of topographic images from the samples can yield information about the surface diffusion processes of the deposited InAs material. As shown in the previous chapter (VII), for In-rich islands grown on GaAs(001) the surface diffusion proceeds differently along orthogonal <110> crystallographic directions producing the detectable island shape anisotropy. Conversely, the observation of such anisotropy provides evidence that InAs diffusion on the surface was an important contribution to island formation. A lower anisotropy implies that InAs surface diffusion has less influence of on the island formation.

In Fig. 9 STM[1] and AFM topographical images of single islands from all three samples are shown in order of increasing average In content (not by the deposition temperature!). The first two Ga-rich islands (Fig. 9(a,b)) (average composition esti-

[1]The information about STM investigation on quantum dots can be found in [104].

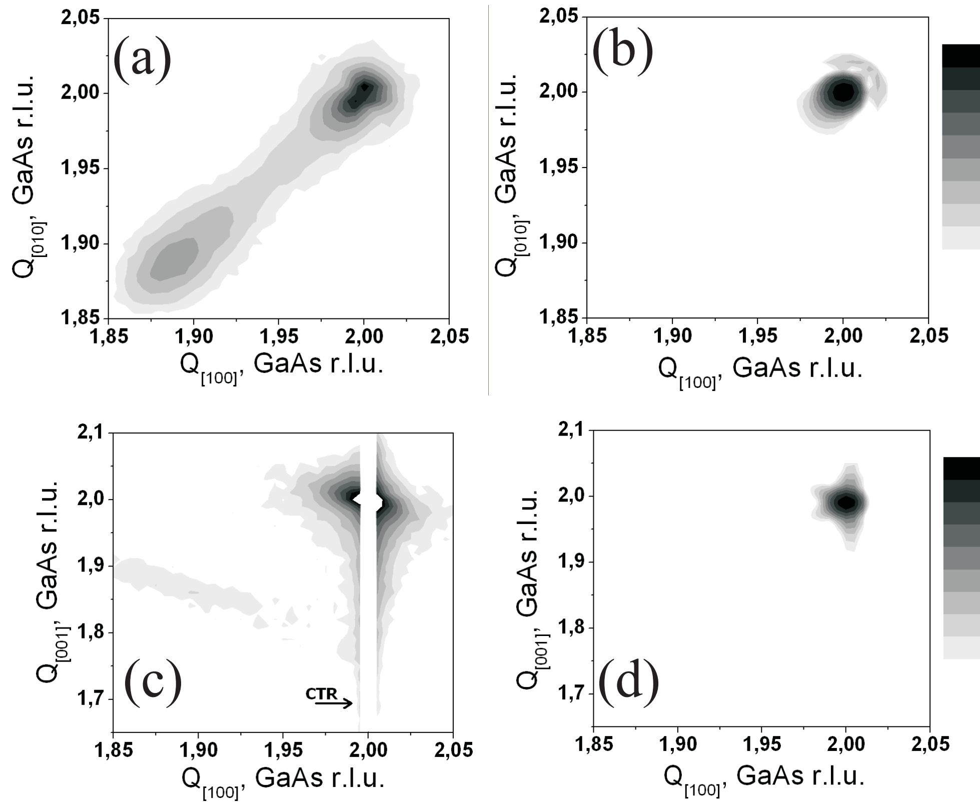

Figure 6: Experimental in-plane (a) and out-of-plane (c) reciprocal space maps in the vicinity of the (220) and the (202) GaAs Bragg reflections for sample grown at 500°C. The white vertical line in (c) at $Q_{[100]}$=2 r.l.u. corresponds to the crystal truncation rod (CTR), where the signal was not measured. Best-fit calculations of the diffuse intensity from elastically strained islands (b,d).

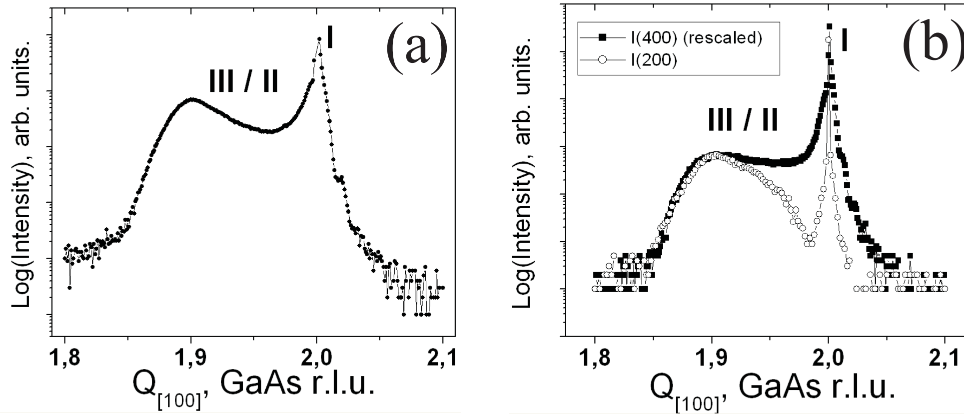

Figure 7: Experimental intensity profile (a) along the radial [110] direction through the (220) GaAs Bragg reflection, and (b) along [100] reciprocal space direction through the (400) and (200) GaAs Bragg peaks. I - substrate peak position, II/III - mixture of signals from elastically strained islands and from relaxed conglomerates.

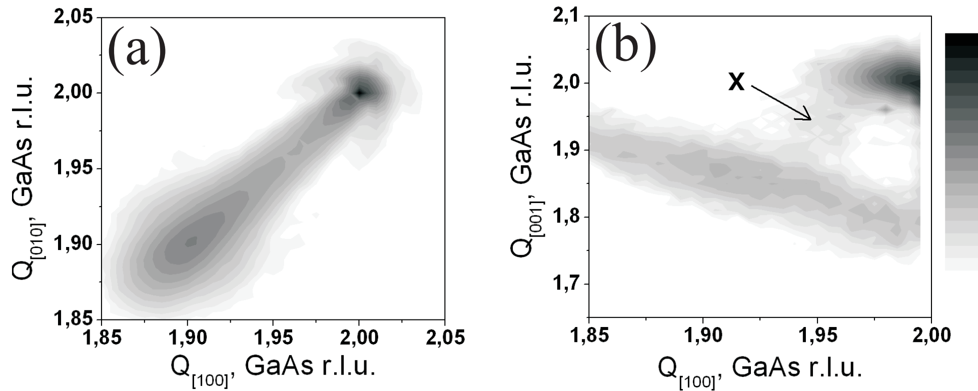

Figure 8: Experimentally measured in-plane (a) and out-of-plane (b) reciprocal space maps in the vicinity of the (220) and the (202) GaAs Bragg reflections for sample grown at 480°C.

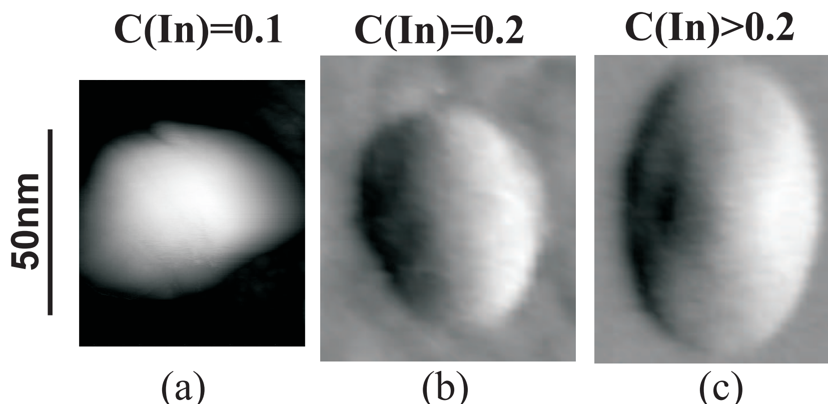

Figure 9: The topographical images of single islands with presumably different In content. The areas are scaled corresponding to their relative size. (a) STM image, (b,c) AFM images.

mated from diffraction data analysis) exhibit almost negligible shape anisotropy. The island shown in Fig. 9(c) has a prononced shape anisotropy and therefore a higher In content.

If the composition of the elastically strained islands is known, then conclusions about temperature driven island formation processes can be made. As a general observation, the island chemical composition approaches that of InAs with decreasing deposition temperature. Surface diffusion and a bulk diffusion are strongly temperature dependent thermally activated processes. The interplay between these processes determines the final island composition. From this point of view, In-enrichment at low island growth temperatures is evidence for temperature dependent InAs-GaAs intermixing. Furthermore, investigations of the temperature dependence of the InAs/GaAs diffusion coefficient [119] and Si interdiffusion in GaAs(001) [120] predict the corresponding process within the investigated island deposition temperature range to be about an order of magnitude. GaAs bulk diffusion processes are significantly reduced for a deposition temperature reduction of ΔT=50°C. At the lowest deposition temperature the minimal bulk diffusion means that InAs surface diffusion mainly supplying the island material.

An analysis of the relative changes in the amount of relaxed island conglomerates can help to clarify the distribution of material between islands and WL at each growth temperature. The structure grown at the moderate temperature of 500°C is taken as a reference. According to the proposed model, increasing the deposition temperature to 530°C should enhance the bulk GaAs diffusion process and the homogeneous islands should become more Ga-rich than the islands grown at 500°C. As a consequence, more unused InAs can be expected to be stored in relaxed conglomerates. In the reality (Fig. 2(c)), the opposite is observed.

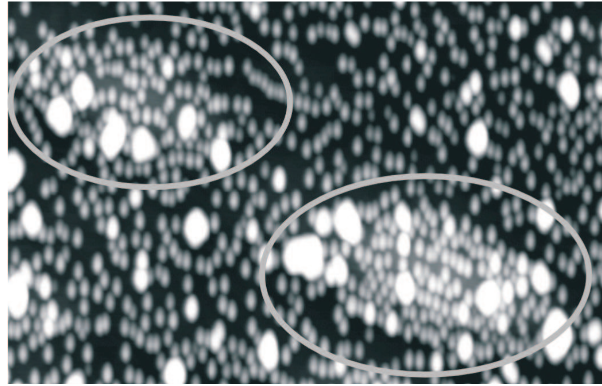

Figure 10: Surface AFM image of A sample grown at 480°C. The areas with high surface density islands are marked by the rings.

This effect can be explained by the increased surface mobility of InAs molecules at higher deposition temperatures. The higher surface mobility probably leads to the situation where the island growth due to InAs surface diffusion becomes comparable to the bulk GaAs material flux. As a result islands are formed with an average composition similar to that of samples grown at 500°C. The In-enrichment of upper parts of the island at 530° extracted from FEM modelling supports assumption concerning enhances surface diffusion of InAs.

The AFM images reveal small relative volume changes for islands grown at 530°C and 500°C. The relative decrease of the InAs volume in the relaxed conglomerates points to an *additional sink* of InAs. This sink could be the wetting layer. For systems with *strong intermixing* an increase in the WL thickness with increasing deposition temperature seems highly realistic.

For the sample grown at 480°C the thermally activated bulk diffusion is relatively small. The diffraction data and the anisotropic shape of the homogeneous islands on the surface indicate that the In content is high. Since a larger amount of the deposited InAs forms homogeneous islands, the relative volume of the relaxed InAs conglomerates compared to that for the sample grown at 500°C should decrease. The large-scale AFM images (Fig. 2(a)) do not confirm this idea. There must be additional processes at work. The main possibility would be the *decrease of the WL thickness* at the lower deposition temperature. The enlarged AFM image in Fig. 10 reveals a second possibility. On the image one can see two regions (in the rings) where small islands form zones with very high surface density ($\approx 10^{11}\text{cm}^{-2}$). The most of the large island conglomerates are also localized at these positions. The very small distance between neighboring small islands is indicative of low elastic strain and, consequently, low In content III.3. The surrounding surface regions have a lower surface density and larger inter-island distance indicating a higher InAs concentration.

The presence of densely packed regions can be explained by the low surface mobility for growth at 480°C [2]. In localized surface regions the mobility is insufficient for homogeneous material transport and the growing islands cannot obtain sufficient InAs. To reach the critical island volume, the system has to find more material. For regions with low surface diffusion, the only possibility is to pump the substrate material into the growing island. In such situations pure strain-driven GaAs diffusion seems to take place and, as a consequence, the unused InAs within these regions forms conglomerates. The proposed explanation should be tested experimentally. The diffracted signal corresponding to such Ga-rich islands can lie close to the substrate peak position in reciprocal space (Fig. 7(a)). Unfortunately, this signal is buried the intensity distribution from In-rich islands (in-plane) (Fig. 8). One possibility to extract this signal would be to use a synchrotron radiation with a coherence length comparable to the dimension of the region where Ga-enrichment effects take place.

Final evidence for the proposed surface/bulk diffusion interplay model is provided by the InAs/GaAs(001) island systems investigated in chapter VII. These structures were grown at 500°C with an InAs deposition rate five times faster. The faster deposition rate minimizes the time for homogeneous island growth. In this case the bulk diffusion has less time to proceed and as a result the islands become more In rich.

VIII.2 Investigation of the temperature dependent island growth mechanism in InAs/AlAs(001).

Three InAs island samples were grown at 480°C, 500°C, and 530°C on an AlAs(001) buffer layer (100nm on GaAs(001)) with an InAs deposition rate of 0.04ML/sec. During MBE growth the volume of InAs deposited was kept constant at 2.7ML (accounted for desorption) which corresponds to the moment of island coalescence. The corresponding large-scale "differential mode" AFM images are shown in Fig. 11. It can be seen, that coalescence regime has been reached for all three systems. It can be also seen that at lower growth temperatures the number of island conglomerates increases.

The samples grown at 480°C and 530°C were covered with a protective coating directly after preparation. Immediately before the X-ray diffraction experiments the coating was removed and the sample was put in a He environment. The sample grown at 500°C was investigated under ultra-high vacuum conditions [106]. Afterwards it has been exposed to the ambient air for a short time and then studied again using X-rays in He atmosphere.

Line scans in the radial [110] direction through the (220) GaAs Bragg reflection

[2] for given deposition conditions the temperature of 470-480°C was experimentally found to lay in the critical low-temperature region for the formation of 3D structures.

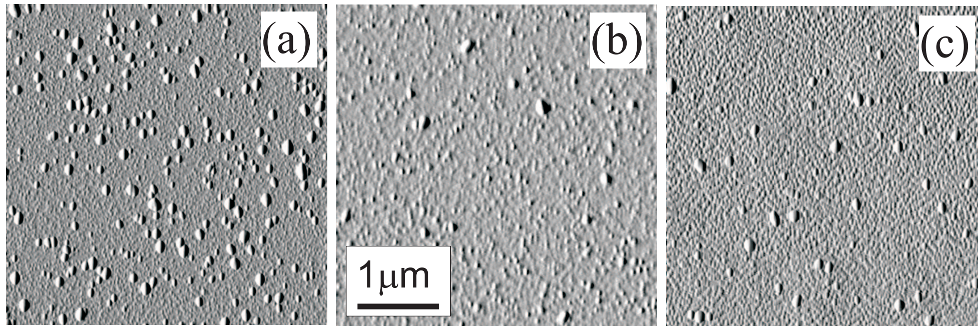

Figure 11: Topographic AFM images ($25\mu m^2$) for InAs(2.7ML)/AlAs(001) island systems grown at (a) 480°C, (b) 500°C , and (c) 530°C.

are shown on a logarithmic intensity scale in Fig. 12. Similar to the InAs/GaAs(001) samples, three main intensity distributions can be distinguished. The main difference is that region II for all three samples the signal from the strained islands is the same which indicates that the islands have similar strain states at all three growth temperatures. The island composition analysis shown in Fig. 13 for samples grown at the lowest and highest temperatures gave identical measured signals. This situation allows to analyse the relative amounts of material in relaxed conglomerates and elastically strained islands. The measured experimental intensity distributions for all three samples were rescaled relative to the relaxed peaks (III) (horizontal dashed line in Fig. 12). Since the same amount of InAs was deposited on all three samples, from the relative changes in intensity in regions III and II one can make conclusions about the material exchange process. To make this comparison more correct for the sample grown at 500°C the intensity profiles measured in vacuum and after exposure to air are shown. From the plots it can be clearly seen that with increase of growth temperature the relative amount of material stored in relaxed conglomerates decreases. This effect also can be directly seen in the AFM images in Fig. 11.

The 2D experimental in-plane and out-of-plane diffuse X-ray diffraction patterns measured in the vicinity of the (220) and (202) AlAs (GaAs) Bragg reflections are shown in Fig. 14. The 2D diffraction patterns can be analysed taking into account the dynamics of the material distribution as a function of growth temperature (see Fig. 1). On the out-of-plane plots, the diffuse part of the diffraction signal which becomes less intense for samples grown at high temperatures is associated with relaxed conglomerates. Conversely, the diffuse pattern from the elastically strained islands should increase with the growth temperature.

The diffuse scattering from both strained and relaxed islands overlap. In this situation, to analyse the structure of the elastically strained islands a new experimental technique had to be developed, which is described in detail in VIII.3. The composition of the strained islands was found to be close to $In_{0.8}Al_{0.2}As$, close to the

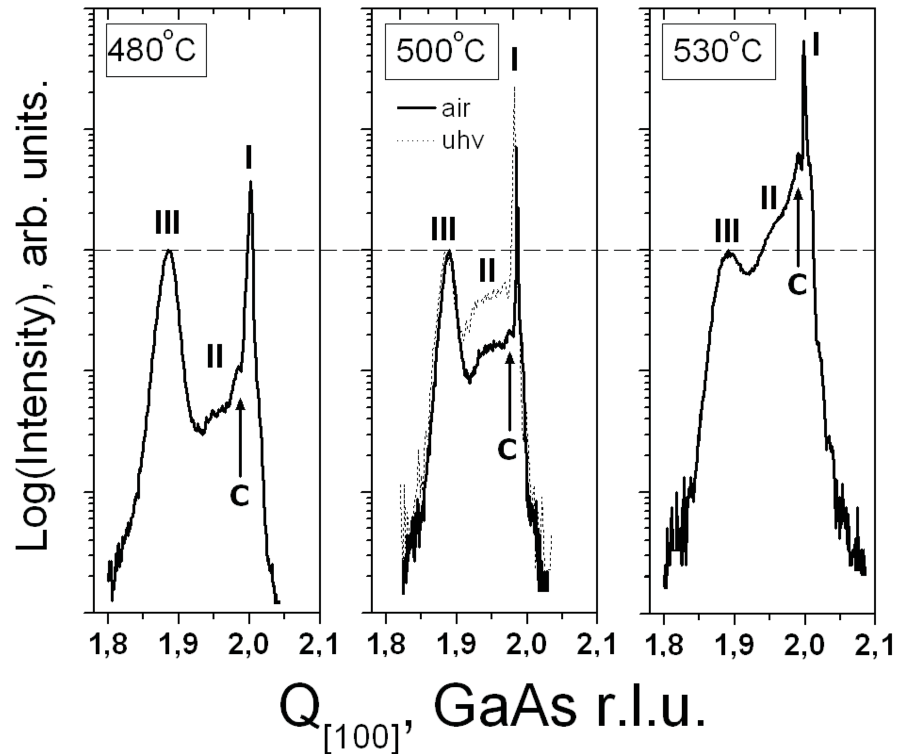

Figure 12: Experimental intensity profiles along the radial [110] reciprocal space direction through the (220) GaAs Bragg reflection for samples grown at 480°C, 500°C, and 530°C. I marks the substrate peak position, II - signal from the elastically strained islands, and III - signal from plastically relaxed island conglomerates. For sample grown at 500°C both results from uhv-measurements and measurements after exposure to the ambient air are shown. "C" -marks the correlation peak positions.

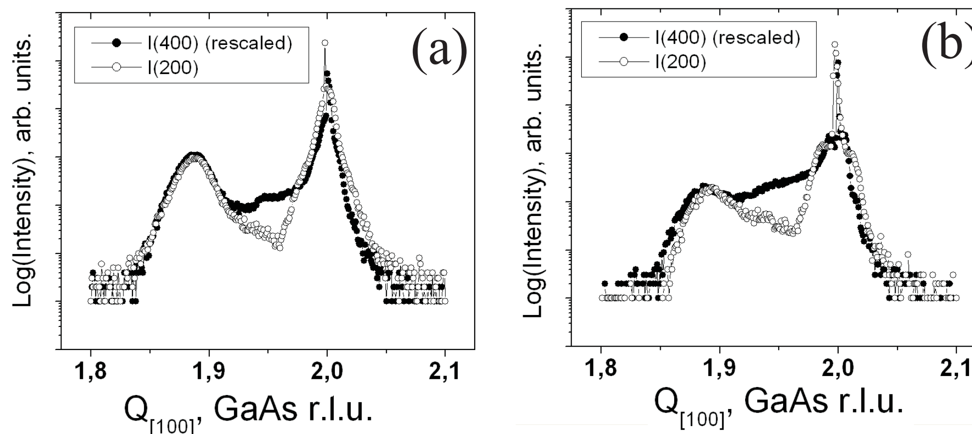

Figure 13: Experimental intensity profiles along the [100] reciprocal space direction through the (400) and (200) GaAs Bragg peaks for samples grown at (a) 480°C, and (b) 530°C.

composition of islands grown on GaAs(001) surface, where bulk diffusion had been suppressed by using a high InAs deposition rate. The constant chemical composition of the elastically strained islands indicates that the process responsible for island growth is essentially temperature independent. It appears that temperature activated bulk diffusion of AlAs from the substrate into the islands during homogeneous growth stage is small. This maximum concentration of 25% AlAs in the strained islands is at all growth temperatures limited by the solubility of InAs in AlAs. On the in-plane maps, the areas with signal from the strained islands were analysed by means of transversal line scans in Fig.15. This analysis revealed the increase in average island size with deposition temperature. The local topographic analysis of the island size with increasing deposition temperature (Fig. 16) also qualitatively agrees with X-ray data. On the Fig. 16(b) the island dimensions comparable to those in Fig. 16(a) can be associated to the better lateral resolution of the STM relative to the AFM-tool [105].

In the InAs/AlAs(001) system the growth of islands at different deposition temperatures is controlled by the limited intermixing of the incoming InAs and substrate material. With increasing deposition temperature the diffusion rate of Al atoms into the island will increase leading to Al-enrichment of the islands. To maintain the maximum allowed Al-concentration a certain InAs volume has to be accommodated in the island. This explains the increase in average island size with growth temperature. The demand for additional InAs for the growth of strained quantum dots explains the decrease of InAs in relaxed conglomerates.

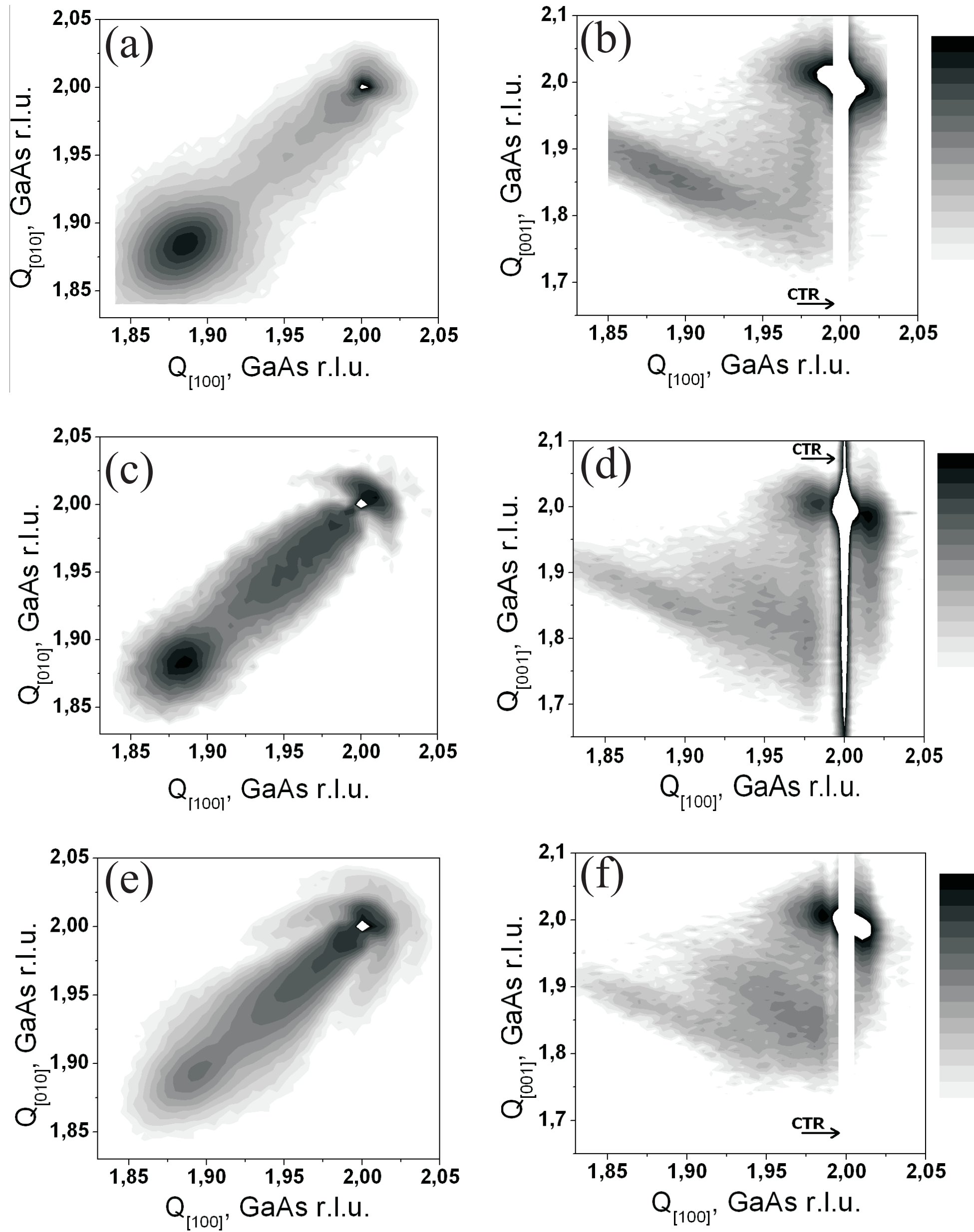

Figure 14: Experimental in-plane (left) and out-of-plane (right) reciprocal space maps in the vicinity of (220) and (202) GaAs Bragg reflections for samples grown at 480°C (a,b), 500°C (c,d), and 530°C (e,f). The white vertical lines on the out-of-plane patterns at $Q_{[100]}$=2 r.l.u. corresponds to the crystal truncation rod (CTR) position, where the signal was not measured. The substrate peaks on the in-plane maps are located at the cut-out intensity at $Q_{[100]}= Q_{[010]}$=2 r.l.u.

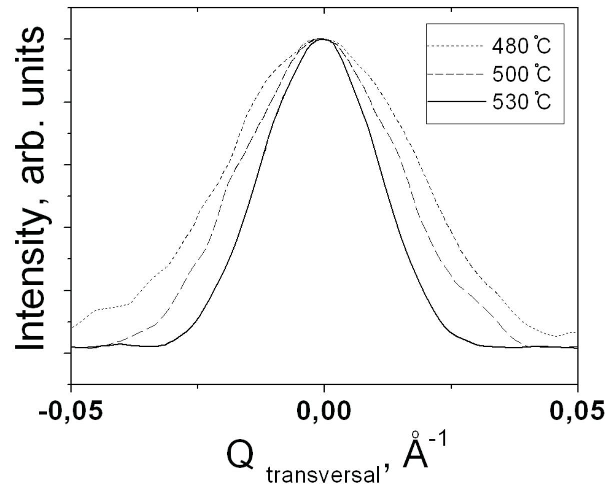

Figure 15: Experimental intensity distribution along scans transversal to the [110] direction through the reciprocal in-plane lattice point $Q_{[100]}=Q_{[010]}=1.95$ GaAs r.l.u. for samples grown under different deposition temperatures.

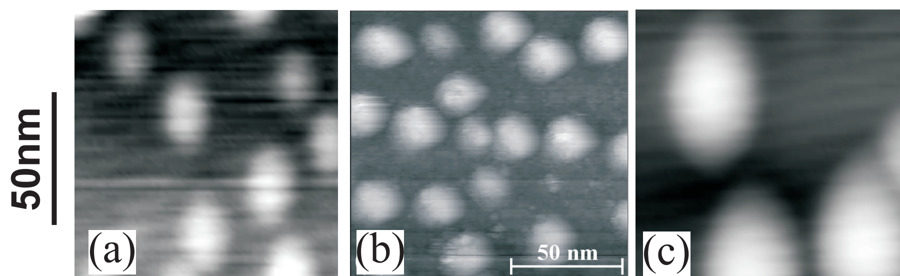

Figure 16: Enlarged images of islands grown on an AlAs(001) surface at deposition temperatures of (a) 480°C, (b) 500°C, and (c) 530°C.

VIII.3 Structural investigation of elastically strained InAs/AlAs(001) islands

The analysis of X-ray diffraction data from islands in the situation where the signals from the elastically strained and plastically relaxed islands overlap in reciprocal space is a non-trivial problem. It requires the development of special experimental techniques. The main idea of the proposed technique is to separate the diffuse intensity patterns of strained and partially relaxed islands by exploiting the effect of island oxidation.

The investigation was done using the sample growth at 500°C. The sample was first measured under ultra-high vacuum conditions and then the sample was exposed to ambient air for a short time to provide surface oxidation and measured again in He atmosphere keeping all other parameters in the X-ray diffraction experiment unchanged.

The sample topography was analysed by means of AFM and STM measurements in order that sufficient resolution could be achieved on both sub-nanometer and micrometer scale. This resolution scale was required to enable the precise determination of an average size of the small elastically strained islands and larger plastically relaxed conglomerates. The corresponding average island dimensions and densities are given in the Tab. VIII.1.

presumable state	height, nm	width, nm	density, cm^{-2}
elastically strained	4	20	$1.2 \cdot 10^{11}$
(partially) relaxed	>10	>50	$\approx 5 \cdot 10^{9}$

Table VIII.1: Experimentally determined island dimensions.

VIII.3.1 Method description

To analyse elastically strained islands we propose a new experimental X-ray diffraction technique based on island oxidation. Relative to the large islands, the volume of small strained islands diminishes more after oxidation and this effect can be used to distinguish the diffraction signal from small and large islands. The applicability of this technique requires the following conditions:

(i) oxidation leads to the formation of a stable amorphous oxide layer with a constant thickness on the top of the islands

(ii) the volume of the oxidized part of the island is smaller than the total volume of the island before oxidation (islands do not oxidize completely)

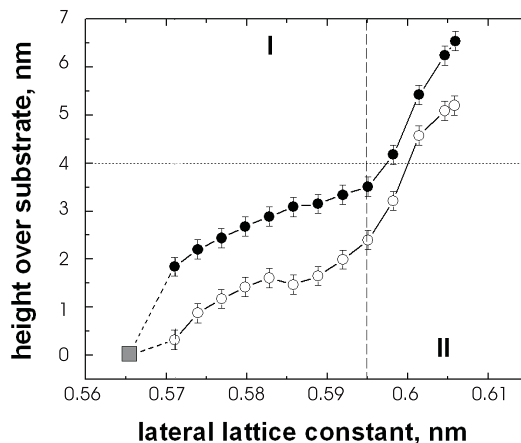

Figure 17: Lateral lattice constant profile over averaged island height for the sample in vacuum (dots) and directly after exposure to ambient air (circles). The bulk substrate lattice constant at zero height (grey square) is shown for reference. The dashed vertical line separates the parts of the curve, where the signals from elastically strained islands (I) and relaxed islands (II) dominate. The horizontal line is the average height of small islands from STM-measurements.

(iii) the crystalline part of the island remaining after oxidation inherits the scaled deformation state of the same island before oxidation

To prove our assumptions the simplified ISA model for the strain field in a non-buried elastically strained island was used (see II.11.2). Based on this consideration, the information about the height of each iso-strain part over the substrate surface was retrieved experimentally (VII). Figure 17 represents the retrieved average island lateral strain profile before and directly after oxidation at RT.

This profile is the result of averaging over all islands on the surface, and it does not fully represent either the strain state in the small strained islands nor in the large islands. Setting the upper height to the STM-derived height for small islands we allocate the part of the experimental curve in region (I) to elastically strained islands. Part (II) of the curve represents the region, where the relaxed islands have most influence. The bulk substrate lattice constant is shown at zero-height. It should be mentioned, that the discrepancy between the indirectly derived average height (7 nm) and directly estimated height (10nm) of large islands could be due to the fact, that on the top of large islands the strain gradient is essentialy zero. This leads to a reduction of the sensitivity of the method to the uppermost part of the average island strain profile.

If the requirement (iii) is not fulfilled, the uppermost island sections (larger lattice constants) after oxidation (amorphisation) should have disappeared. On the contrary,

one can observe different behavior - the proportional decrease of strain profile along the height axis for oxidized sample relatively to the non-oxidized one.

This means, that after oxidation in the crystalline part of the island the initial displacement field is rescaled proportionally to the new island dimensions. The height difference between the same "iso-strain" areas before and after oxidation can then be interpreted as an *average oxide layer thickness*. For region (I) in Fig. 17 this oxide layer thickness is 1.8±0.3nm. For comparison the native oxide thickness on a InAs(001) crystal (see Att. 3) was found to be ≈1.7 nm.

It is assumed that island oxidation leads to loss of material due to the amorphisation with redistribution of the strain in the remaining crystalline part. So, oxidation should lead to a decrease in the diffuse diffraction intensity in regions of interest in reciprocal space without changing the profile of the corresponding diffraction patterns.

It is also assumed, that in the case of the nanometer scale islands the changes in island size after oxidation will not cause a significant broadening in reciprocal space. Fig. 18 shows the Fourier transform of the shape function of a strain-free island close to the experimentally determined size for small island in vacuum and corresponding to the crystalline part of the same island after oxidation. The change in the small island dimensions (≈15%) correspond to the experimental oxide layer thickness. The changes of full width half maximum (Δ_{FWHM}) are $0.01Å^{-1}$. Since the experimental resolution was δ=$0.005Å^{-1}$ the changes in island size are not expected to cause any detectable broadening (this condition holds for $\delta \geq \frac{1}{2}\,\Delta_{FWHM}$).

After oxidation the diffracted intensity from the elastically strained islands will decrease proportionally to the relative amount of material lost by amorphisation. As an example, in Fig. 18 the oxidation of small strain-free islands will lead to a decrease in the maximum intensity signal by a factor of three.

Obviously, if two types of islands with different sizes undergo oxidation, the relative volume losses for smaller islands will be greater than for larger ones. For the structures under consideration, the relative loss of material will be in the order of ≈55% for small islands and not more than ≈25% for large islands. Since the diffracted intensity is proportional to the island volume squared, the relative intensity losses in this case should be at least 4:1. We propose to use the different intensity ratios to identify the diffraction pattern stemming from small strained islands.

VIII.3.2 Experimental implementation

The scans taken in the radial [110] direction in the vicinity of the (220) AlAs Bragg reflection for the sample in vacuum and directly after air exposure are shown in Fig. 19. The projection of $\mathbf{Q_{110}}$ on the $\mathbf{Q_{100}}$ axis was chosen to make the direct comparison of the data easier. In Fig. 19 three main regions can be distinguished (vertical lines). The intensity variations representing lateral lattice constant distributions in the elastically strained (region II) and relaxed (region III) islands can be distinguished. The relaxed islands are characterized by the narrow lattice constant

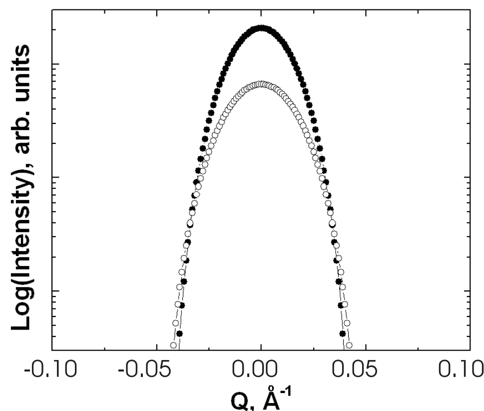

Figure 18: Line scan through Fourier transformed shape functions of small strain-free island in vacuum (dots), and for the crystalline part of the same island after oxidation (circles).

distribution positioned apart from the bulk substrate peak (region I). The elastically strained islands exhibit a lateral lattice constant distribution, starting at the position of the bulk substrate (island/substrate interface), and relaxing slowly to larger lattice constants (smaller **Q** values) on the top of the island. The data was normalized to the maximum intensity in region III ($\mathbf{Q_{100}} = 2.09\AA^{-1}$) from the relaxed islands. The comparison of the normalized intensity profiles before and after oxidation reveals the corresponding relative material losses in the small strained islands. The 2D in-plane intensity distributions in the vicinity of the (220) substrate Bragg peak measured under UHV-conditions and after air exposure are shown in Fig. 20. The relative intensity is decreased due to the reduction of the material in the island but no detectable signal broadening is observed. To get sufficient information about the strain field in small islands, the reciprocal space region containing signals from both lateral and vertical island strain field components (non-zero $\mathbf{Q_z}$ component of diffraction vector) should be investigated. The diffuse intensity patterns in the vicinity of the AlAs (202) Bragg reflection ($Q_x = Q_z = 2.222\AA^{-1}$) measured in vacuum and directly after oxidation in air are shown in Fig. 21. Here, the broad intensity distribution on the left of the substrate truncation rod ($\mathbf{Q_{100}} = 2.222\AA^{-1}$) is an envelope function resulted from overlap of diffuse signals from strained and relaxed islands. For a known lateral position of the intensity maximum for relaxed islands (region III in Fig. 19), the maximum intensity position along $\mathbf{Q_{001}}$ direction in Fig. 21 was found. After this, both patterns (Fig. 21 (a) and (b)) were rescaled relative to their intensities at these reciprocal space points. The normalized out-of-plane diffuse intensity pattern for the oxidized structure (Fig. 21(b)) was subtracted from the pattern measured for the sample in vacuum (Fig. 21(a)) to reveal the intensity reduction for the elastically

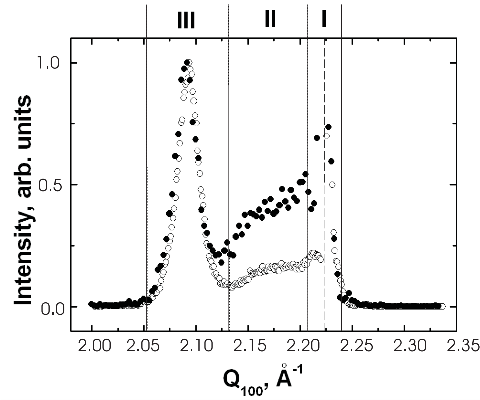

Figure 19: Line scans along the [110] direction for the same sample in vacuum (dots) and directly after exposure to air (circles). The vertical dashed line at $\mathbf{Q_{100}} = 2.222\mathring{A}^{-1}$ indicates the position of the (220) AlAs substrate bulk peak. Vertical black lines on the plot mark regions, where signals from the substrate (**I**), elastically strained islands (**II**), and relaxed islands (**III**) influence the intensity profile. The intensity at the bulk substrate position is truncated.

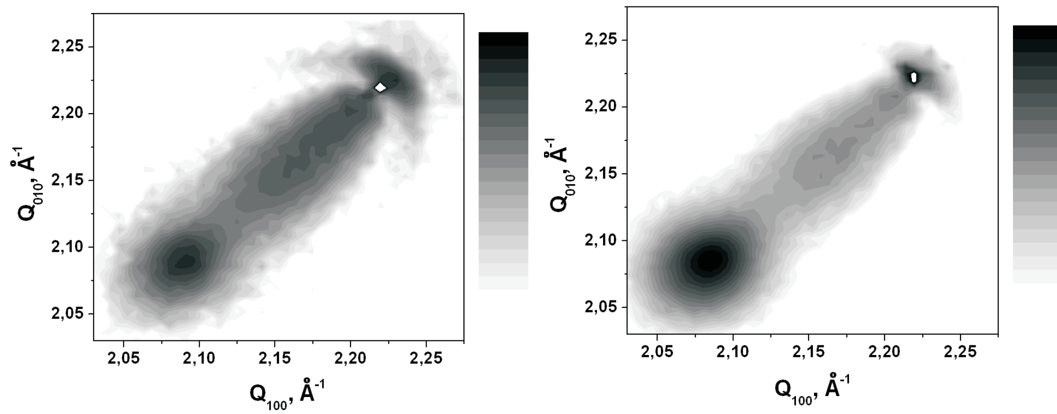

Figure 20: Log-Intensity scaled in-plane reciprocal space maps measured in the vicinity of the (220) substrate Bragg peak for the sample (left) under UHV-conditions and (right) after exposure to air. The cut-out at $\mathbf{Q_{100}} = \mathbf{Q_{010}} = 2.222\mathring{A}^{-1}$ marks the position of the (220) AlAs substrate peak.

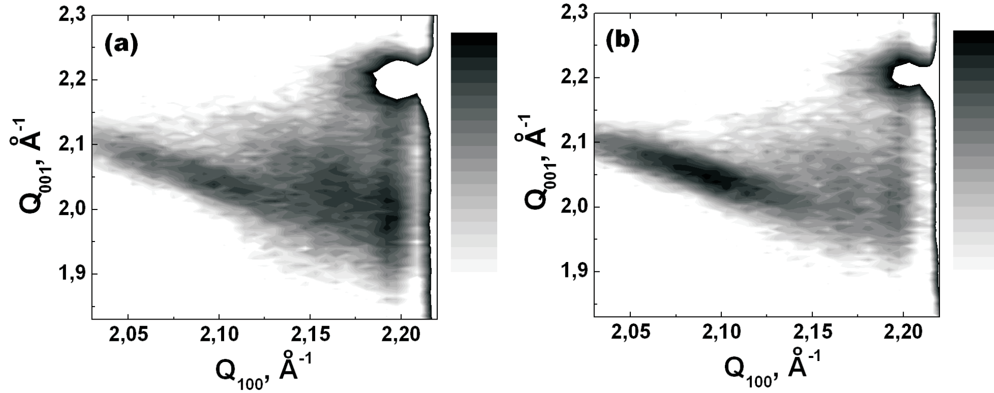

Figure 21: Logarithmically scaled reciprocal space maps in the vicinity of the AlAs (202) Bragg reflection ($\mathbf{Q_{100}} = \mathbf{Q_{001}} = 2.222\AA^{-1}$) for the sample in vacuum (a) and after exposure to air at RT (b). The strong signals from the bulk truncation rod and deformed substrate under the island are cut out.

strained islands. The envelope of resulting intensity profile should be the Fourier transform of the strain field in the small islands. The difference map is shown in Fig. 22(a). Knowing the size and shape of the small islands, the analysis of the difference map reveals the average island chemical composition. Numerical kinematical calculations of the diffuse intensity pattern based on finite element (FEM) simulations in frame of elasticity theory were carried out. Only the diffuse part representing the signal from elastically strained islands was used. Substrate material was not involved in the calculations, so the signal coming from the bulk substrate (truncation rod) as well as from deformed substrate under the island (high intensity part near the bulk substrate position) were not included. The calculated intensity pattern for an island with composition $In_{0.8\pm0.05}Al_{0.2\pm0.05}As$ (Fig. 22(b)) gave the best agreement with the experimental difference map.

VIII.4 Conclusions

The X-ray structure analysis of InAs/GaAs(001) and InAs/AlAs(001) islands in the coalescence stage was described for samples grown at different temperatures with a constant amount of deposited InAs. For the X-ray structure analysis of elastically strained InAs/AlAs(001) islands a new experimental technique has been developed. The main idea of the technique is to use the effect of island oxidation to extract the diffracted signal from elastically strained islands from the envelope signal containing the contribution stemming from plastically relaxed island conglomerates.

Based on the results of the X-ray analysis and direct observations using AFM conclusions about the temperature dependant formation mechanism of elastically

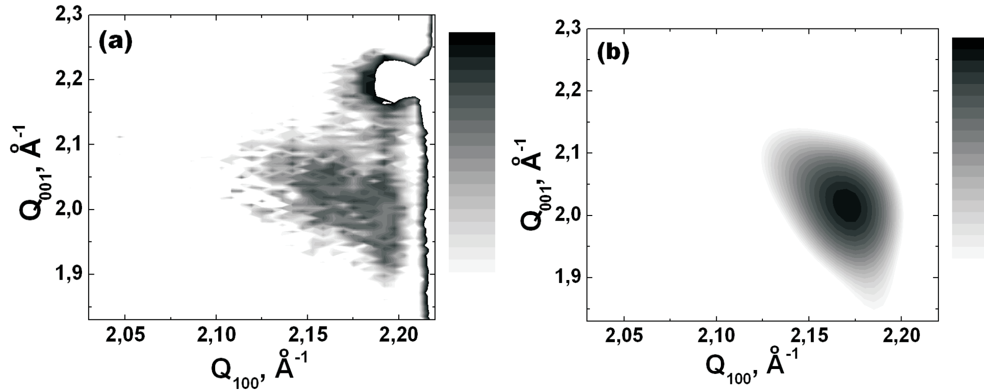

Figure 22: (a) experimental intensity pattern in the vicinity of the AlAs(202) Bragg reflection, obtained by subtraction of the patterns in Fig. 21; (b) calculated diffuse pattern for small islands of composition $In_{0.8}Al_{0.2}As$.

strained islands has been proposed. In InAs/GaAs(001) system strong intermixing between InAs and GaAs materials was found. The complex temperature-dependent interplay between the bulk diffusion of GaAs and the surface diffusion of InAs during island growth process was found to be responsible for the final island composition. In the InAs/AlAs(001) system the temperature independent limited solubility of InAs in AlAs was observed. Due to the limited material solubility, in this system the temperature activated AlAs bulk diffusion process is compensated by the additional InAs material supply leading to a temperature dependant increase of the strained island dimensions.

Chapter IX

Capped quantum dot systems

The final part of quantum-dot device preparation is the capping of the self-assembled islands [121]. Structural changes or intermixing, that may occur during capping are of technological importance [122], [123]. For buried structures transmission electron microscopy is the best method for directly measuring the island shape and size [124], [125]. However, sample preparation required means that the technique is not non-destructive. Photoluminescence measurements (PL) on buried QD systems is a widely-used non-destructive tool [126],[127] but the structural information from PL is indirect and is difficult to extract. X-ray diffraction is non-destructive and a reliable method for the structural analysis of buried island systems [128],[129].

In this chapter InAs/GaAs(001) and InAs/AlAs(001) islands grown under the same deposition conditions after capping with substrate material will be analysed. The good spatial separation of diffraction signal from relaxed InAs conglomerates is an advantage when following the structural changes and intermixing taking place during capping.

IX.1 Theoretical calculations

The strain-induced diffuse diffraction patterns for islands with different geometrical parameters and chemical composition buried in a GaAs matrix material have been calculated using FEM-models in a linear-elasticity approach. The out-of-plane intensity patterns calculated for InAs islands with a base width of 40nm and height to radius ratios (HRR) of 1, 0.5, and 0.25 are shown in Fig. 1(a,b,c). The patterns calculated for islands with the same base width and HRR=1 with varying chemical composition are presented in Fig. 1(d,e,f). The strain field within the whole model (island in the matrix) was calculated. On the calculated maps, the horizontal and vertical intensity stripes going through the (202) substrate position ($Q_{[100]}= Q_{[001]}=0$) correspond to truncation effects related to the finite model dimensions. The results correlate well to similar calculations for Ge islands buried in a Si(001) matrix [130]. For buried

InAs islands the calculated intensity profiles differ qualitatively from the patterns calculated for equivalent non-buried islands (see V). For strong intermixing in the islands these differences disappear. For strong interdiffusion (reduced misfit-strain) the elastic strain energy is localized in the volume limited by the island dimensions and in this situation the capping layer has only a minor influence.

IX.2 Experimental investigations

Two samples were prepared at a deposition temperature of 500°C. This temperature was chosen, because it corresponds to the deposition conditions for the uncapped islands measured under UHV (See VIII). 2.7ML of InAs at a deposition rate of 0.04ML/s were deposited onto GaAs(001) and AlAs(001) surfaces. After the formation of 3D structures was observed in RHEED, both systems were capped with 30nm of the substrate material. The X-ray measurements on both samples were done in He atmosphere.

For GaAs/InAs/GaAs(001) and AlAs/InAs/AlAs(001) systems the in-plane diffraction maps in the vicinity of the (220) GaAs/AlAs Bragg reflection are shown in Fig. 2(b,d). For comparison the same maps, measured for equivalent uncapped samples are given in Fig. 2(a,c). It can be seen, that for both buried systems the intensity signal stemming from the elastically strained islands (see VIII) remains almost unaltered. From this observation the conclusion can be made, that capping of strained islands does not affect their chemical composition. This indicates that both systems already before capping reached an energetically favorable island composition within their homogeneous growth stage.

The signal stemming from plastically relaxed island conglomerates undergoes changes in both systems. In GaAs/InAs/GaAs(001) this signal completely disappears, while for AlAs/InAs/AlAs(001) the maximum position of the intensity distribution is changed slightly. These effects are more apparent in Fig. 3, where the experimental intensity distributions along the radial [110] direction through (220) GaAs/AlAs substrate peaks for capped and uncapped systems are shown. The curved have been rescaled for comparison. The structural changes can be associated with intermixing. The InAs conglomerates become enriched with the GaAs(AlAs) substrate material. Temperature-activated bulk diffusion should be the dominant mechanism controlling this process. The driving force seems to bring the composition of the relaxed conglomerates to minimize the elastic misfit strain at the interface between these conglomerates and the overgrowing matrix material. The intermixing causes the maximum value of the lateral lattice constant difference between the material in the relaxed conglomerates and the matrix to decrease. In reciprocal space it results in a shift of the corresponding intensity distribution towards the position of the substrate peak. The expected behavior can be clearly seen for the AlAs/InAs/AlAs(001) system, where the final position of the peak from the relaxed material can still be

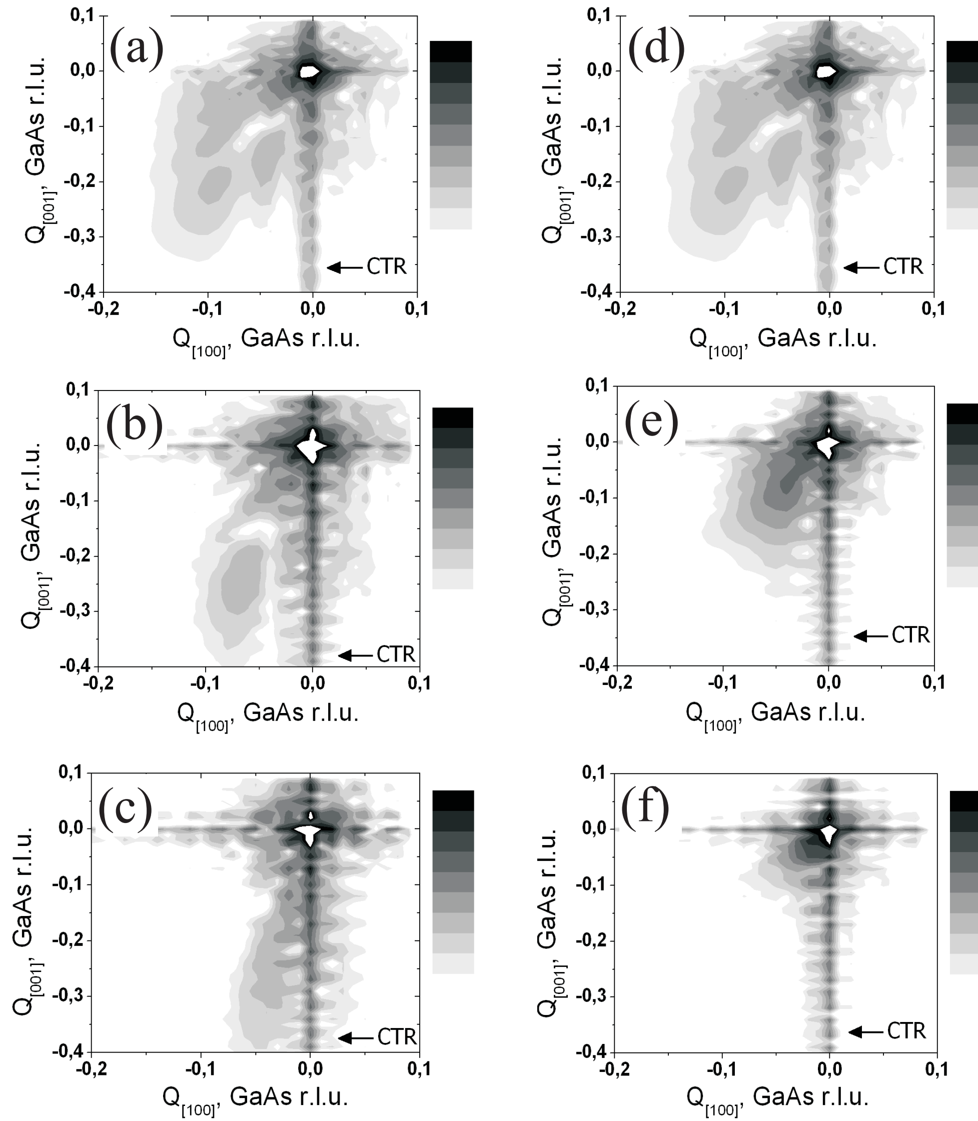

Figure 1: Calculated out-of-plane diffuse intensity patterns in the vicinity of the (202) GaAs Bragg reflection for models of InAs islands (width 40nm) with HRR=1 (a), HRR=0.5 (b), and HRR=0.25 (c) buried in a GaAs matrix. The influence of the island chemical composition (island width 40nm) on the diffuse intensity distribution is shown for InAs (d), $In_{0.5}Ga_{0.5}As$ (e), and $In_{0.2}Ga_{0.8}As$ (f). The horizontal and vertical intensity stripes going through the (202) substrate position ($Q_{[100]}= Q_{[001]}=0$) correspond to truncation effects (CTR) related to the finite model dimensions.

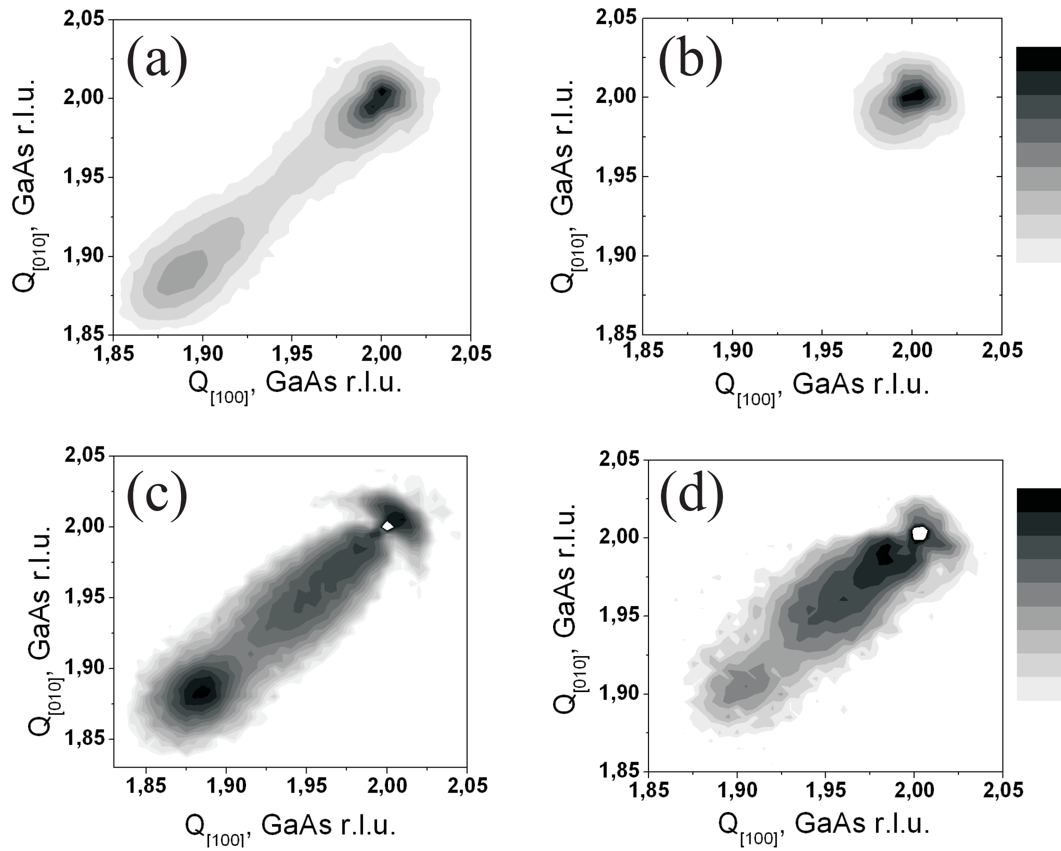

Figure 2: Experimental in-plane diffraction patterns in the vicinity of the (220) GaAs/AlAs Bragg reflection for (b) buried GaAs/InAs/GaAs(001) and (d) AlAs/InAs/AlAs(001) islands. The corresponding maps for uncapped samples are shown on plots (a) and (b).

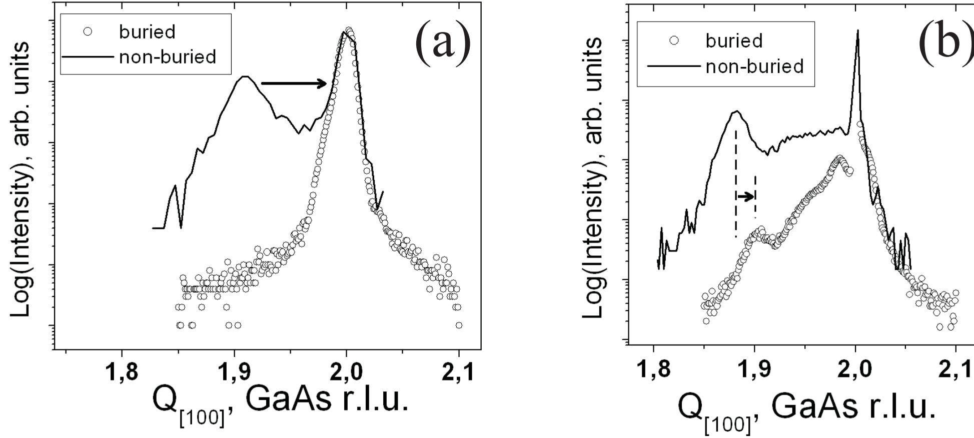

Figure 3: Experimental line scans along the radial [110] direction through the GaAs/AlAs (220) Bragg reflection measured for capped and uncapped (a) InAs/GaAs and (b) InAs/AlAs systems.

resolved, revealing a small shift and so slight intermixing.

In the case of GaAs/InAs/GaAs(001), the final position of the relaxed conglomerates peak seems to coincide with the substrate reflection, pointing on the maximum possible enrichment with GaAs. Since the final peak position cannot be directly observed, additional methods were used to find evidence of strong intermixing. The measurement of capping layer thickness has been done. In the case of strong interdiffusion a significant amount of material from the capping layer should have found its way into the InAs conglomerates. To estimate the GaAs material loss, XRR measurements (Fig. 4(a)) and a CTR-profile measurements in the vicinity of (202) GaAs bulk reflection (Fig. 4(b)) were performed. As a model to fit the experimental XRR profile a thin oxide layer (1.5nm), capping GaAs layer (initial thickness 30nm), and a quantum dot layer of unknown thickness was used. The best fit is shown in Fig. 4(a) as a solid line. The best fit model gave a capping layer thickness of 25nm. The 5nm difference from the nominal GaAs cap layer thickness was also checked by measuring the distance between the capping layer maxima on the CTR. As an additional cross check the measured average thickness of quantum dot layer in the capped structure (4nm) was compared to that found from XRR measurements of the same non-capped sample (2nm). The increase in the average quantum dot layer thickness after capping accompanied by the decrease of capping layer thickness relative to its nominal value confirms the intermixing of the plastically relaxed quantum dots with the surrounding matrix.

In the GaAs/InAs/GaAs(001) system the experimentally found lattice mismatch less than 1% the strain field is entirely concentrated within the island. So, the interface between the islands and capping material can be assumed to be free of

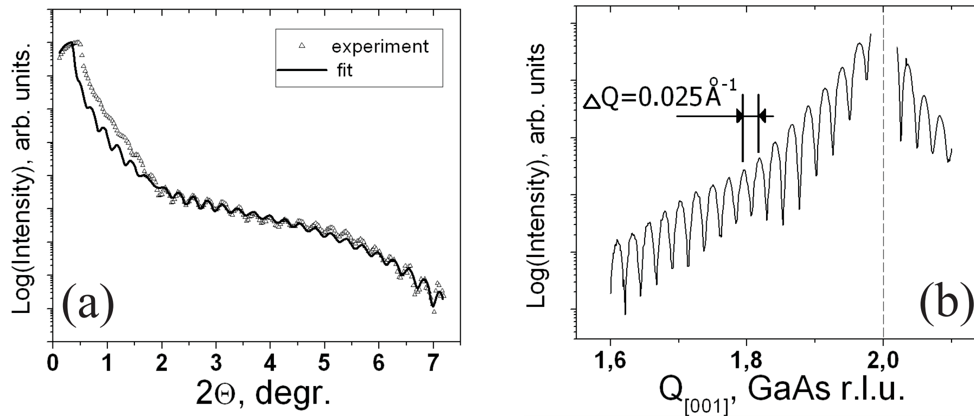

Figure 4: (a) Experimental X-ray reflectivity profile and its theoretical fit, (b) a line scan along the [001]-crystal truncation rod for GaAs/InAs/GaAs(001).

structural defects.

The situation is different in the AlAs/InAs/AlAs(001) system. Due to insufficient solubility the lattice mismatch at the island/capping layer interface is 5-6%. In the Fig. 5(a) the experimentally derived out-of-plane intensity pattern in the vicinity of the (202) AlAs(GaAs) Bragg peak for AlAs/InAs/AlAs(001) is shown. In this system, the absence of intermixing in strained islands during capping allows it to be assumed that the capped islands to have the same shape and composition as they had before capping.

The calculated (202) diffraction pattern is shown in Fig. 5(b) for capped islands with a given composition and size for pure elastic deformation. The comparison of the experimental and calculated patterns reveals significant differences. Furthermore, the experimental pattern does not correspond to the diffuse signal calculated for the equivalent uncapped islands (see V). These results show that the misfit strain accommodation at the island/capping layer interface is complex: misfit dislocations should form at the interface between the islands and the capping material [131].

IX.3 Conclusions

The structural changes in GaAs/InAs/GaAs(001) and AlAs/InAs/AlAs(001) quantum dots taking place during the capping process have been analyzed. It was found that due to the mutual solubility of InAs and GaAs the residual elastic misfit strain is reduced due to bulk diffusion of GaAs material from the capping layer into the InAs conglomerates. This seems to have a positive effect on the uniformity of the quantum dot system. The low solubility of InAs and AlAs leads to the less misfit strain reduction at the island/capping layer interface and, as a consequence, to the

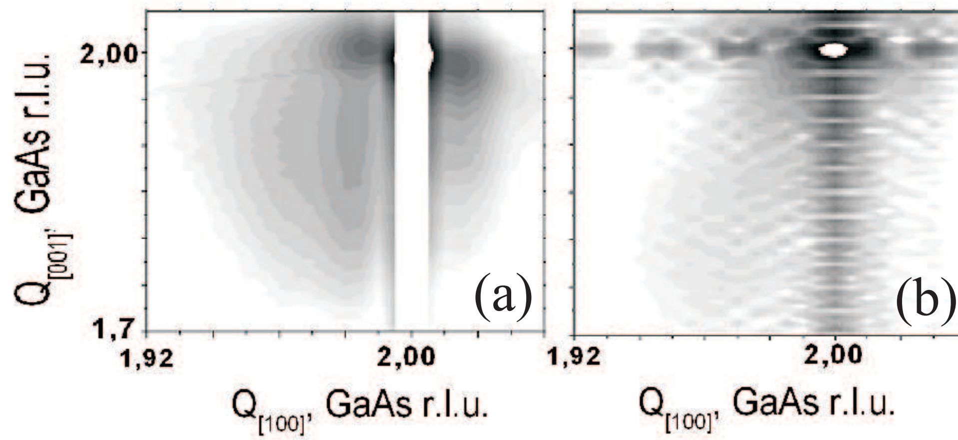

Figure 5: (a) Experimental out-of-plane intensity pattern in the vicinity of the (202) AlAs(GaAs) Bragg reflection; (b) Intensity pattern for an imaginary island with moderate dimensions and a composition of $In_{0.8}Al_{0.2}As$ buried in an AlAs matrix calculated assuming that the system is elastically strained.

creation of structural defects.

Chapter X

Summary and outlook

X.1 Summary

In this work the InAs/GaAs(001) and InAs/AlAs(001) island systems in the uncapped and capped states were studied using synchrotron X-ray diffraction and AFM(STM). The iterative FEM-based technique was applied in parallel to analyse the quantum dot composition.

The theoretical FEM-based calculations of X-ray diffraction patterns were provided to analyse the sensitivity of the diffraction patterns in the reciprocal space to structural and morphological changes in the quantum dots. The application limits for simplified models describing strain distribution in quantum dots were determined.

The homogeneous island growth in the InAs/GaAs(001) system with increasing amount of deposited InAs was investigated. It was found that within the whole homogeneous growth stage the average dot size and chemical composition is independent on the amount of deposited InAs. The increase of deposited InAs primarily leads to a proportional increase of the dot surface density. The island positional correlation analysis for InAs/GaAs(001) sample with high island surface density was provided using GISAXS and GID tools. Using iterative FEM-based technique and experimental methods the average composition of $In_{0.5}Ga_{0.5}As$ was found for the investigated SK-QDs. The conclusions about the nature of the quantum dot intermixing process and formation in InAs/GaAs(001) system were made.

The analysis of InAs/GaAs(001) and InAs/AlAs(001) systems grown at different temperatures with a constant amount of deposited InAs in the coalescence regime was done. For the X-ray structure analysis of elastically strained InAs/AlAs(001) islands a new experimental technique has been developed. The main idea of the technique is to use the effect of island oxidation to extract the diffracted signal from elastically strained islands from the envelope signal containing the contribution stemming from plastically relaxed island conglomerates. In InAs/GaAs(001) system strong intermixing between InAs and GaAs materials was found. The complex temperature-

dependent interplay between the bulk diffusion of GaAs and surface diffusion of InAs during the island growth process was found to be responsible for the strong changes of island composition and wetting layer thickness. In the InAs/AlAs(001) system due to the probable limited material solubility the temperature the temperature activated AlAs bulk diffusion process is compensated by the additional InAs material supply leading to an increase of the dimensions of the strained islands without changing their composition.

The investigation of capping effect on the island structure in InAs/GaAs(001) and InAs/AlAs(001) systems in coalescence regime was done. It showed the minor influence of the capping layer on the structure of homogeneous islands and a strong effect on the chemical composition of the relaxed conglomerates. The changes of the chemical composition of relaxed conglomerates during capping process is determined by the solubility of the matrix and island materials. In the InAs/AlAs(001) system the complex elastic-plastic deformation on the interface between the homogeneous islands and overgrowing matrix was assumed.

X.2 Outlook

Based on the results in this thesis the following topics would be interesting for the future requiring the application of X-ray structure analysis:

- The structural changes in the islands during the 2D-3D growth transition.
- The influence of the deposition parameters on the island spatial arrangement for systems with high island surface densities.
- The structural investigation of island systems grown in their homogeneous regime under variation of a single deposition parameter (similar to the increase of deposited InAs, investigated in this thesis).
- The investigation of island growth mechanisms varying different deposition parameters using the coalescence regime.
- Detailed analysis of capping effects on the island structure and topography.

Appendix A

List of frequently used abbreviations

XRD - X-ray diffraction
GID - grazing-incidence diffraction
GISAXS - grazing-incidence small angle X-ray scattering
HRXRD - high-resolution X-ray diffraction
XRR - X-ray reflectivity
RSM - reciprocal space map
HRR - island height to radius ratio
MBE - molecular beam epitaxy
UHV - ultra high vacuum
AFM - atomic force microscopy
STM - scanning tunnelling microscopy
FFT - fast Fourier transform
WL - wetting layer
SK - Stranski-Krastanow growth
FWHM - full width at half maximum

Appendix B

Linear deformation field algorithm for elastically strained island

Below is the algorithm for a simple linear deformation of an elastically strained hemispherical island (MATLAB command file). It is based on the approximated ISA model describing the elastic deformation in uncapped islands. This algorithm was developed by Alexander Petrov (TUHH) and used for reference numerical calculations. As shown in V, calculations of the island strain field based on the given algorithm revealed physically correct results for elastic deformations below 1%.

```
% Notes:
% 1. Deformation "eps" is a function of Z
% 2. Cylindrical symmetry is taken rad(z)

clear all;

%Note: Below the basis of used crystal structre is given

ra(1,:)=[0 0 0]; %Example: primitive cell

% Variable
ff=1;

% lattice parameter
a=6.0584;

% maximum island hight
zmax=50;

%top (min.) and bottom (max.) deformations
```

```
emin=0;
emax=-0.067;


% Poisson coefficient
nu=0.35;

% number of atoms in the cell
n_atom=length(ra(:,1));

%atom number
n=1;

for k=1:n_atom

   %coordinate start
   x=a*ra(k,1);
   y=a*ra(k,2);
   z=a*ra(k,3);

   % vertical deformation of first layer is approximated at
   % should work quite good at reasonable deformations
   eps=emax-(emax-emin)*(z*(1-2*nu*emax)/2)/zmax;
   z=z*(1-2*nu*eps);

   while (z < zmax)

     % radius function
       rad=sqrt(zmax^2-z^2);

       % deformation function
       eps=emax-(emax-emin)*z/zmax;

       az=a*(1+eps);

       K(ff,1)=az;
       K(ff,2)=z;
       ff=ff+1;
       xz=x*(1+eps);
       yz=y*(1+eps);
       nx1=fix((rad+xz)/az);
```

```
        nx2=fix((rad-xz)/az);
        for i=-nx1:nx2
            xi=az*i+xz;
            radi=sqrt(rad^2-xi^2);
            ny1=fix((radi+yz)/az);
            ny2=fix((radi-yz)/az);
            for j=-ny1:ny2
               r(n,:)=[xi (az*j+yz) z k];
               T(n,1)=xi;
               T(n,2)=(az*j+yz);
               T(n,3)=z;
               n=n+1;
            end
        end

        % vertical deformation is approximated at a/2
        eps=emax-(emax-emin)*(z+a*(1-2*nu*eps)/2)/zmax;
        z=z+a*(1-2*nu*eps);
   end
end

dlmwrite('filename.dat',K,',') %file with deformation values
dlmwrite('filename1.dat',T,',') %file with changed atomic coordinates

%visualize the island

color=[1 0 0; 0 1 0; 0 0 1; 1 0 1];
scatter3(r(:,1), r(:,2), r(:,3), 10, color(r(:,4),:));
```

Appendix C

Investigation of native oxide on InAs(001) single-crystal wafer

InAs(001) miscut-free single-crystal wafer produced by GIRMET (Moscow, Russia) was used for this investigation. The sample was transferred into the UHV-chamber (10^{-10} mbar), and cleaned by ion bombardment at RT and annealed at 450°C until the characteristic (4x2)-c(8x2) LEED-pattern corresponding to the In-terminated reconstructed surface appeared [132].

For chemical analysis of the oxidized InAs(001) surface the photoemission spectra from the crystal surface in the vacuum and directly after its short exposure to the ambient air were collected and compared. The UPS measurements were carried out at the Flipper-II station of HASYLAB/DESY, Hamburg. The incident photon energy was 60 eV. The photoemission data for oxide-free and oxidized surfaces are shown in Figure 1(a).

The analysis of photoemission spectra for the oxide-free InAs(001) surface revealed its high stoichiometric purity. The signals from In and As atoms can be clearly resolved. After surface oxidation the signal from the As atoms is no longer visible. In addition, the shift in binding energy of the surface In atoms shows that the chemical bonding state has changed. This observation allows to assume the surface to be covered by indium oxide.

The X-ray reflectivity measurement on the oxidized sample was performed at the BW2 beam-line at HASYLAB/DESY. The incoming radiation energy was 9.6 keV. The low-angle intensity distribution was recorded for 2θ angles up to 6°. The recorded reflectivity curve was fitted using the *fewlay* software package. As a fit model an oxide layer of unknown composition and thickness on the InAs substrate was used. The electron density of the InAs material was set to the tabulated value. The substrate roughness was the final adjustable parameter. The experimental reflectivity curve and theoretical curve are shown in figure 1. The extracted best-fit model parameters are shown in the table below. The oxide layer density is given as a real component of refraction coefficient. For the oxide layer with the given electron density

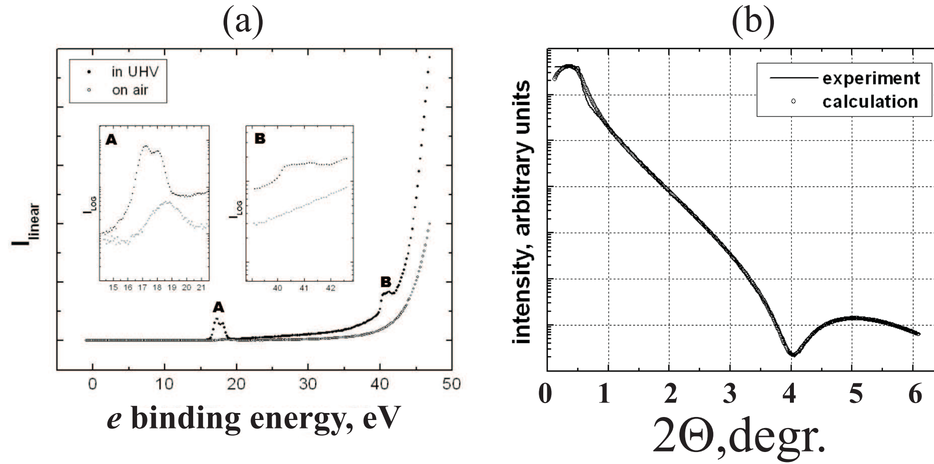

Figure 1: (a) - The electron binding energy calculated from photoemission data for an InAs(001) single-crystal wafer in vacuum and after oxidation. The parts of the spectra with As peaks from $3d_{3/2}$ and $3d_{5/2}$ core levels (**B**) and In peaks from $4d_{3/2}$ and $4d_{5/2}$ core levels (**A**); (b) - Experimental X-ray reflectivity curve and its theoretical fit.

a corresponding thickness of 1.7±0.4 nm was found.

The estimated electron density of the oxide layer reveals the presence of an In-rich oxide with density >7g/cm^3. This result correlates well with the information derived from the photoemission data.

	t, nm	σ, nm	$\delta(\delta_{lit})$
InO	1.7	0.4	$2.4E^{-5}$
InAs	-	0.1	$1E^{-5}$

Short CV of the author

was born on 15th of August 1978 in Kharkov, USSR

1985-1995 secondary school, Kharkov, USSR/Ukraine

1995-1999 Bachelor in Metallurgy from Kharkov Polytechnical Institute, Ukraine

1999-2000 Diploma Engineer in Physical Analysis of Materials from Kharkov National Technical University, Ukraine

2000-2003 Master of Science in Materials Science from Hamburg University of Technology, Germany

2003-2007 Research associate at the Institute of Experimental Physics/HASYLAB (DESY), University of Hamburg, Germany

Author publications list

A. Zolotaryov, A. Bolz, A. Schramm, W. Hansen, R.L. Johnson, *Oxidation as an assistant tool for structural analysis of inhomogeneous nanoscale InAs/AlAs(001) island system*, physica status solidi (a): Proc. Conf. XTOP 2006, (accepted for publication).

A. Zolotaryov, Ch. Heyn, A. Schramm, W. Hansen, and R.L. Johnson, *Investigation of spatial ordering in MBE-grown self-assembled strain-free GaAs quantum dot system*, HASYLAB annual report, 1011-1012 (2006).

A. Zolotaryov, K. Shcherbachev, F. Wu, and R.L. Johnson, *Investigation of damage in GaAs single crystals after irradiation by Ne+ ions*, HASYLAB annual report, 1009-1010 (2006).

A. Zolotaryov, A. Bolz, C. Kumpf, S. Volland, and R.L. Johnson, *Determination of the thickness of oxide layers on InAs/AlAs(001) island structures*, HASYLAB annual report, 731-732 (2005).

A. Zolotaryov, A. V. Penkov, A. G. Ponomarenko, V. V. Kondratenko, T. I. Peregon, L. P. Tishenko, C. Kumpf, and R.L. Johnson, *Investigation of residual stresses in the Si/Mo/Si(001) layer system*, HASYLAB annual report, 749-750 (2005).

A. Zolotaryov, A. Bader, C. Schumacher, P. Bach, L.W. Molenkamp, F. Wu, A. Stahl, C. Kumpf, E. Umbach, and R.L. Johnson, *Investigation of stress relaxation in Heusler-alloy thin films: NiMnSb*, HASYLAB annual report (2002).

Author conference list

XTOP 2006, Baden-Baden, Germany

HASYLAB Users meeting 2006, Hamburg, Germany

Autumn School on X-Ray Scattering, 2005, Smolenice, Slovakia

DPG 2005, Berlin, Germany

HASYLAB Users meeting 2005, Hamburg, Germany

HASYLAB Users meeting 2004, Hamburg, Germany

Acknowledgements

Author would like to gratefully acknowledge the following persons:

Prof. Dr. Robert L. Johnson (University of Hamburg) for supervising my PhD project at HASYLAB, DESY.

Prof. Dr. W. Hansen (University of Hamburg) for the productive research cooperation that was used as a background for this thesis.

Dr. Andreas Schramm (University of Hamburg) for his great support with the sample preparation and AFM measurements.

Dr. Arne Bolz (University of Hamburg/Philips) for preparation and transfer of the UHV samples and useful discussions.

Dr. Ch. Kumpf (University of Wuerzburg) for his generous help and important consultations during the measurement times at the BW2 beam-line.

Dr. A. Vishnevski (Hamburg University of Bundeswehr) for support in finite element calculations.

Dr. A. Petrov (Hamburg University of Technology) for the extremely useful discussions and suggestions and his friendly help.

My friends and relatives for continuous providing the author with the positive motivation.

Bibliography

[1] C. Kittel, *Introduction to Solid State Physics*, Book, Wiley&Sons, New York (1995).

[2] Neil W. Ashcroft, N. D. Mermin, *Solid State Physics*, Book, Itps Thomson Learning (1976).

[3] L. Jacak, P. Hawrylak, A. Wojs, *Quantum Dots*, Springer, Berlin (1998).

[4] L. V. Keldysh, *Fizika Tverdogo Tela (Sov. Phys. Solid State)* **4**, 2265 (1962).

[5] M. Grundmann, *Nano-Optoelectronics: Concepts, Physics and Devices*, Springer, Berlin-Heidelberg (2002).

[6] S. V. Gaponenko, *Optical Properties of Semiconductor Nanostructures*, Cambridge University Press, Cambridge, USA, (1998).

[7] U. Woggon, *Optical Properties of Semiconductor Quantum Dots*, SpringerTracts in Modern Physics **136**, Berlin, (1997).

[8] L. Esaki, *Do-it-yourself Quantum Mechanics in Low-dimensional Structures*, Physica Scripta **T42**, 102 (1992).

[9] D. Bimberg, M. Grundmann and N. N. Ledentsov, *Quantum Dot Heterostructures*, John Wiley&Sons, New York (1999).

[10] D. K. Ferry and S. M. Goodnick, *Transport in Nanostructures*, Cambridge University Press, Cambridge, (1997).

[11] D. Bimberg, *Quantum dots for lasers, amplifiers and computing*, J. Phys. D: Appl. Phys. **38**, 2055 (2005).

[12] H. Cao, J. Y. Xu, W. H. Xiang, Y. Ma, S. H. Chang, S. T. Ho, and G. S. Solomon, *Optically pumped InAs quantum dot microdisk lasers*, Appl. Phys. Lett. **76**, 3519 (2000).

[13] K. J. Luo, J. Y. Xu, H. Cao, Y. Ma, S. H. Chang, S. T. Ho, and G. S. Solomon, *Dynamics of GaAs/AlGaAs microdisk lasers*, Appl. Phys. Lett. **77**, 2304 (2000).

[14] B. Sonnenberg-Klein, K. L. Silverman, and R. P. Mirin, *Semiconductor Lasers for Lightwave Communications Systems*, Proc., Denver, SPIE **4533**, (2001).

[15] Victor M. Ustinov, Alexey E. Zhukov, Anton Yu. Egorov, and Nikolai A. Maleev, *Quantum Dot Lasers*, Springer (2003).

[16] C. Kapteyn, *Optical memory concepts with self-organized quantum dots - material systems and energy-selective charging*, 10th Int. Symp. Nanostructures: Physics and Technology, St Petersburg, Russia, June 17-21, (2002).

[17] R. J. Warburton, *Optical emission from a charge-tunable quantum ring*, Nature **405**, 926 (2000).

[18] R. C. Ashoori, *Electrons in artificial atoms*, Nature **379**, 413 (1996).

[19] A. L. Rogach, D. V. Talapin, E. V. Shevchenko, *Organization of Matter on Different Size Scales:Monodisperse Nanocrystals and Their Superstructures*, Adv. Funct. Mater. **12**, 653 (2002).

[20] Jelena Vuckovic, David Fattal, Charles Santori, Glenn S. Solomon, and Yoshihisa Yamamoto, *Enhanced single-photon emission from a quantum dot in a micropost microcavity*, Appl. Phys. Lett. **82**, 3596 (2003).

[21] Jelena Vuckovic and Yoshihisa Yamamoto, *Photonic crystal microcavities for cavity quantum electrodynamics with a single quantum dot*, Appl. Phys. Lett. **82**, 2374 (2003).

[22] G. S. Solomon, J. A. Trezza, and J. S. Harris, Jr., *Effects of monolayer coverage, flux ratio, and growth rate on the island density of InAs islands on GaAs*, Appl. Phys. Lett. **66**, 3161 (1995).

[23] F. C. Frank and J. H. van der Merwe, *One-dimensional dislocations.*, Proc. Roy. Soc. Lond **A 198**, 205 (1949).

[24] M. Vollmer and A. Weber, *Keimbildung in übersättigten Gebilden*, Z. Phys. Chem. **119**, 227 (1926).

[25] I. N. Stranski and L. Krastanow, *Sitzungsberichte d. Akad. d. Wissenschaften*, Wien, Abt. IIb **146**, 797 (1937).

[26] D. Vanderbit and L. K. Wickham, *Elastic energies of coherent germanium. islands on silicon*, Proc. Mater. Res. Soc. Symp. **202**, 555 (1991).

[27] W. Ostwald, *Über die vermeintliche Isomerie des roten und gelben Quecksilberoxyds und die Oberflächenspannung fester Körper*, Z. Phys. Chem. **34**, 495 (1900).

[28] F. K. LeGoues, M. C. Reuter, J. Tersoff, M. Hammar, and R. M. Tromp, *Cyclic Growth of Strain-Relaxed Islands*, Phys. Rev. Lett **73**, 300 (1994).

[29] Ch. Heyn, *Critical coverage for strain-induced formation of InAs quantum dots*, Phys. Rev. B **64**, 165306-1 (2001).

[30] K. Zhang, J. Falta, Th. Schmidt, Ch. Heyn, G. Materlik, and W. Hansen, *Distribution and shape of self-assembled InAs quantum dots grown on GaAs (001)*, Pure Appl. Chem. **72**, 199 (2000).

[31] D. J. Eaglesham, and M. Cerullo, *Dislocation-Free Stranski-Krastanow Growth of Ge on Si(100)*, Phys. Rev. Lett. **64**, 1943 (1990).

[32] P. B. Joyce, T. J. Krzyzewski, G. R. Bell, B. A. Joyce, T. S. Jones, *Composition of InAs quantum dots on GaAs(001): Direct evidence for (In,Ga)As alloying*, Phys. Rew. B **58**, 15981 (1998).

[33] P. Ballet, J. B. Smathers, and G. J. Salamo, *Morphology of InAs self-organized islands on AlAs surfaces*, Appl. Phys. Lett. **75**, 337 (1999).

[34] G. S. Solomon, J. A. Trezza, and J. S. Harris, Jr., *Substrate temperature and monolayer coverage effects on epitaxial ordering of InAs and InGaAs islands on GaAs*, Appl. Phys. Lett. **66**, 991 (1995).

[35] K. Tillmann, A. Förster, *Crytical dimenstions for the formation of interfacial misfit dislocations of* $In_{0.6}Ga_{0.4}As$ *islands on GaAs(001)*, Thin Solid Films **93**, (2000).

[36] E. E. Koch, D. E. Eastman, and Y. Farges, *Synchrotron Radiation - A Powerful Tool in Science*, Handbook on Synchrotron Radiation **1a**, E. E. Koch, ed., North-Holland Publishing Company; Amsterdam, (1983).

[37] D. T. Cromer and J. B. Mann, *X-ray scattering factors computed from numerical Hartree-Fock wave functions*, Acta Cryst. **A24**, 321 (1968).

[38] A. Wilson, *International Tables for Crystallography*, Volume **A**, (1995).

[39] L. Kissel and R. Pratt, *Corrections to tabulated anomalous-scattering factors*, Acta Cryst. **A46**, 170 (1990).

[40] Balyuzi, *Analytic approximation to incoherently scattered X-ray intensities*, Acta Cryst. **A31**, 600 (1975).

[41] G. H. Vineyard, *Die Konstitution der Mischkristalle und die Raumfüllung der Atome*, Z. Phys. **5**, 17 (1921).

[42] W. L. Bragg, *The diffraction of short electromagnetic waves by a crystal*, Proc. Cambridge Phil. Soc. **17**, 43 (1913).

[43] S. Takagi, *Dynamical theory of diffraction applicable to crystals with any kind of small distortion*, Acta Cryst. **15**, 1311 (1962).

[44] J. R. Fienup, *Phase retrieval algorithms: a comparison*, Appl. Optics **21**, 2758 (1982).

[45] I. A. Vartanyants, *Coherent X-ray diffraction from quantum dots*, (to be published).

[46] André Authier, *Dynamical Theory of X-Ray Diffraction*, Oxford University Press, USA (2004).

[47] Terrence Jach and P. L. Cowan, *Dynamical diffraction of X-rays at grazing angle*, Phys. Rev. B **39**, 5739 (1989).

[48] B. K. Vainshtein, *Fundamentals of Crystals*, Springer, Berlin (1981).

[49] D. M. Vasiliev, *Diffrakzionnie metodi issledovanija struktur*, SPbGTU (1998).

[50] B. Ya. Pines, *Lekzii po strukturnomu analizu*, Kharkov, USSR (1967).

[51] H. Dosch, *Evanescent absorption in kinematic surface Bragg diffraction*, Phys. Rev. B **35(5)**, 2137 (1987).

[52] Markus Rauscher, *Grazing incidence small angle x-ray scattering from free-standing nanostructures*, J. Appl. Phys. **86**, 6763 (1999).

[53] U. Pietsch, V. Holy, and T. Baumbach, *High Resolution X-ray Scattering*, Springer, Berlin (2004).

[54] S. P. Timoshenko and J. N. Goodier, *Theory of Elasticity*, 3rd ed. McGraw-Hill, New York, (1972).

[55] E. Popov, *Engineering Mechanics of Solids*, 2nd ed., Prentice Hall.

[56] N. P. Kobayashi, T. R. Ramachandran, P. Chen, and A. Madhukar, *In-situ atomic force microscope studies of the evolution of InAs three-dimensional islands on GaAs(001)*, Appl. Phys. Lett. **68**, 3299 (1996).

[57] T. H. Metzger, I. Kegel, R. Paniago, and J. Peisl, *Grazing incidence x-ray scattering: an ideal tool to study the structure of quantum dots*, J. Phys. D: Appl. Phys. **32**, A202 (1999).

[58] I. Kegel, T. H. Metzger, A. Lorke, J. Peisl, J. Stangl, G. Bauer, K. Nordlund, W. V. Schoenfeld, and P. M. Petroff, *Determination of strain fields and composition of self-organized quantum dots using X-ray diffraction*, Phys. Rev. B **63**, 035318 (2001).

[59] I. Kegel, T. H. Metzger, A. Lorke, J. Peisl, J. Stangl, G. Bauer, J. M. Garcia, and P. M. Petroff *Nanometer-Scale Resolution of Strain and Interdiffusion in Self-Assembled InAs/GaAs Quantum Dots*, Phys. Rev. Lett. **85**, 1694 (2000).

[60] H. Zabel, *X-ray and neutron reflectivity analysis of thin films and superlattices*, Appl. Phys. A 58, 159 (1994).

[61] D. Bahr, W. Press, R. Jebasinski, and S. Mantl, *X-ray reflectivity and diffuse-scattering study of CoSi2 layers in Si produced by ion-beam synthesis*, Phys. Rev. B **47**, 4385 (1993).

[62] L. G. Parratt, *Surface Studies of Solids by Total Reflection of X-rays*, Phys. Rev. **95**, 359 (1954).

[63] L. Névot and P. Croce, *Characterization of surfaces by grazing x-ray reflection*, Rev. Phys. Appl. **15**, 761 (1980).

[64] J. P. Hirth and J. Lothe, *Theory of dislocations*, Wiley, New York (1982).

[65] G. Köstner and U. Gsele, *Reduced critical thickness for relaxing heteroepitaxial films on compliant substrates*, Appl. Phys. Lett. **82**, 3209 (2003).

[66] D. Maroudas, L. A. Zepeda-Ruiz, and W. H. Weinberg, *Kinetics of strain relaxation through misfit dislocation formation in the growth of epitaxial films on compliant substrates*, Appl. Phys. Lett. **73**, 753 (1998).

[67] A. Zolotaryov, A. Bader, C. Schumacher, P. Bach, L.W. Molenkamp, F. Wu, A. Stahl, C. Kumpf, E. Umbach, and R.L. Johnson, *Investigation of stress relaxation in Heusler-alloy thin films: NiMnSb*, HASYLAB annual report (2002).

[68] Masao Kimura, Ana Acosta, Hiroshi Fujioka, and Masaharu Oshima, *Generalized grazing-incidence-angle x-ray scattering analysis of quantum dots*, J. Appl. Phys. **93**, 2034 (2003).

[69] M. Grundmann, O. Stier, and D. Bimberg, *InAs/GaAs pyramidal quantum dots: Strain distribution, optical phonons, and electronic structure*, Phys. Rev. B **52**, 11969 (1995).

[70] P. Keating, Phys. Rev. B **145**, 637 (1966).

[71] A. M. Saitta, *Ab initio molecular-dynamics study of electronic and optical properties of silicon quantum wires: Orientational effects*, Phys. Rev. B **53**, 1446 (1996).

[72] S. Christiansen, M. Albrecht, H. P. Strunk, and H. J. Maier, *Strained state of Ge(Si) islands on Si: Finite element calculations and comparison to convergent beam electron-diffraction measurements*, Appl. Phys. Lett. **64**, 3617 (1994).

[73] J. Stangl, V. Holy, and G. Bauer, *Structural properties of self-organized semiconductor nanostructures*, Rev. Mod. Phys. **76**, 725 (2004).

[74] T. Benabbas, P. Franois, Y. Androussi, and A. Lefebvre *Stress relaxation in highly strained InAs/GaAs structures as studied by finite element analysis and transmission electron microscopy*, J. Appl. Phys. **80**, p.2763 (1996).

[75] C. Pryor, J. Kim, L. W. Wang, A. J. Williamson, and A. Zunger, *Comparison of two methods for describing the strain profiles in quantum dots*, J. Appl. Phys. **83**, 2548 (1998).

[76] M. J. Turner, R. W. Clough, H. C. Martin, and L. J. Topp, *Stiffness and Deflection Analysis of Complex Structures*, Journal of Aeronautical Sciences **23**, 805 (1956).

[77] M. Benyoucef, M. Kuball, G. Hill, M. Wisnom, B. Beaumont, and P. Gibart, *Finite element analysis of epitaxial lateral overgrown GaN :Voids at the coalescence boundary*, Appl. Phys. Lett **79**, 4127 (2001).

[78] Ashok Rajamani, *Intrinsic tensile stress and grain boundary formation during Volmer-Weber film growth*, Appl. Phys. Lett. **81**, 1204 (2002).

[79] J. Stangl, A. Daniel, V. Holý, T. Roch, G. Bauer, I. Kegel, T. H. Metzger, Th. Wiebach, O. G. Schmidt, and K. Eberl, *Strain and composition distribution in uncapped SiGe islands from x-ray diffraction*, Appl. Phys. Lett. **79**, 1474 (2001).

[80] G. R. Liu and S. S. Quek Jerry, *A finite element study of the stress and strain fields of InAs quantum dots embedded in GaAs*, Semicond. Sci. Technol. **17**, 630 (2002).

[81] T. Benabbas, Y. Androussi, and A. Lefebvre, *A finite-element study of strain fields in vertically aligned InAs islands in GaAs*, J. Appl. Phys. **86**, 1945 (1999).

[82] M. L. Williams, *Stress singularities resulting from various boundary conditions in angular corners of plates in extension*, ASME J. Appl. Mech. **19**, 526 (1952).

[83] B. J. Spencer, and J. Tersoff, *Stress and first-order dislocation energies in equilibrium Stranski-Krastanow islands*, Phys. Rev. B **63**, 205424 (2001).

[84] H. T. Johnson, and L. B. Freund, *Mechanics of coherent and dislocated island morphologies in strained epitaxial material systems*, J. Appl. Phys **81**, 6081 (1997).

[85] W. R. Busing and H. A. Levy, *Angle Calculations for 3- and 4-Circle X-ray and Neutron Diffractometers*, Acta Cryst. **22**, 457 (1967).

[86] E. Vlieg, *Integrated Intensities Using a Six-Circle Surface X-ray Diffractometer*, J. Appl. Cryst **30**, 532 (1997).

[87] H. Schulte-Schrepping, J. Heuer, B. Hukelmann, *Adaptive indirectly cooled monochromator crystals at HASYLAB*, J. Synchrotron Rad. **5**, 682 (1998).

[88] O. Bunk, *Bestimmung der Struktur komplexer Halbleiter-Oberflächenrekonstruktionen mit Röntgenbeugung*, Doktorarbeit, HASYLAB, DESY, Hamburg (1999).

[89] Thomas M. Schultz, *2 and 3 Dimensional Systems Studied Using X-ray Crystallographic Techniques*, Ph. D. thesis, Aarhus University (1998).

[90] M. Schmidbauer, Th. Wiebach, H. Raidt, M. Hanke, R. Köhler, and H. Wawra *Ordering of self-assembled Si(1-x)Ge(x) islands studied by grazing incidence small-angle x-ray scattering and atomic force microscopy*, Phys. Rev. B **58**, 10523 (1998).

[91] J. Stangl, V. Holý, T. Roch, A. Daniel, G. Bauer, J. Zhu, K. Brunner, and G. Abstreiter, *Grazing incidence small-angle x-ray scattering study of buried and free-standing SiGe islands in a SiGe/Si superlattice*, Phys. Rev. B **62**, 7229 (2000).

[92] S. Rozhok, S. Jung, and V. Chandrasekhar, *Atomic force microscopy of nickel dot arrays with tuning fork and nanotube probe*, J. Vac. Sci. Technol. B **21(1)**, 323 (2003).

[93] Pacific Nanotechnology aducation site: www.pacificnanotech.com/afm-tutorial.html

[94] R. Lazzari, *IsGISAXS: a program for grazing-incidence small-angle X-ray scattering analysis of supported islands*, J. Appl. Cryst. **35**, 406 (2002).

[95] *IsGISAXS: a tool for Grazing Incidence Small Angle X-ray Scattering analysis for nanostructures*, IsGISAXS, version 2.5, R. Lazzari.

[96] The program fewlay can be obtained from Andreas Stierle (stierlemf.mpg.de)

[97] Tutorial Script: *X-ray Scattering from Semiconductor Nanostructures*, www.hlphys.uni-linz.ac.at

[98] A. L. Golovin, R. M. Imamov and O. G. Melikyan, *Diffraction and X-ray reflection at grazing incidence. Possibilities of studying multilayer thin-film structures*, J. Appl. Cryst. **22**, 406 (1989).

[99] Qi-Kun Xue, *Atomic structure of Faceted Planes of Inas Quantum Dots on GaAs(001) studied by scanning tunnelling microscopy*, Jpn. J. Appl. Phys. **38**, 500 (1999).

[100] Ichiro Tanaka, I. Kamiya, H. Sakaki, N. Qureshi and S. J. Allen, Jr., and P. M. Petroff, *Imaging and probing electronic properties of self-assembled InAs quantum dots by atomic force microscopy with conductive tip*, Appl. Phys. Lett. **74**, 844 (1999).

[101] K. Zhang, A. Foede, Th. Schmidt, P. Sonntag, Ch. Heyn, G. Materlik, W. Hansen, and J. Falta *X-ray interface characterization of buried InAs Layers on GaAs(001)*, phys. stat. sol.(b), 791 (1999).

[102] M. Meduna, V. Holý, T. Roch, J. Stangl, G. Bauer, J. Zhu, K. Brunner, and G. Abstreiter, *X-ray reflectivity of self-assembled structures in SiGe multilayers and comparison with atomic force microscopy*, J. Appl. Phys. **89**, 4836 (2001).

[103] M. Jergel, *Interface study of a Co/Si/W/Si multilayer with enhanced thermal stability*, J. Appl. Cryst. **33**, 753 (2000).

[104] H. J. Güntherodt and R. Wisendanger, *Scanning Tunneling Microscopy I*, Springer, Berlin (1992).

[105] L. Seehofer, Doktorarbeit, Universität Hamburg (1993).

[106] A. Bolz, *X-ray diffraction on quantum dots*, Dissertation, Universität Hamburg, Shaker Verlag (2004).

[107] A. Malachias, *X-ray Scattering from Self-Assembled InAs Islands*, Brazilian Journal of Physics **34**, 571 (2004).

[108] Hoseman, *Bestimmung der statistischen Strukturparameter der Mizellgitter hochmolekularer Faserstoffe*, Z. Phys. **128**, 1 (1950).

[109] R. Hosemann and S. N. Bagchi, *Direct Analysis of Diffraction by Matter*, North-Holland, Amsterdam (1963).

[110] M. Hanke, *Streuung von Röntgenstrahlen an selbstorganisierten Halbleiter-Inselstrukturen*, Dissertation, Humboldt-Universität zu Berlin (2002).

[111] M. Hanke, M. Schmidbauer, D. Grigoriev, P. Schäfer, R. Köhler, T. H. Metzger, Zh. M. Wang, Yu. I. Mazur, and G. J. Salamo, *Zero-strain GaAs quantum dot molecules as investigated by x-ray diffuse scattering*, Appl. Phys. Lett. **89**, 053116 (2006).

[112] M. Schmidbauer, M. Hanke, and R. Köhler, *Effects of grazing incidence conditions on the x-ray diffuse scattering from self-assembled nanoscale islands*, Phys. Rev. B **71**, 115323 (2005).

[113] Takashi Hanada, Bon-Heun Koo, Hirofumi Totsuka, and Takafumi Yao, *Anisotropic shape of self-assembled InAs quantum dots: Refraction effect on spot shape of reflection high-energy electron diffraction*, Phys.Rev.B **64**, 165307 (2001).

[114] P. Werner, *Quantum Dot Structures in the InGaAs System Investigated by TEM Techniques*, Cryst. Res. Technol. **35**, 759 (2000).

[115] P. J. Grunthaner, R. P. Vasques, and F. J. Grunthaner, *Chemical depth profiles of the GaAs/native oxide interface*, J. Vac. Sci. Technol. **17**, 1045 (1980).

[116] A. Rosenauer, U. Fischer, D. Gerthsen, and A. Förster, *Composition evaluation of $In_xGa_{1-x}As$ Stranski-Krastanow-island structures by strain state analysis*, Appl. Phys. Lett. **71**, 3868 (1997).

[117] Helen R. Eisenberg and Daniel Kandel, *Wetting Layer Thickness and Early Evolution of Epitaxially Strained Thin Films*, Phys. Rev. Lett. **85**, 1286 (2000).

[118] R. Ohtsubo and K. Yamaguchi, *High quality InAs quantum dots covered by InGaAs/GaAs hetero-capping layer*, phys. stat. sol.(c) **3**, 939 (2003).

[119] Kinoshita Kyoichi, Japan Aerospace exploration agency, Space Experiments Summary, *Measurements of the Interdiffusion Coefficients of InAs-GaAs*

[120] P. Murugan, R. Pothiraj, S. D. D. Roy, and K. Ramachandran, *Si diffusion in GaAs*, Bull. Mater. Sci. **25**, 335 (2002).

[121] F. Y. Chang, C. C. Wu, and H. H. Lin, *Effect of InGaAs capping layer on the properties of InAs/InGaAs quantum dots and lasers*, Appl. Phys. Lett. **82**, 4477 (2003).

[122] Benjamin Sonnenberg-Klein, Kevin L. Silverman, and Richard P. Mirin, *Multimode Lasing at Room Temperature from InGaAs/GaAs Quantum Dot Lasers*, Proc. SPIE **4533**, Aug 21-22, Denver (2001).

[123] Fariba Ferdos, Shumin Wang, Yongqiang Wei, Anders Larsson, Mahdad Sadeghi, Qingxiang Zhao, *Influence of a thin GaAs cap layer on structural and optical properties of InAs quantum dots*, Appl. Phys. Let. **81**, 1195 (2002).

[124] U. H. Lee, *Visible photoluminescence from self-assembled InAs quantum dots embedded in AlAs cladding layers*, Appl. Phys. Let. **74**, 1597 (1999).

[125] P. Sutter and M. G. Lagally, *Embedding of Nanoscale 3D SiGe Islands in a Si Matrix*, Phys. Rev. B **81**, 3471 (1998).

[126] K. Pierz, A. Miglo, P. Hinze, F. J. Ahlers, G. Ade, I. Hapke-Wurst, U. Zeitler, and J. Hang, *Photoluminescence Study of InAs/AlAs Quantum Dots*, phys. stat. sol.(b) **224**, 119 (2001).

[127] D. Leonard, J. Vac. Sci. Technol. B **12(2)**, 1063 (1994).

[128] A. Hesse, *Effect of overgrowth on shape, composition, and strain of SiGe islands on Si(001)*, Phys. Rev. B **66**, 085321 (2002).

[129] G. Bauer, A. A. Darhuber, V. Holy, *Self-assembled Germanium-dot multilayers embedded in Silicon*, Cryst. Res. Technol. **34**, 197 (1999).

[130] A. Hesse at al., *Influence of capping and effect of overgrowth temperature on strain, composition and shape of SiGe islands*, workpackage I: Fabrication and analysis of quantum dot structures.

[131] J. G. Belk, *Surface Contrast in Two Dimensionally Nucleated Misfit Dislocations in InAsyGaAs(110) Heteroepitaxy*, Phys. Rev. Let. **78**, 475 (1997).

[132] C. Kendrick, G. LeLay, A. Kahn, *Bias-dependent imaging of the In-terminated InAs(001) (42)/c(82) surface by STM: Reconstruction and transitional defect*, Phys. Rev. B **54**, 17877 (1996).